

Thermodynamics and Kinetics of Carbon Dioxide Corrosion of Mild Steel
at Elevated Temperatures

A dissertation presented to
the faculty of
the Russ College of Engineering and Technology of Ohio University

In partial fulfillment
of the requirements for the degree
Doctor of Philosophy

Tanaporn Tanupabrungsun

May 2013

© 2013 Tanaporn Tanupabrungsun. All Rights Reserved.

This dissertation titled
Thermodynamics and Kinetics of Carbon Dioxide Corrosion of Mild Steel
at Elevated Temperatures

by

TANAPORN TANUPABRUNGSUN

has been approved for
the Department of Chemical and Biomolecular Engineering
and the Russ College of Engineering and Technology by

Srdjan Nešić

Professor of Chemical and Biomolecular Engineering

Dennis Irwin

Dean, Russ College of Engineering and Technology

Abstract

TANUPABRUNGSUN, TANAPORN, Ph.D. May 2013, Chemical Engineering

Thermodynamics and Kinetics of Carbon Dioxide Corrosion of Mild Steel at Elevated Temperatures

Director of Dissertation: Srdjan Nešić

CO₂ corrosion of mild steel in the oil and gas industry has been widely investigated. Nevertheless, research on high temperature CO₂ corrosion has been rarely conducted, and its mechanisms remain unclear. Therefore, it is important to complete an in-depth study of CO₂ corrosion of mild steel at high temperature. The entire scope of this Ph.D. research is to investigate and model CO₂ corrosion of mild steel over a range of 25-250°C. The research is divided into four main sections: chemical thermodynamics, electrochemical thermodynamics, electrochemical kinetics, and the proposal of mechanisms of CO₂ corrosion.

In the chemical thermodynamics segment, water chemistry components of CO₂ systems were studied. In the absence of Fe²⁺, pH increased with temperature in both predicted and experimental results. With addition of Fe²⁺, pH did not change with temperature due to FeCO₃ precipitation.

Pourbaix diagrams for the Fe-CO₂-H₂O systems were constructed using thermodynamic theory and data, subsequently validated with observed CO₂ corrosion phenomena. In the range of 80-150°C, FeCO₃ and Fe₂(OH)₂CO₃ formed on the steel surface, for experiments lasting 4 days. At 200-250°C, the corrosion product was exclusively Fe₃O₄. Kinetic studies conducted at 120°C show full transformation from

plate-like $\text{Fe}_2(\text{OH})_2\text{CO}_3$ to oblong prismatic FeCO_3 crystals over time. In relation to pressure effects, FeCO_3 is the more favored corrosion product than Fe_3O_4 at high $p\text{CO}_2$. With surface pH consideration, the generated Pourbaix diagrams were validated by experimental results.

The corrosion kinetic experiments at elevated temperatures were further investigated including the effects of pH and flow. It was concluded that corrosion rates did not monotonously decrease with temperatures due to formation of corrosion products. Corrosion rates at pH 4.0 were higher than those at pH 6.0, independent of temperature. The main corrosion product was FeCO_3 with Fe_3O_4 present at temperatures above 150°C . No flow sensitivity was observed due to the formation of corrosion products.

Mechanisms of CO_2 corrosion at temperatures of $25\text{-}250^\circ\text{C}$ were proposed based on the current CO_2 corrosion model with an addition of Fe_3O_4 formation. The thermodynamics and kinetics of Fe_3O_4 formation were identified. As soon as thermodynamic conditions for Fe_3O_4 are achieved, it forms and protects the steel.

Dedication

To

Phathanan Tanupabrungsun (my mother)

and

Sornsiri Saeheng (my aunt/foster mother)

for their unconditional love, caring and encouragement

Acknowledgments

First and foremost, I would like to express my greatest gratitude to my advisor and chairman of my dissertation committee, Dr. Srdjan Nešić, for all his constant guidance, help and support during my Ph.D. studies. With his direction, supervision and encouragement, he has helped me mature in both academic and social areas, and prepared me for the new challenges in my future career. I would not have had this success without him.

I would like to acknowledge Dr. David Young with his scientific guidance and his help on my academic progress. With his expertise in chemistry, I benefited from his direct contribution in the part of the dissertation related to corrosion product formation, analysis and identification.

I take this chance to thank my project leader, Bruce Brown, who worked closely with me and assisted me with my experimental work and valuable suggestions on my project. Assistance was also provided by Cody Shafer and other laboratory technicians at the Institute for Corrosion and Multiphase Technology (ICMT) with the experimental designs and equipment set-ups. Without their technical support, major parts of this dissertation would not be accomplished.

My gratitude is extended to other committee members, Dr. Michael Prudich, Dr. Valerie Young, Dr. Howard Dewald, Dr. Hugh Richardson and Dr. Yoon-Seok Choi for their agreements to serve on my dissertation committee.

I would like to express my deepest affection for Dr. Thunyaluk Pojtanabuntoeng, my colleague and true friend who shares the same nationality, kept me company during my 5-year Ph.D. studies, and always gives me her support. It was also a pleasure to work and spend time with all my colleagues at ICMT.

I would like to thank the CC-JIP sponsors for their financial support, technical direction and academic advisory role in my research.

The surface characterization was achieved with the help of several collaborators: Dr. John Lannuti, the Ohio State University, and Dr. Brian Hassler, the Center for Electrochemical Engineering Research (CEER), Ohio University, for the use of their XRD equipment/measurements and Dr. Hendrik Colijn from the Campus Electron Optics Facility of the Ohio State University for TEM/EDX analysis.

Last, but not least, I would like to express my deep indebtedness to my family for their unconditional love, caring and endless encouragement.

Contents

Abstract.....	3
Dedication.....	5
Acknowledgments.....	6
List of Tables	11
List of Figures.....	12
Chapter 1 : Introduction.....	21
1.1 Literature review.....	22
1.1.1 Mechanisms of CO ₂ corrosion	22
1.1.2 Key parameters in CO ₂ corrosion.....	24
1.1.3 Corrosion product formation in CO ₂ corrosion.....	25
1.2 Research objectives.....	27
Chapter 2 : Chemical Thermodynamics of CO ₂ Systems at Elevated Temperatures	30
2.1 Introduction.....	30
2.2 Water chemistry modeling.....	31
2.2.1 CO ₂ -H ₂ O systems	31
2.2.2 Fe ²⁺ -CO ₂ -H ₂ O systems.....	36
2.3 Experimental validation	39
2.3.1 Experimental setup.....	39
2.3.2 Experimental procedure	39
2.4 Results and discussion	40

2.5 Summary	46
Chapter 3 : Electrochemical Thermodynamics of Fe-CO ₂ -H ₂ O Systems at Elevated	
Temperatures.....	48
3.1 Introduction.....	48
3.2 Thermodynamic background	50
3.2.1 Electrochemical thermodynamics	50
3.2.2 Equilibria in the Fe-CO ₂ -H ₂ O System.....	54
3.2.3 Pourbaix diagrams	56
3.3 Experimental validation of generated Pourbaix diagrams	68
3.3.1 Experimental procedures	68
3.3.2 Results and discussion.....	70
3.4 Summary	100
Chapter 4 : Electrochemical Kinetics of Fe-CO ₂ -H ₂ O Systems at Elevated Temperatures	
.....	102
4.1 Introduction.....	102
4.2 Experimental procedure	102
4.3 Results and discussion	106
4.3.1 Preliminary results at 25-80°C in corrosion product free environments.....	106
4.3.2 Effect of specimen size.....	110
4.3.3 Effect of pH.....	112
4.3.4 Effect of flow.....	126

	10
4.3.5 Long-term experimental study	134
4.4 Summary	147
Chapter 5 : Mechanisms of CO ₂ Corrosion at Elevated Temperatures	148
5.1 Scenario of CO ₂ corrosion at temperatures up to 250°C	148
5.2 Mechanism of Fe ₃ O ₄ formation	151
5.2.1 Thermodynamics of Fe ₃ O ₄ formation	151
5.2.2 Kinetics of Fe ₃ O ₄ formation	152
5.2.3 Protectiveness of Fe ₃ O ₄ formation	155
5.3 Summary	160
Chapter 6 : Conclusions and Recommendations for Future Work	161
6.1 Conclusions	161
6.2 Recommendations for future work	162
References	163
Appendix A: Experimental Techniques	178
A.1 pH measurements	178
A.2 Corrosion rate calculation	181
Appendix B: EDX Analysis of Specimens	183

List of Tables

Table 1. Electrochemical reactions for CO ₂ corrosion.	23
Table 2. Equilibrium constants.	32
Table 3. Test matrix for the water chemistry validation experiments.	40
Table 4. Relationship between pH and dissolved CO ₂ with temperature.	45
Table 5. Thermodynamic data for the Fe-CO ₂ -H ₂ O system.	53
Table 6. Chemical reactions and equilibrium constants for a CO ₂ -H ₂ O system.	55
Table 7. Examples of the reactions representing FeCO ₃ precipitation.	55
Table 8. Key reactions considered in the Pourbaix diagrams for iron along with the expressions for their equilibrium (reversible) potential or pH.....	66
Table 9. Chemical composition of API 5L X65 (wt%).	69
Table 10. Test matrix for the experiments in Section 3.3.2.1 i).	71
Table 11. Test matrix for the experiments in Section 3.3.2.1 ii).	77
Table 12. XRD quantitative analysis for the experiments at 120°C (Data from Figure 20b., Figure 24b. - Figure 28b.).....	81
Table 13. Test matrix for the experiments in Section 3.3.2.1 iii).	84
Table 14. Water chemistry at 200°C for the conditions used in Section 3.3.2.1 iii).	85
Table 15. Effect of temperature on CO ₂ solubility and pressure (calculated based on Chapter 2).....	106
Table 16. Test conditions for Section 4.3.1.	107
Table 17. Test matrix for the experiments in Section 4.3.3.....	113
Table 18. Test matrix for the experiments in Section 4.3.4.....	127

List of Figures

Figure 1. The experimental and calculated Henry's constant vs. temperature.	33
Figure 2. The experimental and calculated K_{a1} vs. temperature.	34
Figure 3. The experimental and calculated K_{a2} vs. temperature.	35
Figure 4. The experimental and calculated K_w vs. temperature.	35
Figure 5. Steps of pH calculation with the effect of FeCO_3	38
Figure 6. Experimental setup for water chemistry validation.	39
Figure 7. Effect of temperature on pH for the $\text{CO}_2\text{-H}_2\text{O}$ system; 1 wt.% NaCl, $p\text{CO}_2 = 1$ bar at 25°C	41
Figure 8. Temperature effects on pressure for the $\text{CO}_2\text{-H}_2\text{O}$ systems; 1 wt.% NaCl, $p\text{CO}_2 = 1$ bar at 25°C	42
Figure 9. The calculated concentrations of species in the CO_2 -saturated solution vs. temperature; 1 wt.% NaCl, $p\text{CO}_2 = 1$ bar at 25°C	43
Figure 10. Comparison of the predictive model results and experimental results: pH vs temperature at the different concentrations of Fe^{2+} ; 1 wt.% NaCl, $p\text{CO}_2 = 1$ bar at 25°C	44
Figure 11. Example of a Pourbaix diagram for an $\text{Fe-H}_2\text{O}$ system at 25°C ;	57
Figure 12. Generated Pourbaix diagrams for $\text{Fe-CO}_2\text{-H}_2\text{O}$ systems corresponding to the experimental conditions given in Table 5; $c\text{Fe}^{2+}=10$ ppm, $c\text{Fe}^{3+}=10$ ppm, $p\text{H}_2=1$ bar, $p\text{O}_2=1$ bar, (symbols: • - typical bulk pH, o - corresponding surface pH in stagnant conditions).....	62
Figure 13. Potential-pH-temperature diagram for $\text{Fe-CO}_2\text{-H}_2\text{O}$ systems;	63

Figure 14. pH-temperature diagrams at $E = -0.5$ V, $p\text{CO}_2 = 1$ bar; a. $c\text{Fe}^{2+} = 1$ ppm, b. $c\text{Fe}^{2+} = 10$ ppm and c. $c\text{Fe}^{2+} = 100$ ppm.	64
Figure 15. pH-temperature diagrams at $E = -0.5$ V, $c\text{Fe}^{2+} = 1$ ppm; a. $p\text{CO}_2 = 1$ bar, b. $p\text{CO}_2 = 10$ bars and c. $p\text{CO}_2 = 100$ bars.	65
Figure 16. Weight-loss specimen.	69
Figure 17. Specimen surface of X65 polished with 600-grit sand paper.	69
Figure 18. Morphology and compositional analysis of corrosion product layer at 80°C , 4 days, 1 wt.% NaCl, $p\text{CO}_2 = 1$ bar at 25°C	72
Figure 19. Morphology and compositional analysis of corrosion product layer at 100°C , 4 days, 1 wt.% NaCl, $p\text{CO}_2 = 1$ bar at 25°C	73
Figure 20. Morphology and compositional analysis of corrosion product layer at 120°C , 4 days, 1 wt.% NaCl, $p\text{CO}_2 = 1$ bar at 25°C	73
Figure 21. Morphology and compositional analysis of corrosion product layer at 150°C , 4 days, 1 wt.% NaCl, $p\text{CO}_2 = 1$ bar at 25°C	74
Figure 22. Morphology and compositional analysis of corrosion product layer at 200°C , 4 days, 1 wt.% NaCl, $p\text{CO}_2 = 1$ bar at 25°C	74
Figure 23. Morphology and compositional analysis of corrosion product layer at 250°C , 4 days, 1 wt.% NaCl, $p\text{CO}_2 = 1$ bar at 25°C	75
Figure 24. Morphology and compositional analysis of corrosion product layer at 120°C , 1 day, 1 wt.% NaCl, $p\text{CO}_2 = 1$ bar at 25°C	78
Figure 25. Morphology and compositional analysis of corrosion product layer at 120°C , 2 days, 1 wt.% NaCl, $p\text{CO}_2 = 1$ bar at 25°C	79

Figure 26. Morphology and compositional analysis of corrosion product layer at 120°C, 7 days, 1 wt.% NaCl, pCO ₂ =1 bar at 25°C.	79
Figure 27. Morphology and compositional analysis of corrosion product layer at 120°C, 10 days, 1 wt.% NaCl, pCO ₂ =1 bar at 25°C.	80
Figure 28. Morphology and compositional analysis of corrosion product layer at 120°C, 30 days, 1 wt.% NaCl, pCO ₂ =1 bar at 25°C.	80
Figure 29. SEM images of corrosion product layers at 200°C, 1 wt.% NaCl, pCO ₂ =1 bar at 25°C (test conditions listed in Table 11).....	82
Figure 30. XRD analysis of corrosion product layers at 200°C, 1 wt.% NaCl, pCO ₂ =1 bar at 25°C (test conditions listed in Table 11).....	83
Figure 31. Surface analysis at 200°C, pCO ₂ =0.8bars, 4 days , 1 wt.% NaCl, pCO ₂ =1 bar at 25°C (test conditions listed in Table 13).....	85
Figure 32. Morphology and compositional analysis of corrosion product layer at 200°C, pCO ₂ =2.7 bars (equivalent to 1 bar @ 25°C), 1 wt.% NaCl, 4 days (test conditions listed in Table 13).	86
Figure 33. Morphology and compositional analysis of corrosion product layer at 200°C, pCO ₂ =3.8 bars, 1 wt.% NaCl, 4 days (test conditions listed in Table 13).....	86
Figure 34. Morphology and compositional analysis of corrosion product layer at 200°C, pCO ₂ =25 bars, 1 wt.% NaCl, 4 days (test conditions listed in Table 13).....	87
Figure 35. Generated Pourbaix diagrams at 200°C, cFe ²⁺ =10 ppm; corresponding to the experimental conditions as listed in Table 14.....	88

Figure 36. Weight loss corrosion rates vs temperature; $p\text{CO}_2 = 1$ bar at 25°C , 1 wt.% NaCl, 4-day exposure (test conditions listed in Table 10).....	90
Figure 37. Metal loss and Fe^{2+} concentration in mol/l vs temperature; 1 $p\text{CO}_2 = 1$ bar at 25°C , 1 wt.% NaCl, 4-day exposure.....	90
Figure 38. Average weight loss corrosion rate over time at 120°C ; $p\text{CO}_2 = 1$ bar at 25°C , 1 wt.% NaCl.....	91
Figure 39. Average weight loss corrosion rate over time at 200°C ; $p\text{CO}_2 = 1$ bar at 25°C , 1 wt.% NaCl.....	92
Figure 40. Moles of iron from X65 samples in autoclave testing at 120°C ; $p\text{CO}_2 = 1$ bar at 25°C , 1 wt.% NaCl.	92
Figure 41. Moles of iron from X65 samples in autoclave testing at 200°C ; $p\text{CO}_2 = 1$ bar at 25°C , 1 wt.% NaCl.	93
Figure 42. TEM analysis: Cross section of steel surface at 200°C ; $p\text{CO}_2 = 1$ bar at 25°C , 1 wt.% NaCl, 4-day exposure; corresponding to Figure 22.....	93
Figure 43. SEM images of steel surfaces after cleaning from Figure 20 and Figure 22, respectively, for the 4-day experiments.....	94
Figure 44. 3D profilometry analysis of steel surfaces after cleaning from Figure 43 a. and b., respectively.....	96
Figure 45. 3D Profilometry at 120°C , 30 days after cleaning the surface from Figure 28.	97
Figure 46. 3D Profilometry at 200°C , 30 days after cleaning the surface from Figure 29 d.	99

Figure 47. Weight loss corrosion rate vs $p\text{CO}_2$ at 200°C , 1 wt.% NaCl, 4 days (test conditions listed in Table 13).....	100
Figure 48. 4-Liter autoclave system from Cortest, Incorporated.....	104
Figure 49. Drawings of autoclave configurations with electrochemical measurements equipped.....	105
Figure 50. Drawings of specimen configuration.....	105
Figure 51. Potentiodynamic sweep: Glass cell tests, total pressure = 1 bar (test condition listed in Table 16, Set 1).	108
Figure 52. Potentiodynamic sweep: Autoclave tests, $c\text{CO}_2 = 0.030\text{ M}$ (test condition listed in Table 16, Set 2).	109
Figure 53. LPR corrosion rate vs temperature: 1 wt.% NaCl, pH 4.0, total pressure=1 bar for glass cell tests and $c\text{CO}_2 = 0.030\text{ M}$ for autoclave experiments (test condition listed in Table 16).	109
Figure 54. Specimens used in Section 4.3.2: a. $A/V=0.7\text{cm}^2/\text{l}$, b. $A/V=2.1\text{cm}^2/\text{l}$ and c. $A/V=6.3\text{cm}^2/\text{l}$	110
Figure 55. Effect of specimen size on corrosion rate over temperature; 120°C , 1 wt.% NaCl, $c\text{CO}_2 = 0.030\text{ M}$, pH 4.0 (water chemistry in Table 4, Set C).....	111
Figure 56. SEM images of the steel surface for different specimen sizes at 120°C , after 20 hours, corresponding to the corrosion rate results in Figure 55.....	112
Figure 57. LPR corrosion rate over time; $T=80\text{-}200^\circ\text{C}$, 1 wt.% NaCl, $c\text{CO}_2 = 0.030\text{ M}$, 20 hours.....	114
Figure 58. EIS at 80°C , 1 wt.% NaCl, $c\text{CO}_2 = 0.030\text{ M}$, 20 hours.	115

Figure 59. SEM images at 80°C, 1 wt.% NaCl, cCO ₂ = 0.030 M, 20 hours.....	115
Figure 60. EIS at 120°C, 1 wt.% NaCl, cCO ₂ = 0.030 M, 20 hours.	116
Figure 61. SEM images at 120°C, 1 wt.% NaCl, cCO ₂ = 0.030 M, 20 hours.....	117
Figure 62. EIS at 150°C, 1 wt.% NaCl, cCO ₂ = 0.030 M , 20 hours.	117
Figure 63. SEM images at 150°C, 1 wt.% NaCl, cCO ₂ = 0.030 M, 20 hours.....	118
Figure 64. EIS at 200°C, 1 wt.% NaCl, cCO ₂ = 0.030 M, 20 hours.	119
Figure 65. SEM images at 200°C, 1 wt.% NaCl, cCO ₂ = 0.030 M, 20 hours.....	120
Figure 66. XRD analysis at pH 4.0, 1 wt.% NaCl, cCO ₂ = 0.030 M, 20 hours.	121
Figure 67. Cross-sectional analysis at 150°C, pH 4.0, 1 wt.% NaCl, cCO ₂ = 0.030 M, 20 hours, corresponding to Figure 63.	122
Figure 68. Generated Pourbaix diagrams for Fe-CO ₂ -H ₂ O systems; cCO ₂ = 0.030 M, cFe ²⁺ = 50 ppm. (● = bulk pH, o = surface pH).....	124
Figure 69. LPR corrosion rate at 20 hours vs temperature: 1 wt.% NaCl, cCO ₂ = 0.030 M, pH 4.0.....	125
Figure 70. LPR corrosion rate at 20 hours vs temperature: 1 wt.% NaCl, cCO ₂ = 0.030 M, pH 6.0.....	125
Figure 71. LPR corrosion rates at 120°C, pH 4.0, 1 wt% NaCl, cCO ₂ = 0.030 M; Rotating speeds of 0, 100, 500 and 1000 rpm (equivalent to 0, 0.1, 0.5, 1.0 m/s, respectively)...	128
Figure 72. LPR corrosion rates at 20 hours: 120°C, pH 4.0, 1 wt% NaCl, cCO ₂ = 0.030M: 0, 100, 500 and 1,000rpm (equivalent to 0, 0.1, 0.5 and 1.0 m/s, respectively).	129
Figure 73. EIS spectrum at 120°C, pH 4.0, 1 wt% NaCl, cCO ₂ = 0.030 M, 20 hours....	129

Figure 74. SEM images of flow effects at 120°C, pH 4.0, 1 wt.% NaCl, cCO ₂ = 0.030 M, 20 hours.....	130
Figure 75. Generated Pourbaix diagram at 120°C, cCO ₂ = 0.030 M, cFe ²⁺ = 50 ppm. (● = bulk pH, o = surface pH).	131
Figure 76. LRP corrosion rates with varying flow rates; at 120°C, pH 4.0, 1 wt.% NaCl, cCO ₂ = 0.030 M.	132
Figure 77. SEM image from the test at 120°C, pH 4.0, 1 wt.% NaCl, cCO ₂ = 0.030 M, after 46 hours.	132
Figure 78. LRP corrosion rates at 200°C, pH 4.0, 1 wt.% NaCl, cCO ₂ = 0.030M; Rotating speeds of 0, 100 and 1,000rpm (equivalent to 0, 0.1 and 1.0m/s, respectively).	133
Figure 79. LRP corrosion rates at 20 hours: 200°C, pH 4.0, 1 wt.% NaCl, cCO ₂ = 0.030M: 0, 100 and 1,000rpm (equivalent to 0, 0.1 and 1.0 m/s, respectively).	133
Figure 80. SEM images at 200°C, pH 4.0, 1 wt.% NaCl, cCO ₂ = 0.030M, 20 hours.....	134
Figure 81. LRP corrosion rates at 120 and 200°C, pH 4.0, 1 wt.% NaCl, cCO ₂ = 0.030 M.	136
Figure 82. Open circuit potentials over time at 120 and 200°C, pH 4.0, 1 wt.% NaCl, cCO ₂ = 0.030 M.	136
Figure 83. Surface analysis at 120°C, pH 4.0, 1 wt.% NaCl, cCO ₂ = 0.030 M, 14 days.	137
Figure 84. Back-scatter cross-sections for 120°C, pH 4.0, 1 wt.% NaCl, cCO ₂ = 0.030 M, 14 days.	138
Figure 85. Surface after corrosion product removal at 120°C, pH 4.0, 1 wt.% NaCl, cCO ₂ = 0.030 M, 14 days.	138

Figure 86. 3D Profilometry at 120°C, pH 4.0, 1 wt.% NaCl, cCO ₂ = 0.030 M, 14 days, corresponding to Figure 85.	140
Figure 87. EIS results: pH 4.0, 1 wt.% NaCl, cCO ₂ = 0.030 M.....	140
Figure 88. Surface analysis at 200°C, pH 4.0, 1 wt.% NaCl, cCO ₂ = 0.030 M, 14days.	141
Figure 89. Surface after corrosion product removal at 200°C, pH 4.0, 1 wt.% NaCl, cCO ₂ = 0.030 M, 14 days.....	141
Figure 90. 3D Profilometry at 200°C, pH 4.0, 1 wt.% NaCl, cCO ₂ = 0.030 M, 14 days; corresponding to Figure 89.	143
Figure 91. LPR corrosion rate at 120°C, pH 4.0, 1 wt.% NaCl, cCO ₂ = 0.030 M, 14 days.	145
Figure 92. Nyquist plots at 120°C, 1000 rpm, pH 4.0, 1 wt.% NaCl, cCO ₂ = 0.030 M.	146
Figure 93. Surface analysis at 120°C, 1000 rpm, pH 4.0, 1 wt.% NaCl, cCO ₂ = 0.030 M, 14 days.	147
Figure 94. Scenarios for CO ₂ corrosion.....	151
Figure 95. Solubility limit of Fe ₃ O ₄ formation as a function of temperature.	152
Figure 96. Comparison of corrosion rate with different types of corrosion product covered on the steel surface; pH 4.0, 1 wt.% NaCl; FeCO ₃ : 120°C, cCO ₂ = 0.030 M; FeCO ₃ and Fe ₃ O ₄ : 200°C, cCO ₂ = 0.021 M; Fe ₃ O ₄ : 200°C, cCO ₂ = 0.030 M.....	153
Figure 97. Morphology of Fe ₃ O ₄ on the steel surface: results from Section 3.3.2.1 i)...	154
Figure 98. Morphology of FeCO ₃ on the steel surface; results from Section 3.3.2.1 ii).	155

Figure 99. Comparison of corrosion rates between predicted and experimental results; pH 4.0, 1 wt.% NaCl; FeCO ₃ : 120°C, cCO ₂ = 0.030 M; FeCO ₃ and Fe ₃ O ₄ : 200°C, cCO ₂ = 0.021 M; Fe ₃ O ₄ : 200°C, cCO ₂ = 0.030 M.....	156
Figure 100. Corrosion rates and open circuit potentials at 120 and 200°C.	157
Figure 101. Decrease in open circuit potentials due to diffusion barrier.....	158
Figure 102. Increase in open circuit potentials.	159
Figure 103. Morphology of the steel surface covered by corrosion products from Figure 67: 1 = Fe, 2 = Fe ₃ O ₄ , 3 = FeCO ₃ , 4 = Epoxy.	159
Figure 104. Types of pH electrodes and a high temperature reference electrode (Source: <i>Corr Instruments, LLC</i>).	179
Figure 105. Measured potential vs. pH calibration curve for the ZrO ₂ -based pH electrode.	181
Figure 106. EDX analysis of sample at 80°C, 4 days corresponding to Figure 18.	183
Figure 107. EDX analysis of sample at 100°C, 4 days corresponding to Figure 19.	183
Figure 108. EDX analysis of sample at 120°C, 4 days corresponding to Figure 20.	184
Figure 109. EDX analysis of sample at 150°C, 4 days corresponding to Figure 21.	184
Figure 110. EDX analysis of sample at 200°C, 4 days corresponding to Figure 22.	185
Figure 111. EDX analysis of sample at 120°C, 7 days corresponding to Figure 26.	185
Figure 112. EDX analysis of sample at 120°C, 30 days corresponding to Figure 28. ...	186
Figure 113. EDX analysis of sample at 200°C corresponding to Figure 29.....	186

Chapter 1: Introduction

Carbon dioxide (CO₂) corrosion in wellbores, pipelines and production/separation facilities can have significant economic and environmental consequences for the oil and gas industry and in carbon capture/sequestration. Due to declining production of hydrocarbons from relatively shallow geologic formations, oil and gas are increasingly produced from deeper reservoirs [1–3]. The deeper the well is, the higher the temperature downhole. This leads to more severe conditions and higher risks relating to corrosion management. CO₂ corrosion has been widely investigated and is now well understood for relatively low temperatures and pressures (<100°C, < 5 bars) [4–32], mechanistic models have been developed describing its mechanisms under such conditions and have evolved into widely used corrosion prediction software.

MULTICORP is one of the most advanced corrosion prediction models. Its backbone is derived from studies performed at the Institute for Corrosion and Multiphase Technology (ICMT) at Ohio University. Water chemistry, electrochemistry, mass transport and FeCO₃ layer formation are simulated according to underlying physicochemical laws [16], [26], [27]. Nevertheless, research on CO₂ corrosion at elevated temperatures (above 100°C) has rarely been conducted [24], [30–32]. Consequently, the corrosion mechanisms at higher temperature remain unclear and, hence, mechanistic models have yet to be developed. Therefore, the main goals of this research are to define the CO₂ corrosion mechanisms and to predict the corrosion severity at temperatures up to 250°C, which will result in the expansion of the valid temperature range in the current CO₂ corrosion model MULTICORP.

This document is structured as follows: 0 provides the literature review and the research objectives; Chapter 2 presents chemical thermodynamics and water chemistry for the CO₂ system; Chapter 3 demonstrates the electrochemical thermodynamics for construction and validation of Pourbaix diagrams; Chapter 4 presents the electrochemical kinetics corrosion experiments; Chapter 5 proposes the mechanisms of CO₂ corrosion at temperatures of 25-250°C; Chapter 6 provides conclusions and recommendations for future work. Relevant experimental details are described in Appendix A and B.

It should be noted that parts of the research described below have been published in the internal confidential reports to the Ohio University Corrosion Center Joint Industry Project (CC-JIP) Advisory Board meetings over the period 2008 – 2012 [33–39]. In addition, excerpts from the work were or will be published at NACE (National Association of Corrosion Engineers) International conferences [40], [41].

1.1 Literature review

In this chapter, three main areas of CO₂ corrosion are discussed: mechanisms of CO₂ corrosion, key parameters affecting CO₂ corrosion (such as pH, temperature and flow) and corrosion product formation.

1.1.1 Mechanisms of CO₂ corrosion

The mechanisms of CO₂ corrosion in aqueous environments at temperatures up to 100°C have been proposed by many researchers [7], [8], [13], [14], [42]. When steel is in a corrosive environment, such as in acidic environments or CO₂ systems (indirectly

acidic through H_2CO_3 formation), corrosion processes will occur. Corrosion is an electrochemical process, consisting of two classes of half-reactions, anodic and cathodic, as listed in Table 1. For CO_2 corrosion of mild steel, the main anodic reaction is iron oxidation and the main cathodic reactions are the reduction of H^+ , H_2CO_3 and H_2O .

Table 1. Electrochemical reactions for CO_2 corrosion.

	Name	Reaction
Cathodic reactions	H^+ reduction	$2\text{H}^+_{(\text{aq})} + 2\text{e}^- \rightarrow \text{H}_{2(\text{g})}$
	H_2CO_3 reduction	$2\text{H}_2\text{CO}_{3(\text{aq})} + 2\text{e}^- \rightarrow 2\text{HCO}_{3(\text{aq})}^- + \text{H}_{2(\text{g})}$
	H_2O reduction	$2\text{H}_2\text{O}_{(\text{l})} + 2\text{e}^- \rightarrow 2\text{OH}^-_{(\text{aq})} + \text{H}_{2(\text{g})}$
Anodic reaction	Fe oxidation	$\text{Fe}_{(\text{s})} \rightarrow \text{Fe}^{2+}_{(\text{aq})} + 2\text{e}^-$

However, in addition to the electrochemical reactions, the corrosion mechanisms always involve other processes such as chemical reactions (more discussion in Chapter 2) and mass transfer phenomena [16]. For instance, if only the electrochemical reactions are taken into account, the proposed models above will sometimes over-predicted corrosion rates due to the unaccounted for formation of corrosion products in actual situations [43]. In CO_2 corrosion, when steel is corroded it releases soluble Fe^{2+} . Once conditions for forming FeCO_3 are achieved and are above the saturation level (S) for FeCO_3 , FeCO_3 will cover the steel surface or act as a diffusion barrier [13], [44–49]. The FeCO_3 formation may reduce corrosion rate depending on several parameters [50–52]. The protectiveness of FeCO_3 is determined from the scaling tendency, defined as the ratio of

the FeCO_3 formation/precipitation rate to corrosion rate [15], [43]. If the rate of formation/precipitation is faster than the rate of corrosion, the scaling tendency will be high. Thus, the FeCO_3 forms as a dense and protective scale on the steel surface. On the other hand, if the corrosion rate is faster than the precipitation rate the scaling tendency is low, a porous and non-protective corrosion product layer will form.

1.1.2 Key parameters in CO_2 corrosion

pH has a significant direct effect on the corrosion rate and indirect influence via FeCO_3 formation; the lower the pH the more corrosive the system [15]. At high pH, the solubility of FeCO_3 decreases leading to a high precipitation rate and scaling tendency. If the protective FeCO_3 layer covers the steel surface, the corrosion rate will decrease [27], [44], [47].

de Waard and Milliams [42] studied the effect of temperature (up to 80°C) at pH 4.0 in CO_2 corrosion. They concluded that the corrosion rate increased with temperature due to the kinetic rate of the electrochemical reactions being accelerated by temperature. Gray *et al.* [7], [8] also suggested that corrosion rate increased as temperature increased. However, at temperatures of $90\text{-}125^\circ\text{C}$, the corrosion rate did not change with temperature because there was protective FeCO_3 formation on the steel surface. It was suggested that FeCO_3 slowed down both anodic and cathodic reactions [53].

Similarly, Ikeda *et al.* [24] and de Waard and Lotz [54] found that the corrosion rate increased with temperature until it reached maximum values around a temperature range of $60\text{-}120^\circ\text{C}$, depending on partial pressure of CO_2 , then it decreased with

temperature due to corrosion product formation. For instance, at 0.1 and 1 bar of partial pressure of CO₂, the corrosion rates had the maximum values at 120°C and 80°C, respectively. In addition, the peak of the corrosion rate was found at temperatures between 60°C and 80°C, depending on water chemistry and flow [55–57].

Many researchers [57–60] investigated the effect of flow on CO₂ corrosion. It was found that the corrosion rate increased as a function of flow in the absence of corrosion product layers. However, Nešić, *et al.*, [60] suggested that when temperature (50–80°C) increased the corrosion rate has no flow sensitivity due to the corrosion product formation on the steel surface and its action as a mass transfer barrier.

1.1.3 Corrosion product formation in CO₂ corrosion

From the literature discussed above, it seems that the corrosion product formation has significant impacts on CO₂ corrosion mechanisms at elevated temperatures. In this section, the types of corrosion products found in CO₂ corrosion and their effects on corrosion phenomena are discussed.

Starting with low temperatures (lower than 60°C), typically no corrosion product layer is formed [7], [15], [24], [61]. However, De Marco, *et al.*, [62], [63] proposed that a range of carbonate compounds, including Fe₂(OH)₂CO₃, Fe₆(OH)₁₂CO₃, Fe₂O₂CO₃ and Fe₆(OH)₁₂CO₃•H₂O, that can form as corrosion products at temperatures ranging from 20°C to 40°C at high pH.

Ikeda, *et al.*, [24] concluded that temperature and pressure of CO₂ affect the corrosion rate and the corrosion product layers on low carbon steel in CO₂ environments. At

temperatures lower than 60°C, no corrosion product layer was formed. Only uniform corrosion occurred. At temperatures between 60°C and 150°C, pitting corrosion occurred, and the scale consisted of thick, prismatic crystals. The corrosion rate was the highest in this temperature range. At temperatures above 150°C, corrosion rates were relatively low due to the formation of protective FeCO₃ layers.

Shannon [31] studied the role of chemical components in geothermal brines on corrosion. The thermodynamic stability of iron was investigated both computationally and experimentally. In the experiments, it was found that at low pH (4.8) the main corrosion products were aqueous Fe²⁺ at 50°C, FeCO₃ at 150°C, and 70% of Fe₃O₄ with 30% of FeCO₃ at 250°C. Nevertheless, at higher pH (7.5), there was no observable solid corrosion product detected at 50°C, but Fe₃O₄ was observed at 150°C and 250°C.

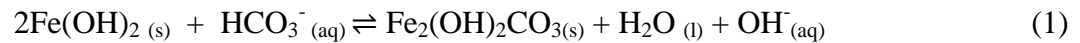
Yin *et al.* [30] examined the effect of temperature on CO₂ corrosion of carbon steel over a range of 50-180°C. They concluded that temperature changed the crystal morphology of corrosion scales. The finer and denser the scale was, the lower the corrosion rate. It has been shown that the corrosion rate at 50°C was the highest in this range, and the corrosion rate at 100°C was the lowest due to the formation of the finest crystal and densest corrosion product layer. At temperatures above 100°C, the corrosion rate increased slightly with temperature. In addition, not only was the main corrosion product FeCO₃, but some trace amounts of Fe₃C and Fe₃O₄ were observed.

Lin, *et al.*, [32] observed the corrosion product layer of carbon steel at 80-200°C in an aqueous CO₂ solution. They found two distinct layers on the bare metal surface, which were composed of a very thin film layer beneath a layer of prismatic crystals.

Furthermore, at 120°C, the grain sizes of crystal scales were the largest, and the layer of the corrosion products was the thickest. The authors provided similar results for their corrosion rate and the characteristics of corrosion scales to results from Ikeda, *et al.* [24].

Han *et al.* [64] investigated the pseudo-passive layer on the mild steel surfaces in CO₂ corrosion using grazing incidence X-ray diffraction and transmission electron microscopy with energy dispersive X-ray fluorescence analysis. The results show that iron carbonate (FeCO₃) formed on the steel surface at high pH, with thorough coverage. However, magnetite (Fe₃O₄) was observed along the grain boundaries of the FeCO₃ crystals and adjacent to the steel surface at these locations.

Rémazeilles and Rafait [65] suggested that Fe(OH)₂ transforms into Fe₂(OH)₂CO₃ over a long period of aging according to Equation (1).



Schlegel, *et al.*, [66] proposed the formation of FeCO₃ and Fe₂(OH)₂CO₃ as expressed in Equation (2). This reaction is controlled by partial pressure of CO₂ and pH. If pH is high, Fe₂(OH)₂CO₃ will be favored. In contrast, if the partial pressure of CO₂ is high, FeCO₃ will dominate.



1.2 Research objectives

As discussed in the literature review (Section 1.1), many questions and uncertainties surround the mechanisms of CO₂ corrosion at high temperature. New test equipment, revised test procedures and expanded monitoring technologies need to be

employed for higher temperature corrosion tests. The entire scope of this Ph.D. research is to understand the mechanisms of CO₂ corrosion of mild steel over a range of 25-250°C by studying a closed system in which temperature and concentrations of species related to the corrosion reaction can be well defined. As stated above, the research is divided into four main sections: chemical thermodynamics (Chapter 2), electrochemical thermodynamics (Chapter 3), electrochemical kinetics (Chapter 4) and the proposal of mechanisms of CO₂ corrosion (Chapter 5).

The first section defines the water chemistry components in a closed CO₂ system at temperatures of 25-250°C by using a thermodynamic approach relying on theoretical values from various open literature sources and a comparison of theoretical to experimental values.

With the introduction of steel to the aqueous environment, the electrochemical thermodynamics of Fe-CO₂-H₂O systems was studied to implement thermodynamic calculations and predict corrosion products by constructing the potential-pH (Pourbaix) diagrams in the temperature range of 25-250°C and validating them with experimental results of surface characterization and their influence on corrosion behaviors. Scanning electron microscopy (SEM), energy dispersive X-ray spectroscopy (EDX), X-ray diffraction (XRD), transmission electron microscopy (TEM) and 3D profilometry techniques were used for surface analysis.

For the corrosion kinetics study, the effect of temperature on CO₂ corrosion has been investigated, which includes the analysis of the corrosion product layer on mild steel. CO₂ corrosion mechanisms as influenced by the effects of pH and flow were also

investigated using electrochemical measurements: linear polarization resistance (LPR) and electrochemical impedance spectroscopy (EIS).

Finally, the mechanisms of CO₂ corrosion at temperatures of 25-250°C were proposed for prediction purposes by integrating all of the above.

Chapter 2: Chemical Thermodynamics of CO₂ Systems at Elevated Temperatures

2.1 Introduction

Since CO₂ corrosion occurs only in the presence of water, water chemistry is the most influential characteristic of corrosion in aqueous environments. Generally, if water is acidic it will be corrosive, which implies onset of high corrosion rates [4], [5], [7], [15], [28]. On the other hand if water has high pH then corrosion product layer formation will be favored, which may provide some protection to the steel surface against lower corrosion rates [13], [22], [45], [48], [50].

Several researchers in various research fields, such as geology, marine chemistry, sedimentology and corrosion [67–77] investigated the effect of temperature on the equilibrium constants for CO₂-H₂O systems by conducting experiments or using theoretical thermodynamic models. However, there are differences among these equilibrium constants. Therefore, the main objective of this chapter was to validate a water chemistry model over a temperature range of 25-250°C in CO₂-saturated solution using the equilibrium constants in the current corrosion model, MULTICORP. The work presented in this chapter was structured into two main parts:

- Build a thermodynamic model based on the information available in the open literature.
- Validate the developed water chemistry model with experimental data.

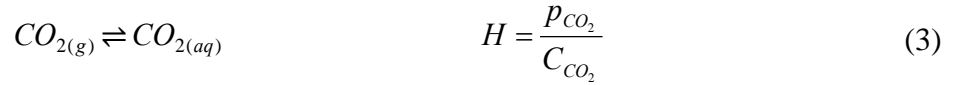
2.2 Water chemistry modeling

2.2.1 CO_2 - H_2O systems

In a CO_2 - H_2O system, five homogeneous chemical reactions are considered in the model as shown in Equation (3)-(7); their equilibrium constants are presented in Table 2.

These correspond to:

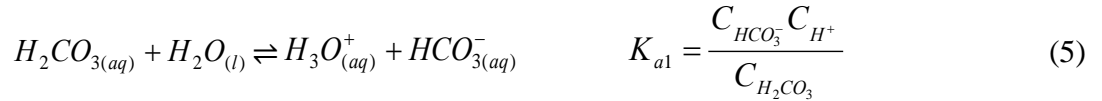
- Dissolution of carbon dioxide:



- Carbon dioxide hydration:



- Carbonic acid dissociation:



- Bicarbonate anion dissociation:



- Water dissociation:



where H is Henry's constant for the dissolution of carbon dioxide, K_h is the equilibrium constant for the carbon dioxide hydration, K_{a1} is the equilibrium constant for the carbonic acid dissociation, K_{a2} is the equilibrium constant for the bicarbonate anion dissociation,

K_w is the equilibrium constant for the water dissociation, $p\text{CO}_2$ is the partial pressure of carbon dioxide, and C_x is the concentration of species x .

Table 2. Equilibrium constants.

Equilibrium Constant	Unit	Temperature (°C)	Ref.
$H = \frac{14.5}{1.0038} \times 10^{-(2.27 + (5.65 \times 10^{-3} T_f) - 8.06 \times 10^{-6} T_f^2 + 0.075 I)}$	molar/ bar	0-200	[72]
$K_h = 2.58 \times 10^{-3}$	molar	0-300	[67]
$K_{a1} = 387.6 \times 10^{-(6.41 - 1.594 \times 10^{-3} T_f + 8.52 \times 10^{-6} T_f^2 - 3.07 \times 10^{-5} p - 0.4772 I^{0.5} + 0.1180 I)}$	molar	0-200	[72]
$K_{a2} = 10^{-(10.61 - 4.97 \times 10^{-3} T_f + 1.331 \times 10^{-5} T_f^2 - 2.624 \times 10^{-5} p - 1.166 I^{0.5} + 0.3466 I)}$	molar	0-200	[72]
$K_w = 10^{-(293868 - 0.0737549 T_K + 7.47881 \times 10^{-5} T_K^2)}$	molar ²	0-350	[78]

Note: In the table, T_f and T_K are Temperature in degrees Fahrenheit and Kelvin, respectively, p is the pressure in psi, I is ionic strength in molar.

All the equilibrium constants listed in Table 2 were used previously in this research and the current corrosion model, MULTICORP. To expand the temperature range in the model and validate these equilibrium constants, they were compared to other published data. To begin with, Henry's constant (H) by Oddo and Tomson [72] was compared to that published by Li and Duan [79] as shown in Figure 1. Li and Duan [79] developed a model for the calculation of speciation equilibrium coupled with liquid-

vapor phase equilibrium in the $\text{CO}_2\text{-H}_2\text{O-NaCl}$ system from 0-250°C. The equilibrium constants were calculated thermodynamically from the standard free energy change, the enthalpy of chemical reactions and the heat capacity of species. Furthermore, the equilibrium constant was compared with that published by Zawlsza, *et al.* [73]. They carried out experiments using potentiometric measurements from 0-200°C. In Figure 1, the results show that the Henry's constant values published by these authors deviate by less than a 15% from each other.

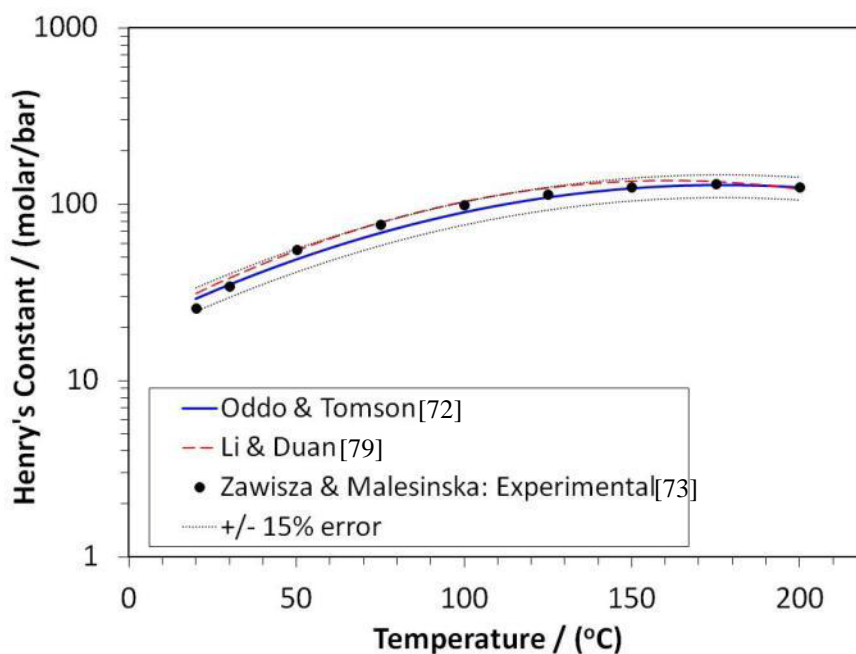


Figure 1. The experimental and calculated Henry's constant vs. temperature.

For K_{a1} and K_{a2} , the equilibrium constants were compared with those published by Li and Duan [79] and Millero, *et al.* [71] as shown in Figure 2 and Figure 3. In the Millero, *et al.*, publication, K_{a1} and K_{a2} were measured using potentiometric

measurements from 0 to 50°C. For 50-250°C, the K values were taken from Patterson, *et al.*, [80] which used a potentiometric technique. The results show that all the values lie within a 15% error except at temperatures greater than 150°C, these data lie outside this arbitrary margin of error. The validity of these equilibrium constants is explored in Section 2.4.

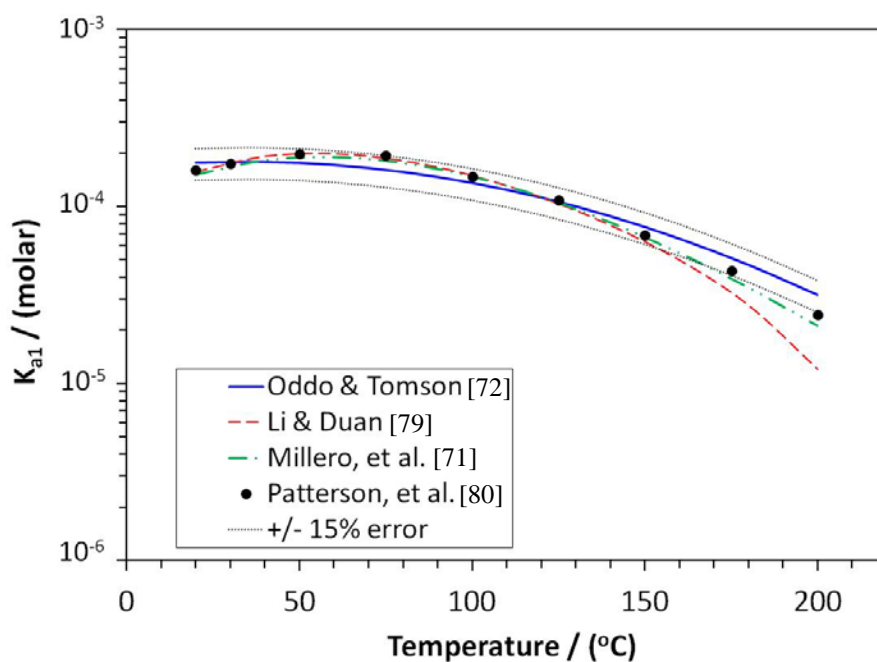


Figure 2. The experimental and calculated K_{a1} vs. temperature.

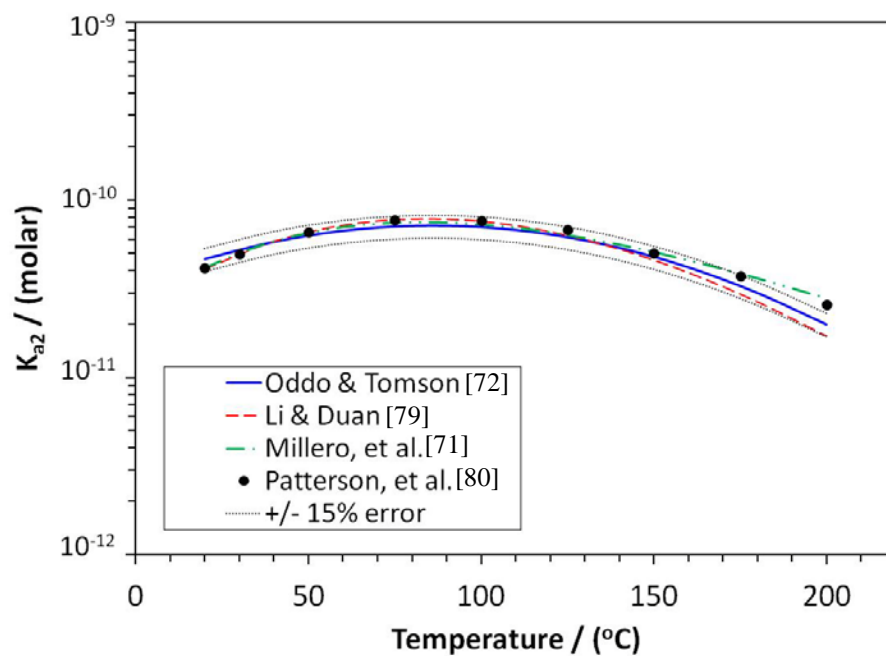


Figure 3. The experimental and calculated K_{a2} vs. temperature.

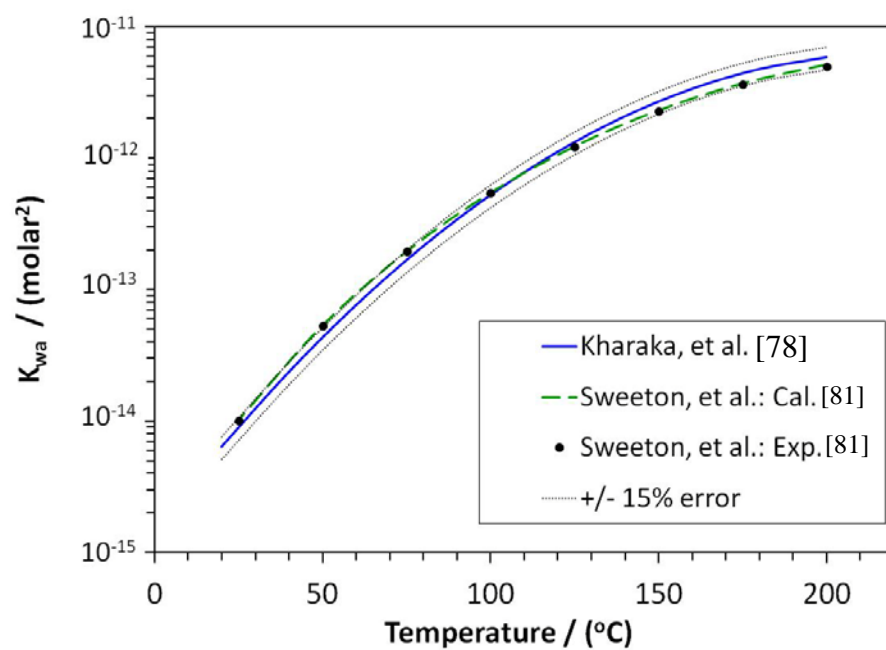


Figure 4. The experimental and calculated K_w vs. temperature.

In order to calculate the concentration of species at equilibrium, electro-neutrality must be satisfied since the solution cannot have a net charge:

$$C_{H^+} = C_{HCO_3^-} + 2C_{CO_3^{2-}} + C_{OH^-} \quad (8)$$

There are two types of systems which need to be distinguished: open and closed.

– For an open system, examples are: a field condition with a large amount of gaseous CO₂ or in a laboratory: a glass cell purged continuously with CO₂. In these systems, the partial pressure of CO₂ is assumed to be constant. The equations (3) – (6) are used for the calculation of net equilibria.

– For a closed system, examples are: a field condition with a small amount of gaseous CO₂ or in a laboratory: a closed autoclave. In closed systems, the partial pressure of CO₂ cannot be assumed to be constant, so there is one more unknown. However, the total amount of carbonic and carbonate species is constant, as expressed by Equation (9), and there is one more equation. To calculate the equilibrium, the equations listed here (Equation (3) - (9)) take this into account.

$$M_{CO_{2(g)}} + M_{CO_{2(aq)}} + M_{H_2CO_3} + M_{HCO_3^-} + M_{CO_3^{2-}} = const. \quad (9)$$

where M_x is the number of moles of species x .

2.2.2 Fe^{2+} -CO₂-H₂O systems

According to the literature review (Section 1.1.3), the main solid species expected to be presented in a Fe²⁺-CO₂-H₂O system at temperatures of 25-250°C are FeCO₃ and Fe₃O₄. Nevertheless, due to limitation of kinetics information for magnetite (Fe₃O₄)

formation, only iron carbonate (FeCO_3) precipitation was considered. Thus, six chemical reactions, Equation (3) - (7) and (10), were considered in the model.



In addition of Equation (8) and (9), the Fe, Fe^{2+} and FeCO_3 species were considered as shown in Equation (11) - (13):

$$C_{\text{H}^+} + 2C_{\text{Fe}^{2+}} + C_{\text{Na}^+} = C_{\text{HCO}_3^-} + 2C_{\text{CO}_3^{2-}} + C_{\text{OH}^-} + C_{\text{Cl}^-} \quad (11)$$

$$M_{\text{CO}_2(g)} + M_{\text{CO}_2(aq)} + M_{\text{H}_2\text{CO}_3} + M_{\text{HCO}_3^-} + M_{\text{CO}_3^{2-}} + M_{\text{FeCO}_3} = \text{const.} \quad (12)$$

$$M_{\text{Fe}^{2+}} + M_{\text{FeCO}_3} = \text{const.} \quad (13)$$

The FeCO_3 precipitation occurs when the concentrations of Fe^{2+} and CO_3^{2-} exceed the solubility limit (K_{sp}), and saturation (S) is defined as:

$$S = \frac{C_{\text{Fe}^{2+}} C_{\text{CO}_3^{2-}}}{K_{sp}} > 1 \quad (14)$$

where K_{sp} ($\text{mol/l})^2$ is determined following [81] as:

$$\log K_{sp} = -59.3498 - 0.041377T_K - \frac{2.1963}{T_K} + 24.5724 \log(T_K) + 2.518I^{0.5} - 0.6571 \quad (15)$$

where T_K is temperature in Kelvin and I is ionic strength.

In addition, the amount of FeCO_3 formed was calculated from the precipitation rate (PR) expression taken from [44]:

$$PR = \frac{\alpha}{V} e^{\alpha - \frac{\beta}{RT_K}} \frac{A}{V} (S - 1) \quad (16)$$

where α and β are constants, 28.2 and 64.85 J/mol, respectively, V is volume (m^3), R is the gas constant (8.314 J/mol.K), and A is the surface area (m^2). The steps of the

calculations are demonstrated by the flowchart shown in Figure 5. We start by calculating water chemistry at the desired temperature using Equation (3) - (9). Then, the saturation level (S) is calculated using Equation (14) - (15). If S is larger than 1, the precipitation rate and the amount of Fe^{2+} consumed by the FeCO_3 precipitation will be calculated using Equation (16). Finally, the water chemistry is recalculated using Equation (3) - (7) and (11) - (13).

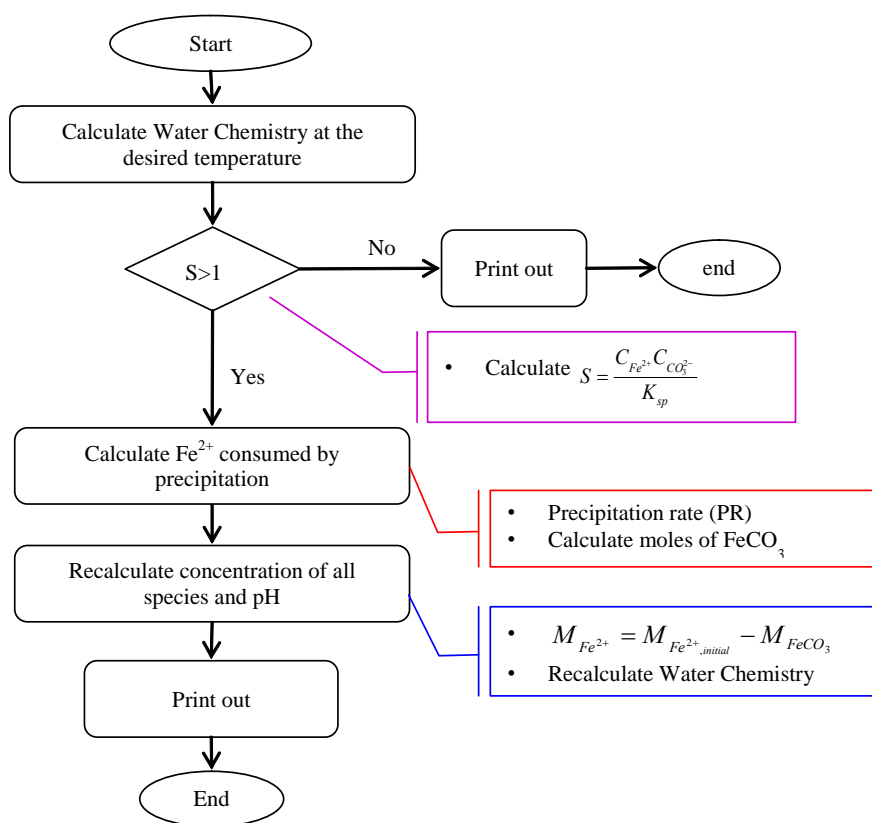


Figure 5. Steps of pH calculation with the effect of FeCO_3 .

2.3 Experimental validation

2.3.1 Experimental setup

The autoclave schematic is shown in Figure 6. It consists of a 2-liter autoclave, thermocouple, temperature controller, pressure gauge, pH electrode, reference electrode, gas inlet and outlet valves.

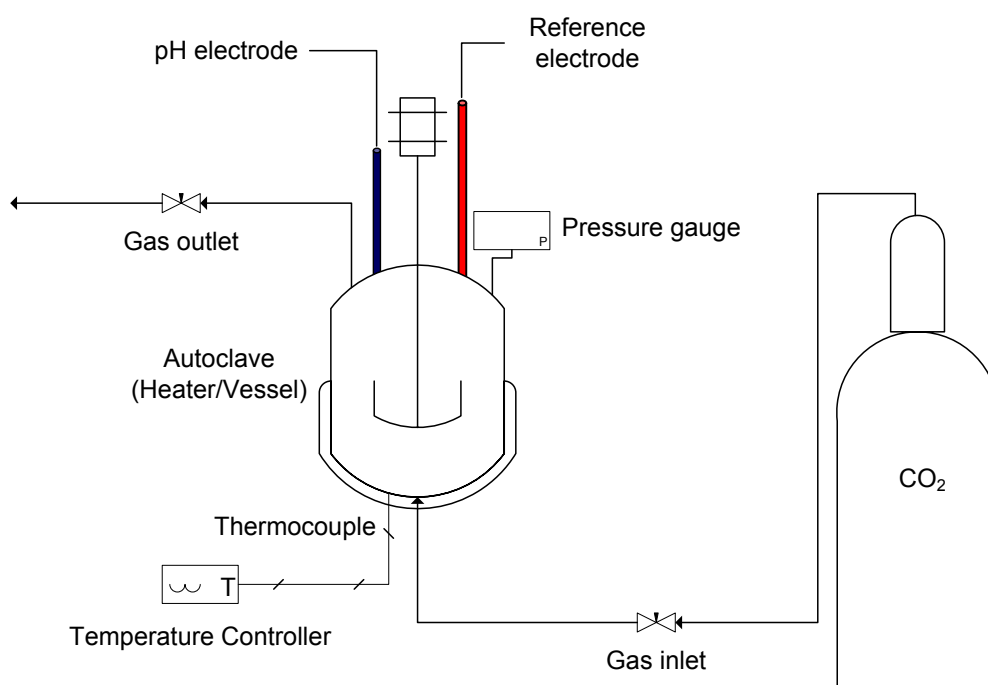


Figure 6. Experimental setup for water chemistry validation.

2.3.2 Experimental procedure

The experimental verification of water chemistry with the effect of Fe^{2+} was carried out in a 2-liter autoclave with a 1 wt.% NaCl solution. Initially, the solution was purged with CO_2 at 25°C until no change of pH was observed, i.e., the solution was saturated with CO_2 . Then, a deoxygenated aqueous $\text{FeCl}_2 \cdot 4\text{H}_2\text{O}$ solution was added into

the system to increase the dissolved Fe^{2+} concentration, and the gas inlet valve was closed. The autoclave was then heated-up to the desired test temperature. Each experimental data point was developed from a single test using a closed system starting at 25°C that was heated to the test temperature and held constant for 6 hours. This was deemed a steady state (equilibrium) as less than 0.02 of pH change was observed after 6 hours. Then the pH of the solution was taken. Two types of pH electrodes (see Appendix A: Experimental Techniques for details and calibrations) were used; glass-based for 25-130°C and ZrO_2 -based for 90-250°C. Test temperatures were in an operating range of 25-250°C. The full experimental conditions are listed in Table 3.

Table 3. Test matrix for the water chemistry validation experiments.

Parameter	Description
System	2-L static autoclave
Solution	1 wt.% NaCl
pCO ₂ initial at 25°C (bar)	0.97
Temperature (°C)	25-250
Aqueous Fe^{2+} concentration (ppm)	0, 100, 1000, 11000

2.4 Results and discussion

Since experiments were conducted in a 2-liter autoclave, this satisfied the closed system conditions. The effect of temperature on pH is shown in Figure 7. The results show that pH increases with temperature due to an increase in the CO_2 solubility.

Furthermore, the predicted data for a closed system are consistent with the experimental results.

The temperature effect on the total pressure is shown in Figure 8a. The total pressure increases with temperature due to vaporization of water. The calculated total pressure agrees with the measured values. Figure 8b. shows the effect of temperature on partial pressure of CO_2 , which is determined by subtracting the vapor pressure of water [82] from the total pressure.

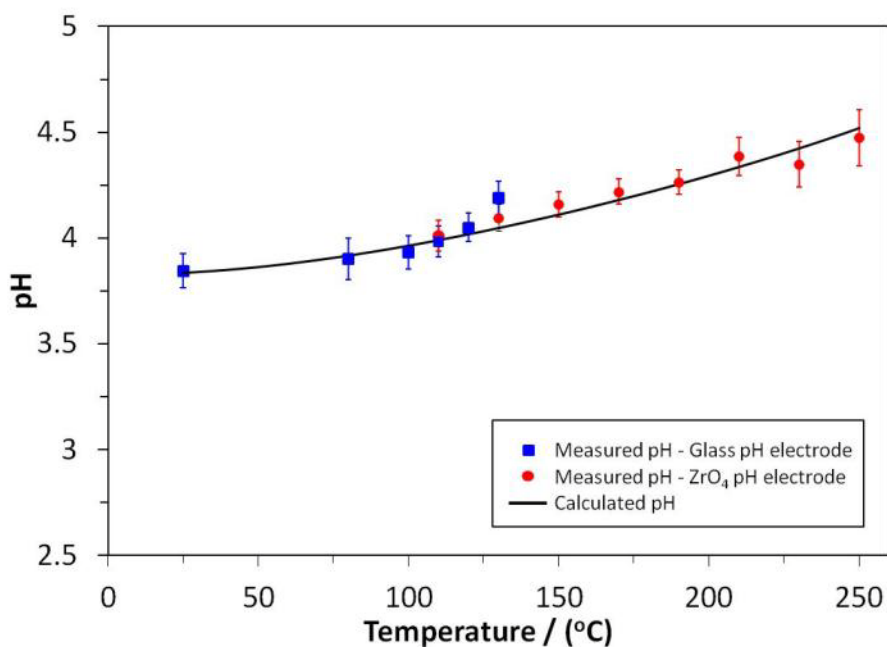
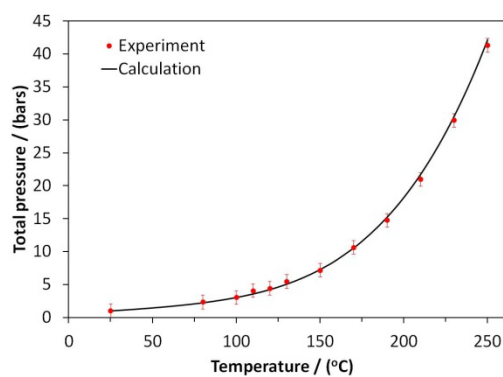


Figure 7. Effect of temperature on pH for the $\text{CO}_2\text{-H}_2\text{O}$ system; 1 wt.% NaCl, $p\text{CO}_2 = 1$ bar at 25°C .



a. Total pressure

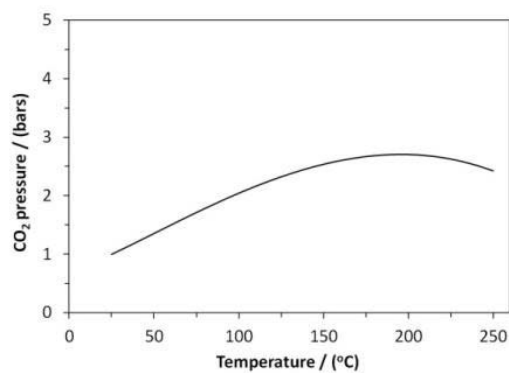
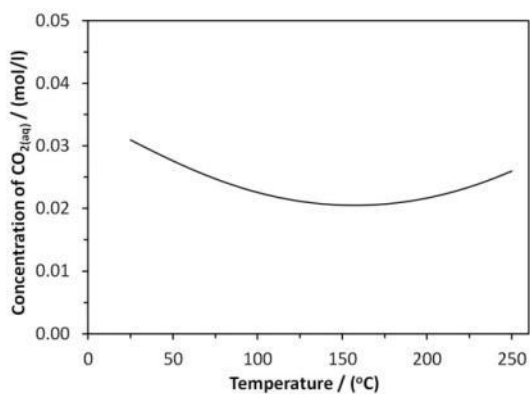
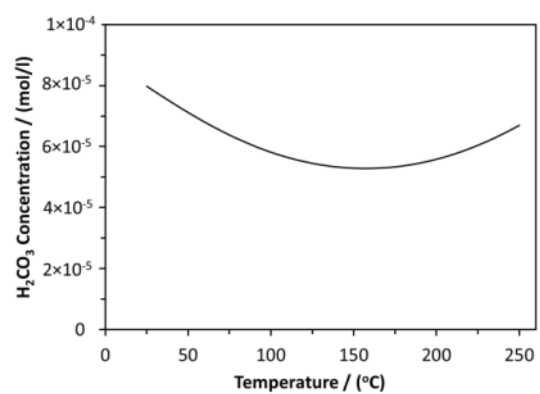
b. CO₂ partial pressure

Figure 8. Temperature effects on pressure for the CO₂-H₂O systems; 1 wt.% NaCl, pCO₂= 1 bar at 25°C.

a. CO₂ concentration in solutionb. H₂CO₃ concentration

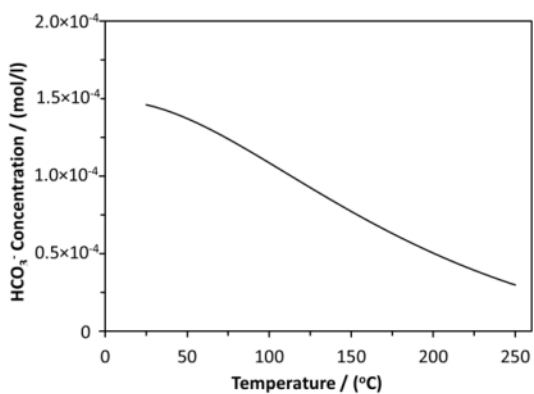
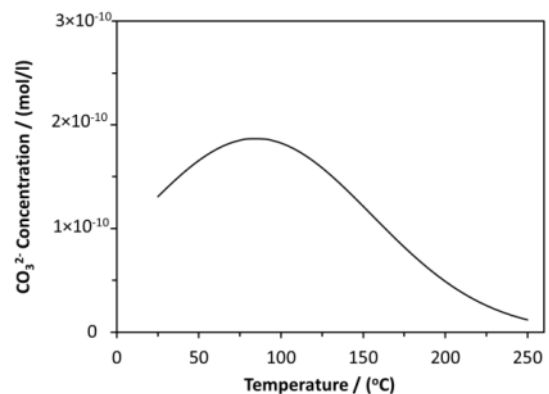
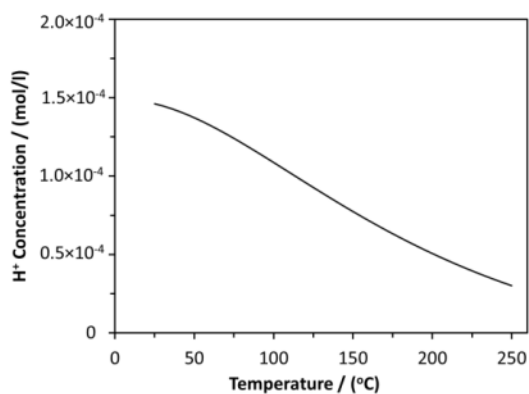
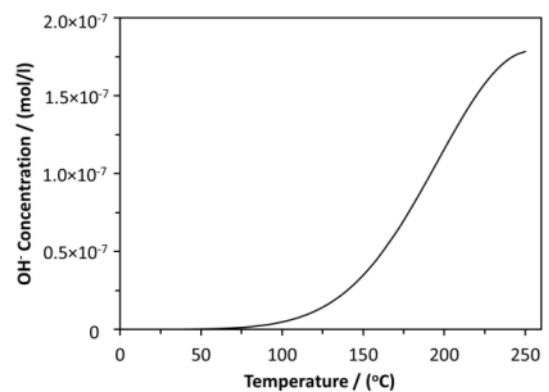
c. HCO_3^- concentrationd. CO_3^{2-} concentratione. H^+ concentrationf. OH^- concentration

Figure 9. The calculated concentrations of species in the CO_2 -saturated solution vs. temperature; 1 wt.% NaCl, $p\text{CO}_2 = 1$ bar at 25°C .

Figure 9 shows the relation between the concentrations of species in the CO_2 -saturated solution and temperature. These values were predicted based on the equilibrium constants listed in Table 2. For CO_2 and H_2CO_3 concentrations, the character of the curves resulted from Henry's Law. HCO_3^- concentration decreases with temperature due to the bicarbonate dissociation. CO_3^{2-} concentration increases and then decreases with

temperature caused by the bicarbonate dissociation. For H^+ concentration, it steadily decreases with temperature, while OH^- concentration increases with temperature.

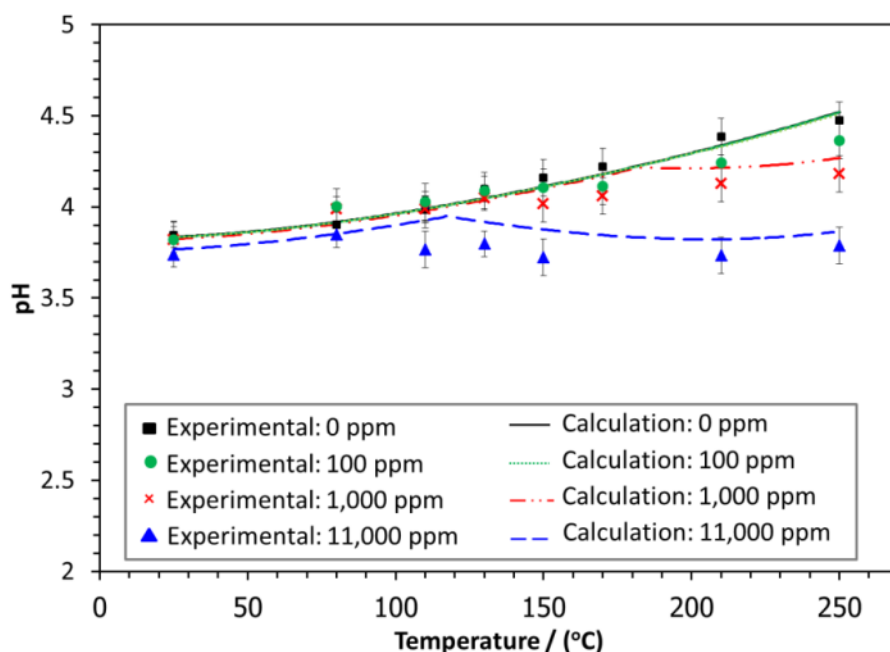


Figure 10. Comparison of the predictive model results and experimental results: pH vs temperature at the different concentrations of Fe^{2+} ; 1 wt.% NaCl, $pCO_2 = 1$ bar at 25°C.

For the water chemistry of Fe^{2+} - CO_2 - H_2O systems, the effect of temperature on pH at different concentrations of Fe^{2+} is shown in Figure 10. The lines show the calculated values, and the points show the experimental data. In the absence of Fe^{2+} , both predicted and experimental results show that pH increased with temperature. At 100 ppm of Fe^{2+} , pH also increased with temperature, which had the same trend as the Fe^{2+} free condition. Yet the predicted line did not show any $FeCO_3$ precipitation. At 1,000 ppm

and 11,000 ppm of Fe^{2+} , pH increased with temperature. However, pH did not change with temperature after the saturation level ($S \geq 1$) was reached since FeCO_3 precipitated. After FeCO_3 precipitated, carbonate species were consumed. As a consequence, the equilibrium position changed. In other words, the reactions, Equation (3)-(6), shifted forward resulting in generation of more hydrogen ions. From the model, FeCO_3 started precipitating at around 180°C and 117°C for 1,000 and 11,000 ppm of Fe^{2+} , respectively.

Table 4. Relationship between pH and dissolved CO_2 with temperature.

T (°C)	Set 1: Glass Cell			Set 2: Autoclave			Set 3: Autoclave		
	Const. P_{total} 1 bar			Set $p\text{CO}_2$ 1 bar @ 25°C			Const. $\text{CO}_{2,\text{aq}}$ 0.030M		
	$p\text{CO}_2$ (bar)	$\text{CO}_{2,\text{aq}}$ (M)	pH	$p\text{CO}_2$ (bar)	$\text{CO}_{2,\text{aq}}$ (M)	pH	$p\text{CO}_2$ (bar)	$\text{CO}_{2,\text{aq}}$ (M)	pH
25	0.97	0.030	3.84	1.00	0.030	3.84	0.97	0.030	3.84
50	0.88	0.018	3.96	1.38	0.028	3.86	1.27	0.030	3.84
80	0.53	0.007	4.18	1.86	0.025	3.91	2.21	0.030	3.87
120	-	-	-	2.41	0.023	4.01	3.2	0.030	3.94
150	-	-	-	2.70	0.022	4.10	3.71	0.030	4.03
200	-	-	-	2.78	0.023	4.28	3.76	0.030	4.22
250	-	-	-	2.50	0.027	4.52	2.8	0.030	4.49

To summarize the speciation of CO_2 systems, Table 4 demonstrates the relationship between pH and the concentration of dissolved CO_2 with temperature in

three different experimental systems used within this series of experiments. Firstly, in a hypothetical glass cell test system (as tested in Section 4.3.1) the total pressure is always atmospheric: 1 bar. Once the temperature increases, the partial pressure of CO₂ will decrease due to an increase in vapor pressure of water. Consequently, the concentration of dissolved CO₂ decreases, while the pH increases.

When the partial pressure of CO₂ in a closed autoclave system is set to 1 bar at 25°C (as was done in the water chemistry validation experiments above and in Section 3.3 for the study of temperature effects) the partial pressure of CO₂ and pH increase due to the decrease in solubility of CO₂ when temperature increases, therefore the concentration of dissolved CO₂ also decreases.

Finally, the concentration of dissolved CO₂ can be maintained at 0.030M at all temperatures. This approach was used in Chapter 4, kinetics and corrosion study shown below. In this condition, the partial pressure of CO₂ is adjusted in an autoclave system to control the concentration of dissolved CO₂ at different temperatures since the concentration of dissolved CO₂ corresponds to the total amount of acid in the system and directly affects corrosion.

2.5 Summary

The behavior of CO₂-H₂O-NaCl closed systems was investigated in the range of 25-250°C. The pH was modeled using the homogeneous chemical reactions at equilibrium, which was verified by experiments using high temperature pH measurements. In the absence of Fe²⁺, both predicted and experimental results show that

pH increased with temperature. With addition of Fe^{2+} , pH did not change with temperature once FeCO_3 precipitated.

Chapter 3: Electrochemical Thermodynamics of Fe-CO₂-H₂O Systems at Elevated Temperatures

3.1 Introduction

As noted above, one of the important factors in CO₂ corrosion phenomena is the morphology and identity of the corrosion product layer. Some previous research has indicated the effect of temperature on the CO₂ corrosion product layers to be as follows:

- At temperatures lower than 60°C, no corrosion product layer is formed [7], [15], [24], [61]. However, at high pH, additional more complex carbonate compounds, including Fe₂(OH)₂CO₃, Fe₆(OH)₁₂CO₃, Fe₆(OH)₁₂CO₃•H₂O and Fe₂O₂CO₃, have been proposed to form as corrosion products at temperatures from 20°C to 40°C [62].
- At temperatures greater than 60°C, Fe₂(OH)₂CO₃ was detected in the corrosion product layer [83].
- At 100°C, trace amounts of Fe₃O₄/Fe(OH)₂ were observed in the FeCO₃ dominant corrosion product [84].
- At temperatures between 60°C and 130°C pitting corrosion occurs and the corrosion product consists of thick, prismatic crystals of FeCO₃ [9], [30], [32], [85].
- At temperatures between 130°C and 200°C, the fine grained, dense, adherent corrosion product layer that has been observed is composed of FeCO₃ and Fe₃O₄ [24], [30], [31], [86].

As indicated above by the few key studies listed, many questions and uncertainties surround the corrosion product layer formation in CO₂ corrosion of mild steel at high temperatures. This ambiguity in the open literature indicates that more

research needs to be done in order to elucidate the nature of corrosion products formed in CO₂ corrosion of mild steel in the temperature range of 25-250°C.

The potential-pH, or Pourbaix, diagram is a well-known tool for displaying the most stable corrosion product based on thermodynamic theory. The Pourbaix diagrams for metal-water systems at 25°C have been established for various metals in the Atlas of Electrochemical Equilibria in Aqueous Solutions [87], [88]. Some authors have developed Pourbaix diagrams for an Fe-H₂O system at elevated temperatures with Fe, Fe²⁺, Fe₃O₄, Fe(OH)₂, Fe₂O₃ and FeO(OH) considered as the most stable species [87], [89–92]. Many extensions of the basic Pourbaix diagrams for a Fe-H₂O system that include CO₂ are available freely and as commercial software packages. They can predict the most stable iron species for a bicarbonate/carbonate (HCO₃⁻/CO₃²⁻) aqueous system by using a specified concentration of HCO₃⁻ and then cover the full range of pH.

However, this does not directly relate to a practical system where one typically has a constant aqueous concentration of dissolved CO₂, rather than a constant HCO₃⁻ concentration. When a corrosion engineer is interested in the effect of CO₂ on corrosion of mild steel, the aqueous concentration of CO₂ is assumed to be constant and known, since it can be easily calculated as a function of temperature and partial pressure of CO₂. When considering the equilibrium state of a CO₂ system, the concentrations of HCO₃⁻/CO₃²⁻ will vary widely with pH, for a constant concentration of dissolved CO₂. Therefore, in this research the potential-pH diagrams for an Fe-CO₂-H₂O system were developed for a constant temperature and partial CO₂ pressure (*i.e.*, constant concentration of dissolved CO₂). The starting point was the open literature data/diagrams

for a simpler Fe-H₂O system at elevated temperatures [91]. Subsequently, additional species were introduced due to the presence of CO₂. In addition, those diagrams were correlated with surface characterization of CO₂ corrosion products formed on mild steel in the temperature range from 25°C to 250°C.

3.2 Thermodynamic background

3.2.1 Electrochemical thermodynamics

Since corrosion is an (electro)chemical process involving reduction/oxidation reactions, it can be described using a thermodynamics framework. An electrochemical reaction is composed of one oxidized species (X^{z+}) and one reduced species (X):



The 1st Law of Thermodynamics for an isobaric isothermal system can be written as:

$$\sum_{i=1}^{\kappa} \mu_i dn_i + Edq = d\tilde{G} \quad (18)$$

where μ_i is the chemical potential of species i , $\sum_{i=1}^{\kappa} \mu_i dn_i$ is the change of the chemical free energy (dG), Edq is the change of the electrical energy, and $d\tilde{G}$ is the total (electrochemical) Gibbs energy change, this equation can be integrated to:

$$\Delta G + zFE = \Delta\tilde{G} \quad (19)$$

where ΔG is the free energy change due to the chemical reaction, zFE is the electrical energy change in the process and $\Delta\tilde{G}$ is the total (electrochemical) free energy for the

system. At overall equilibrium, there is no change of total Gibbs energy ($\Delta \tilde{G} = 0$), so we can write:

$$-\Delta G = zFE_{rev} \quad (20)$$

where E_{rev} is called the reversible potential and indicates the reversibility of the electrochemical process at equilibrium.

To calculate E_{rev} , Equation (20) is substituted into the general expression for Gibbs free energy change of a chemical reaction, Equation (21):

$$\Delta G = \Delta G^o + RT \sum_{i=1}^k \ln(c_i)^{n_i} \quad (21)$$

to obtain the well-known Nernst equation, Equation (22):

$$E_{rev} = E_{rev}^o - \frac{RT}{zF} \sum_{i=1}^{\kappa} \ln(c_i)^{n_i} \quad (22)$$

where E_{rev}^o is the reversible potential as defined at standard conditions using unit concentrations and reference temperature and pressure.

However, the Nernst equation is unable to correct for concentration and temperature simultaneously. To determine the reversible potential of a redox reaction at any temperature, E_{rev}^o is calculated at that temperature, which can be found from the Gibbs energy change ΔG^o . For instance, the Gibbs energy change of reaction for the dissolution of iron, Equation (23), the main anodic reaction in a mild steel corrosion process, is expressed as Equation (24):



$$\Delta G^o = G_{Fe}^o - G_{Fe^{2+}}^o - 2G_{e^-}^o \quad (24)$$

The absolute Gibbs energy of electron, $G_{e^-}^{\circ}$ described by Kaye and Thompson [93] is also considered, written as Equation (25). By definition of the Nernst equation, the reversible potential at 1 bar of H_2 and 1 molar of H^+ concentration (pH=0.0) is zero at any temperature. This means the Gibbs free energy of the H_2 oxidation/reduction (Equation (26)), is zero at all temperatures (ΔG° of Equation (27) = 0). From Table 5, the absolute Gibbs energy of H^+ ($G_{H^+}^{\circ} = 0$) is zero at any temperature. Then, the absolute Gibbs energy of electron, $G_{e^-}^{\circ}$ is written as Equation (25):

$$G_{e^-}^{\circ} = \frac{1}{2}G_{H_2}^{\circ} \quad (25)$$



$$\Delta G^{\circ} = G_{H_2}^{\circ} - 2G_{H^+}^{\circ} - 2G_{e^-}^{\circ} \quad (27)$$

The absolute Gibbs energy for each species, G° , Equation (28), at any temperature can be determined using the 1st and 2nd Law of Thermodynamics (Equation (29) - (32)):

$$\Delta G = \Delta G^{\circ} + \int_{298.15}^T C_p dT - T \int_{298.15}^T \frac{C_p}{T} dT - \Delta T \cdot S^{\circ} \quad (28)$$

$$dG = dH - d(TS) \quad (29)$$

$$dH = C_p dT \quad (30)$$

$$dS = \frac{C_p}{T} dT \quad (31)$$

where C_p is heat capacity, S is entropy and H is enthalpy. In this work, the species considered and their respective thermodynamic data are presented in Table 5.

Table 5. Thermodynamic data for the Fe-CO₂-H₂O system.

Species	G°_{298K} (kJ/mol)	S°_{298K} (J/mol/K)	$C_p = a + bT + cT^{-2} + dT^2 + eT^{-0.5}$ (J/mol/k)					Ref.
			a	$b \times 10^3$	$c \times 10^{-6}$	$d \times 10^3$	$e \times 10^{-4}$	
Fe _(s)	0.0	27.28	28.18	-7.32	-0.290	0.0250	0.0	[91]
Fe(OH) _{2(s)}	-491.98	88.0	116.06	8.648	-2.874	0.0	0.0	[91]
Fe ₃ O _{4(s)}	-1,012.6	146.14	2659.1	-2521.53	20.734	1.368	-3.646	[91]
Fe ₂ O _{3(s)} *	-744.3	87.40	-838.61	-2343.4	0.0	0.605	0.0	[91]
FeO(OH) _(s)	-485.3	60.4	49.37	83.68	0.0	0.0	0.0	[91]
Fe(OH) _{3(s)}	-705.3	106.7	127.61	41.639	-4.217	0.0	0.0	[91]
Fe ³⁺ _(aq)	-17.8	-276.94	-143	0.0	0.0	0.0	0.0	[91]
Fe ²⁺ _(aq)	-91.88	-105.6	-2.0	0.0	0.0	0.0	0.0	[91]
Fe(OH) ₂ ⁺ _(aq)	-459.50	8.0	230.0	0.0	0.0	0.0	0.0	[91]
FeCO _{3(s)}	-680.3	95.47	257.38	-0.0462	1.523	0.0	-3.082	[94]
H ⁺ _(aq)	0.0	0.0	0.0	0.0	0.0	0.0	0.0	[95]
OH ⁻ _(aq)	-157.2	-10.878	506.77	-1.181	-24.60	0.0	0.0	[95]
H ₂ O _(l)	-237.1	70.01	20.36	109.2	2.03	0.0	0.0	[95]
H _{2(g)}	0.0	130.7	26.88	3.59	0.11	0.0	0.0	[95]
O _{2(g)}	0	205.1	29.15	6.48	-0.18	-1.02	0.0	[95]
CO _{2(g)}	-394.51	213.8	51.13	4.37	-1.47	0.0	0.0	[95]

* $C_{p(Fe_2O_3)} = a + bT + cT^{-2} + dT^2 + fT^{-0.5} + gT^{-1}$ (J/mol/K), where $f = 86.525$ and $g = 2.782 \times 10^4$.

3.2.2 Equilibria in the Fe-CO₂-H₂O System

The equilibrium concentrations of species in a homogenous CO₂-H₂O system can be calculated by simultaneously solving the equations shown in Table 6. Since these chemical reactions are linked *via* the common species (such as H⁺) changing any one concentration will shift the equilibrium concentration for all others. For example, the concentrations of HCO₃⁻ and CO₃²⁻ are dependent on pH, pCO₂ and, of course, temperature (which affects the equilibrium constants). When one includes dissolved iron species in the picture, one other heterogeneous chemical reaction needs to be considered here: the formation of solid ferrous carbonate (FeCO₃). The various ways to represent this chemical reaction in a CO₂-H₂O system are shown in Table 7. They are all thermodynamically equivalent, by combining any one of the reactions from Table 7 with selected reactions shown in Table 6 to get any other reaction in Table 7. Therefore, only one form the heterogeneous ferrous carbonate formation reaction shown in Table 6 needs be used in conjunction with the homogenous chemical reactions listed in Table 7. Finally, we can add in the key electrochemical (reduction/oxidation or redox) reactions possible in a Fe-CO₂-H₂O system and arrive at the complete list of equilibrium reactions considered in construction of the Pourbaix diagrams.

Table 6. Chemical reactions and equilibrium constants for a CO₂-H₂O system.

Name	Reaction	Equilibrium Constant
Dissolution of CO ₂	$CO_{2(g)} \rightleftharpoons CO_{2(aq)}$	$H = \frac{P_{CO_2}}{C_{CO_2}}$
CO ₂ hydration	$CO_{2(aq)} + H_2O_{(l)} \rightleftharpoons H_2CO_{3(aq)}$	$K_h = \frac{C_{H_2CO_3}}{C_{CO_2}}$
H ₂ CO ₃ dissociation	$H_2CO_{3(aq)} + H_2O_{(l)} \rightleftharpoons H_{(aq)}^+ + HCO_{3(aq)}^-$	$K_{a1} = \frac{C_{HCO_3^-} C_{H^+}}{C_{H_2CO_3}}$
HCO ₃ ⁻ dissociation	$HCO_{3(aq)}^- + H_2O_{(l)} \rightleftharpoons H_{(aq)}^+ + CO_{3(aq)}^{2-}$	$K_{a2} = \frac{C_{CO_3^{2-}} C_{H^+}}{C_{HCO_3^-}}$

Table 7. Examples of the reactions representing FeCO₃ precipitation.

Reaction	Equilibrium Constant
$FeCO_{3(s)} + 2H^+_{(aq)} \rightleftharpoons Fe^{2+}_{(aq)} + H_2O_{(l)} + CO_{2(g)}$	$K_{sp1} = \frac{P_{CO_2} c_{Fe^{2+}}}{c_{H^+}}$
$FeCO_{3(s)} + 2H^+_{(aq)} \rightleftharpoons Fe^{2+}_{(aq)} + H_2CO_{3(aq)}$	$K_{sp2} = \frac{c_{H_2CO_3} c_{Fe^{2+}}}{c_{H^+}^2}$
$FeCO_{3(s)} + H^+_{(aq)} \rightleftharpoons Fe^{2+}_{(aq)} + HCO_{3(aq)}^-$	$K_{sp3} = \frac{c_{HCO_3^-} c_{Fe^{2+}}}{c_{H^+}}$
$FeCO_{3(s)} \rightleftharpoons Fe^{2+}_{(aq)} + CO_{3(aq)}^{2-}$	$K_{sp4} = c_{CO_3^{2-}} c_{Fe^{2+}}$

3.2.3 Pourbaix diagrams

All the reactions, chemical and electrochemical, considered in the present study are listed in Table 8, along with the oxygen and hydrogen reactions. To construct a Pourbaix diagram, the Nernst equation is used for electrochemical reactions, and simple equilibrium expressions are used for the chemical reactions. In the third column, the Nernst expression for the reversible potential is given for the electrochemical reactions while the equilibrium pH is shown for the chemical reactions.

For example, at the reversible potential for iron deposition/dissolution (Reaction (1) in Table 8), the reaction is in equilibrium and no corrosion or loss of Fe^{2+} is occurring. However, if the potential is higher than the reversible potential of this reaction, then reaction (1) proceeds from right-to-left more than from left-to-right and iron corrodes. In contrast, if the potential is lower than the reversible potential of this reaction, then reaction (1) proceeds more from left-to-right and deposits iron in a reduction reaction.

An example of a Pourbaix diagram for an Fe-H₂O system at 25°C was generated using thermodynamic data given in Table 5 and is shown in Figure 11. The lines *H* and *O* correspond to the equilibrium redox potential of hydrogen and oxygen evolution at 1 bar of H₂ and O₂, respectively. Where the stable state of iron is ferrous ion, Fe^{2+} , (the area under the line *H* and above the Fe boundary) in deaerated acidic, neutral, or mildly alkaline conditions, spontaneous corrosion of steel will occur. For higher pH, the layer of solid $\text{Fe}(\text{OH})_2$ or Fe_3O_4 will form on the surface of the steel (the area under the line *H* and above the Fe boundary) which may give some degree of protection from active corrosion.

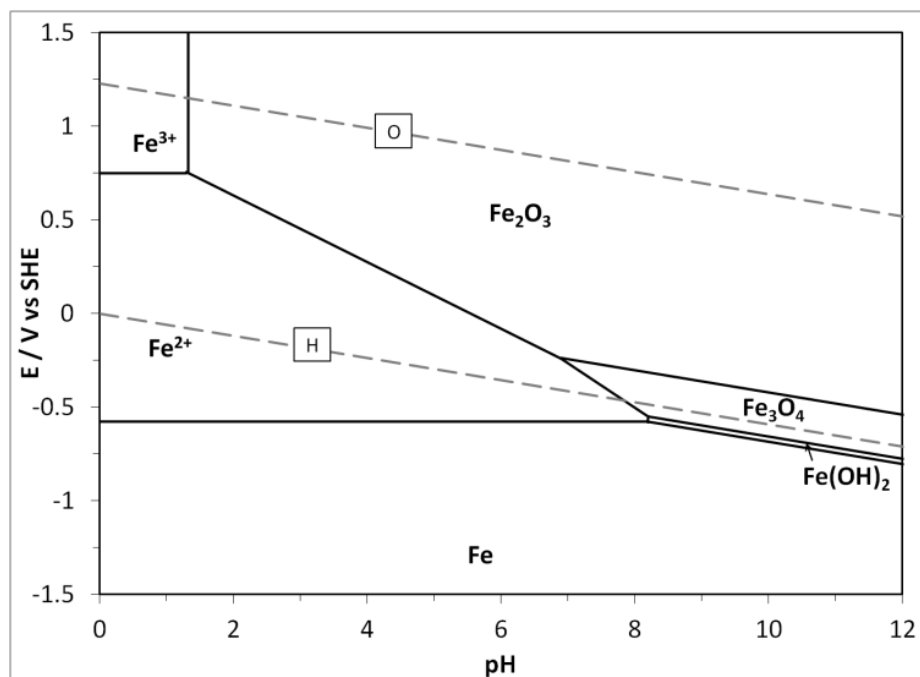
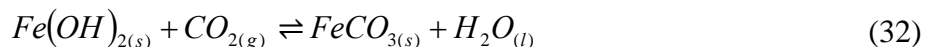


Figure 11. Example of a Pourbaix diagram for an Fe-H₂O system at 25°C;

$$c\text{Fe}^{2+} = 10 \text{ ppm}, c\text{Fe}^{3+} = 10 \text{ ppm}, p\text{H}_2 = 1 \text{ bar}, p\text{O}_2 = 1 \text{ bar}.$$

An example of the Pourbaix diagrams for an Fe-CO₂-H₂O system at 25°C is shown in Figure 12 a. Based on experimental results (described in Section 2.3), 10 ppm of Fe²⁺ was arbitrarily selected to generate the Pourbaix diagram shown. In a deaerated acidic condition, Fe²⁺ is the most thermodynamically stable state of iron. For mildly acidic and alkaline regions, the dotted lines show that FeCO₃, Fe(OH)₂ and Fe₃O₄ can coexist. However, FeCO₃ is the most thermodynamically stable species of the three (i.e. it has the lowest Gibbs free energy). The other two species must therefore be considered as metastable, *i.e.*, they would eventually be transformed into FeCO₃. This can be seen by inspection of the thermodynamic data in Table 5, where the standard free energy of formation for FeCO₃ is more negative than that of, for example, Fe(OH)₂. This means

$\text{Fe}(\text{OH})_2$ is unstable with respect to FeCO_3 , *i.e.*, $\text{Fe}(\text{OH})_2$ will eventually convert into FeCO_3 , via Reaction (32):



$$\Delta G^\circ = -27.5 \text{ kJ/mol}$$

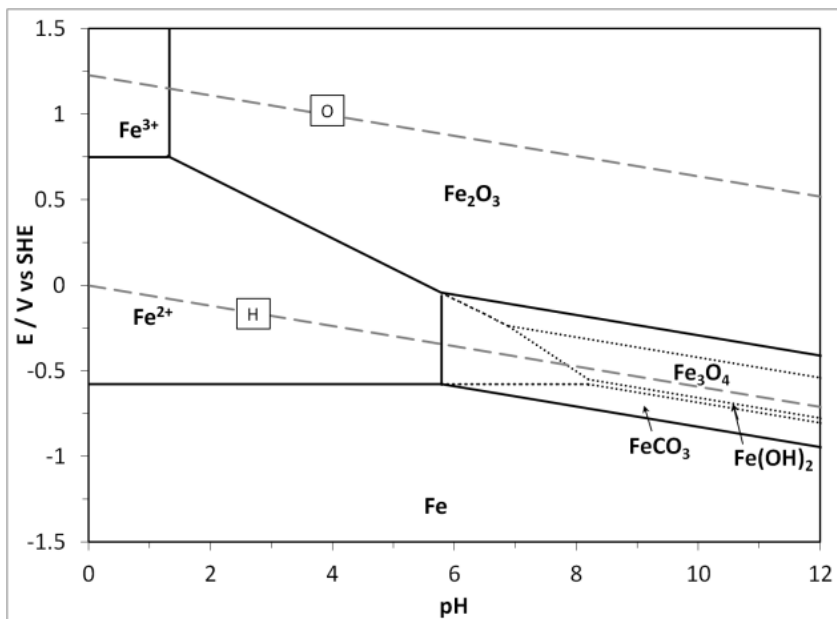
The same strategy can also be applied to determine the relative stability of FeCO_3 vs. Fe_3O_4 ; it is found that the former is more stable, *i.e.*, all Fe_3O_4 would eventually convert into FeCO_3 at this condition.

Using the same methodology, the diagrams for Fe-CO₂-H₂O systems at temperatures of 80, 100, 120, 150, 200 and 250°C are constructed as shown in Figure 12 b. – Figure 12 g. By inspection of these Pourbaix diagrams, two conclusions can be made with respect to the nature of the corrosion product, as a function of pH and temperature:

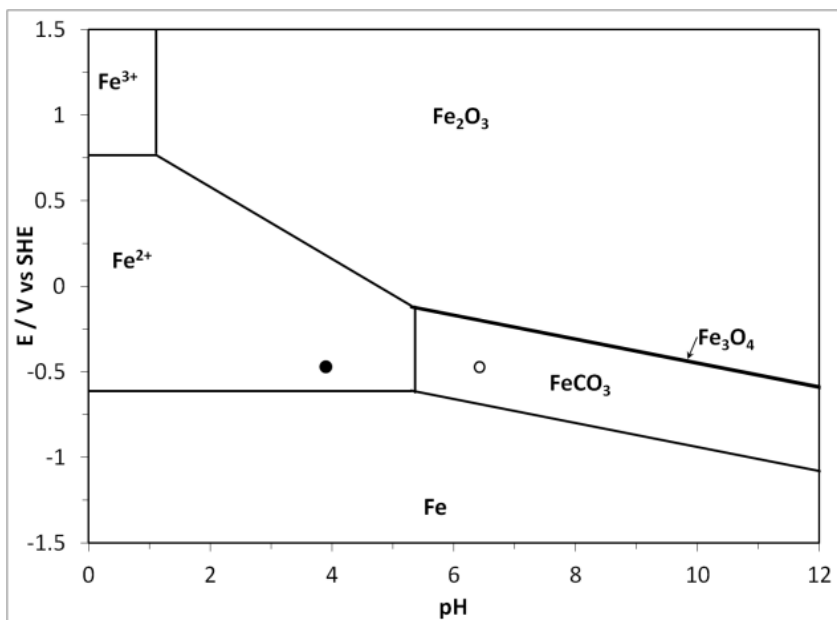
- As the temperature increases, the solubility line of FeCO_3 shifts to the left increasing the possibility of formation/precipitation at lower pH. In other words, at higher temperature FeCO_3 is stable at lower pH.

- At temperatures below 80°C, the stable state of iron in acidic conditions is Fe^{2+} and in neutral and alkaline conditions it is FeCO_3 . As the temperature increases up to 250°C, Fe_3O_4 becomes the more stable product in neutral and alkaline conditions.

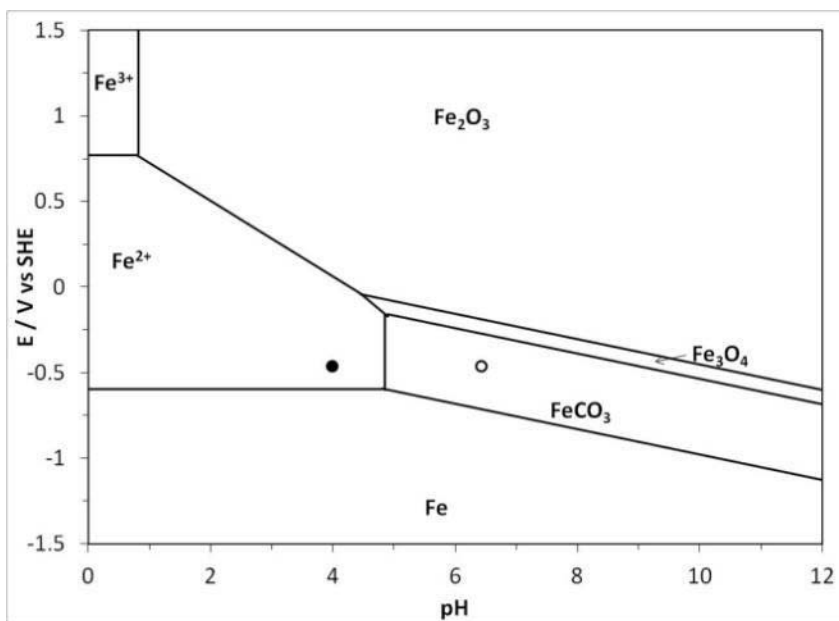
The generated Pourbaix diagrams were in broad agreement with those reported by Ueda [86] and Nishimura and Dong [96] for the same conditions. New experiments were conducted in the present study to further verify the validity of the constructed Pourbaix diagrams, particularly for higher temperatures (80 – 250°C).



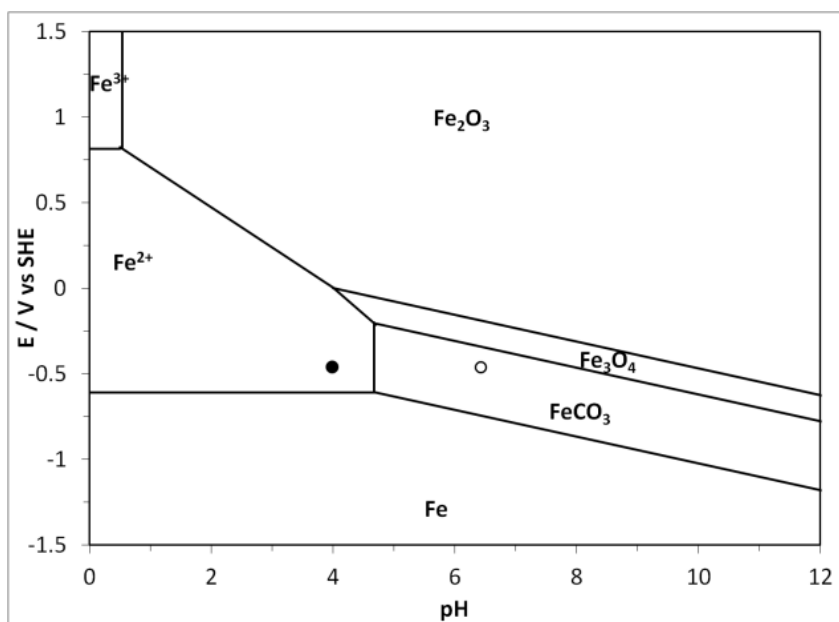
a. 25°C



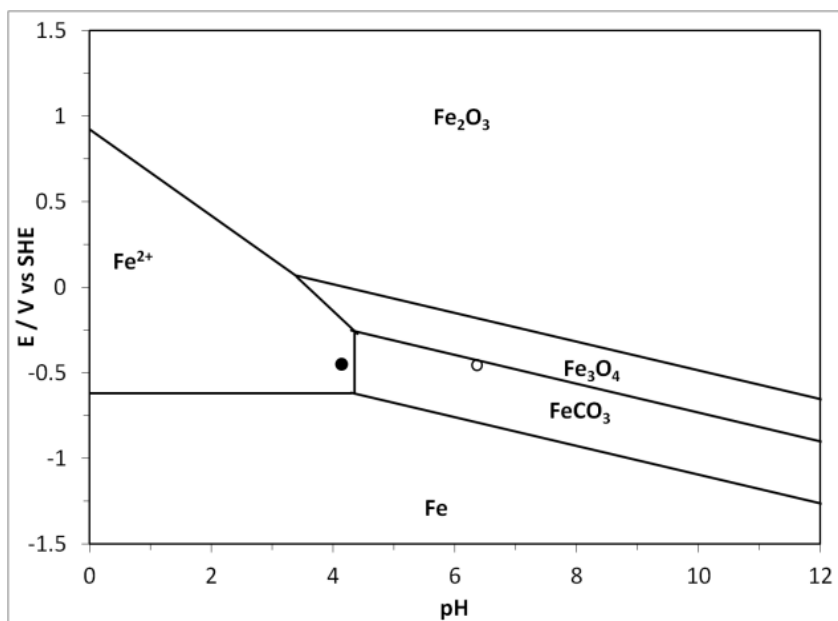
b. 80°C



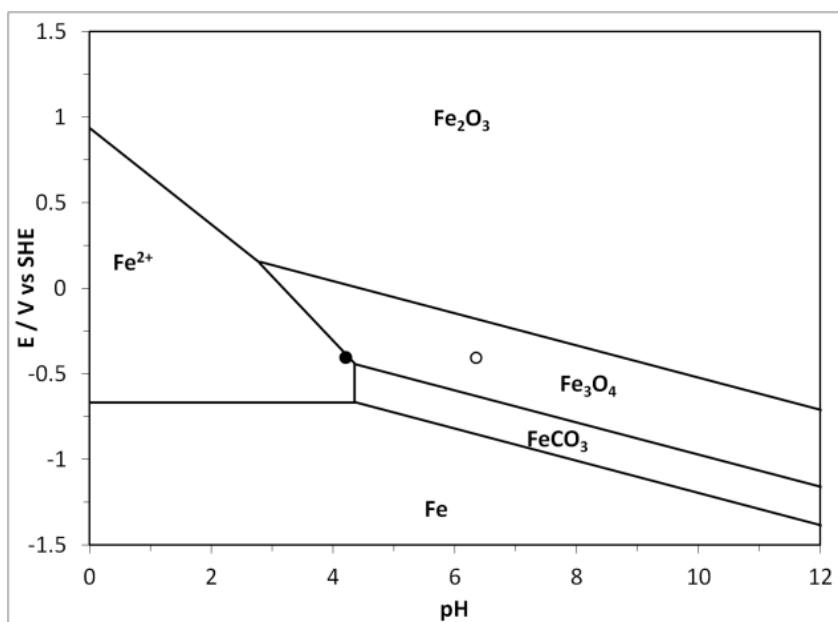
c. 100°C



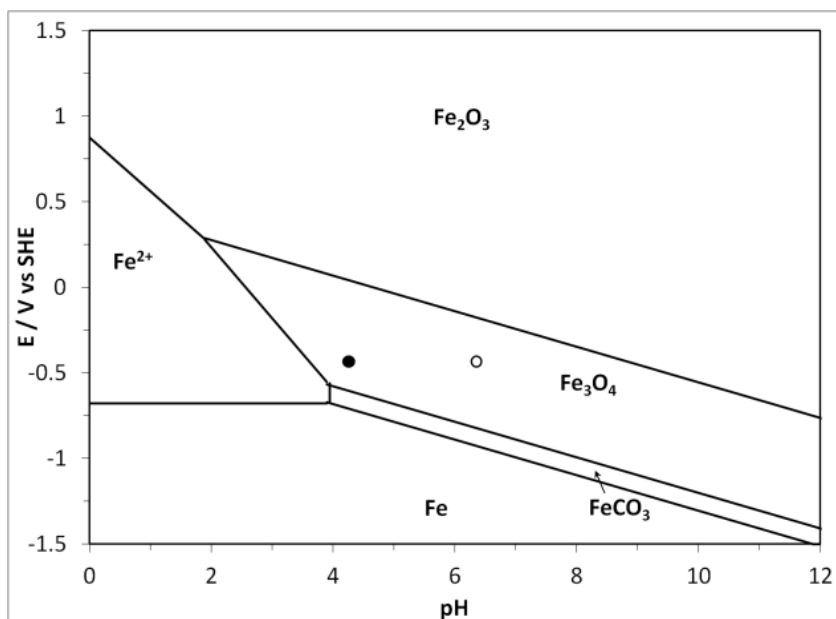
d. 120°C



e. 150°C



f. 200°C



g. 250°C

Figure 12. Generated Pourbaix diagrams for Fe-CO₂-H₂O systems corresponding to the experimental conditions given in Table 5; $c\text{Fe}^{2+}=10$ ppm, $c\text{Fe}^{3+}=10$ ppm, $p\text{H}_2=1$ bar, $p\text{O}_2=1$ bar, (symbols: • - typical bulk pH, o - corresponding surface pH in stagnant conditions).

To summarize the construction of Pourbaix diagrams, Figure 13 shows the potential-pH-temperature diagram for Fe-CO₂-H₂O systems. In practical conditions for CO₂ corrosion, around -0.5 V of potential, the stable states of iron are Fe²⁺, FeCO₃, and Fe₃O₄ shown in Figure 14.

There are other, possibly more effective ways of displaying the same thermodynamic data, other than the Pourbaix (E-pH) diagrams. For example one can construct a three-dimensional E-T-pH diagram or a simpler and more practical T-pH diagram, as illustrated in the graphs below. There, one can clearly see that the area of

FeCO_3 becomes larger, as FeCO_3 forms at lower pH, when increasing the amount of dissolved Fe^{2+} (Figure 14 a. – c.) or the partial pressure of CO_2 (Figure 15 a. – c.),

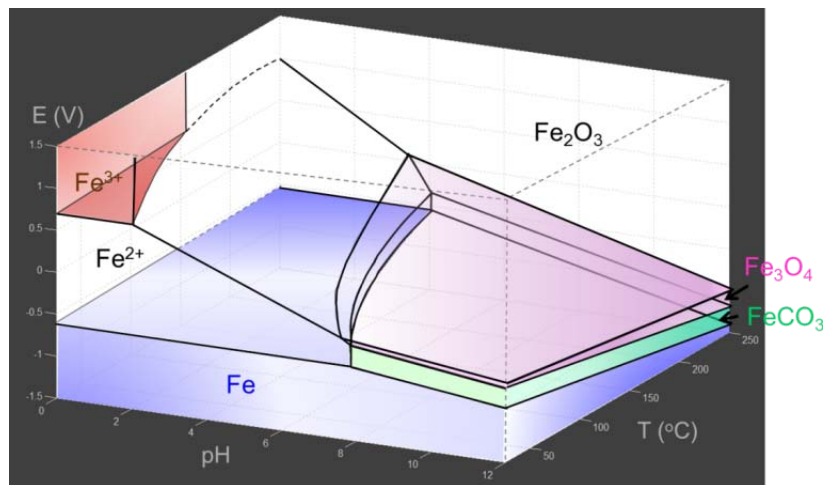
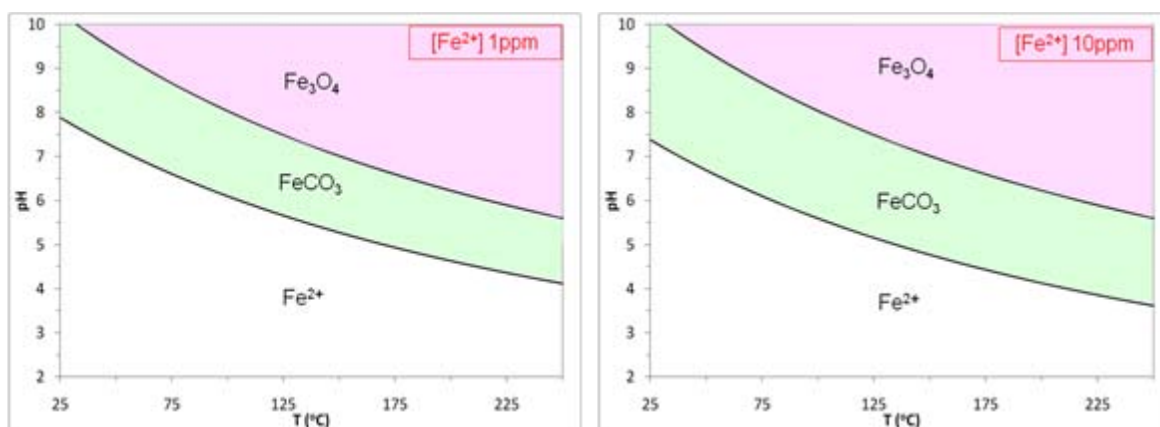


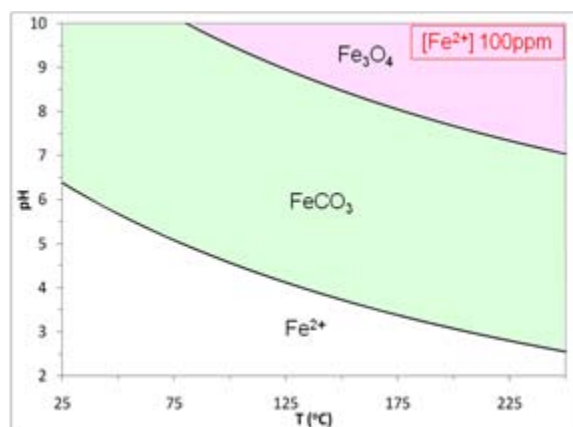
Figure 13. Potential-pH-temperature diagram for Fe- CO_2 - H_2O systems;

$$c\text{Fe}^{2+} = 1 \text{ ppm}, p\text{CO}_2 = 1 \text{ bar}.$$



a. $c\text{Fe}^{2+} = 1 \text{ ppm}$, $p\text{CO}_2 = 1 \text{ bar}$

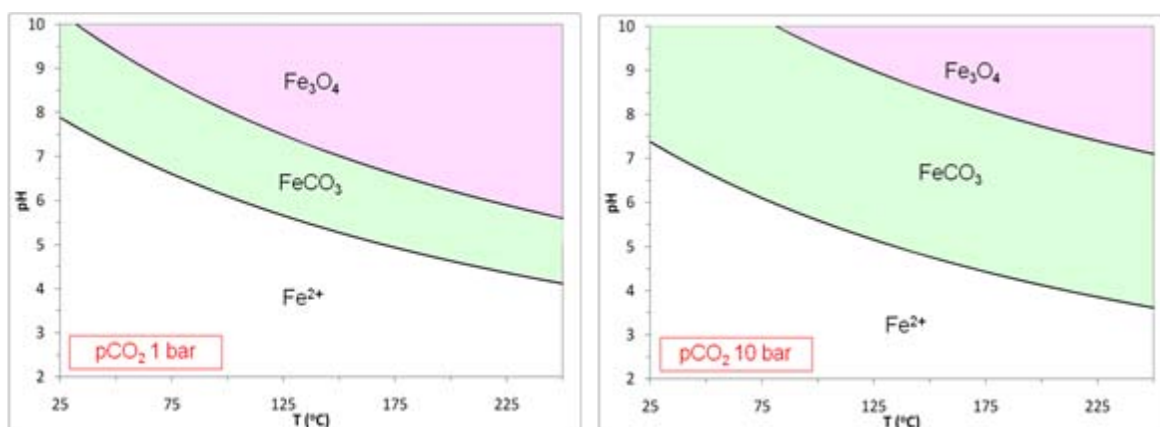
b. $c\text{Fe}^{2+} = 10 \text{ ppm}$, $p\text{CO}_2 = 1 \text{ bar}$



c. $c\text{Fe}^{2+} = 100 \text{ ppm}$, $p\text{CO}_2 = 1 \text{ bar}$

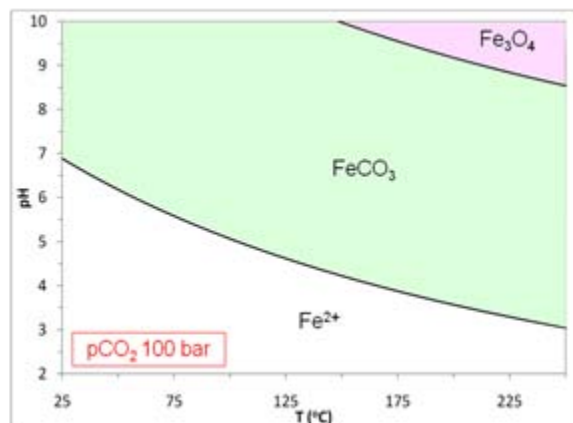
Figure 14. pH-temperature diagrams at $E = -0.5 \text{ V}$, $p\text{CO}_2 = 1 \text{ bar}$; a. $c\text{Fe}^{2+} = 1 \text{ ppm}$, b.

$c\text{Fe}^{2+} = 10 \text{ ppm}$ and c. $c\text{Fe}^{2+} = 100 \text{ ppm}$.



a. $c\text{Fe}^{2+} = 1 \text{ ppm}$, $p\text{CO}_2 = 1 \text{ bar}$

b. $c\text{Fe}^{2+} = 1 \text{ ppm}$, $p\text{CO}_2 = 10 \text{ bar}$



f. $c\text{Fe}^{2+} = 1 \text{ ppm}$, $p\text{CO}_2 = 100 \text{ bar}$

Figure 15. pH-temperature diagrams at $E = -0.5 \text{ V}$, $c\text{Fe}^{2+} = 1 \text{ ppm}$; a. $p\text{CO}_2 = 1 \text{ bar}$, b. $p\text{CO}_2 = 10 \text{ bars}$ and c. $p\text{CO}_2 = 100 \text{ bars}$.

Table 8. Key reactions considered in the Pourbaix diagrams for iron along with the expressions for their equilibrium (reversible) potential or pH.

No.	Reaction	Equilibrium Potential in V or pH
H	$2H_2O + 2e^- \rightleftharpoons H_2 + 2OH^-$	$E_{rev(H^+/H_2)} = \frac{RT}{2F} \ln \left(\frac{c_{H^+}^2}{p_{H_2}} \right)$
O	$O_2 + 4H^+ + 4e^- \rightleftharpoons 2H_2O$	$E_{rev(O_2/H_2O)} = E_{rev(O_2/H_2O)}^o + \frac{RT}{4F} \ln(p_{O_2} c_{H^+}^4)$
1.	$Fe^{2+} + 2e^- \rightleftharpoons Fe$	$E_{rev(Fe^{2+}/Fe)} = E_{rev(Fe^{2+}/Fe)}^o + \frac{RT}{2F} \ln(c_{Fe^{2+}})$
2.	$Fe^{3+} + e^- \rightleftharpoons Fe^{2+}$	$E_{rev(Fe^{3+}/Fe^{2+})} = E_{rev(Fe^{3+}/Fe^{2+})}^o - \frac{RT}{F} \ln \left(\frac{c_{Fe^{2+}}}{c_{Fe^{3+}}} \right)$
3.	$Fe^{2+} + 2H_2O \rightleftharpoons Fe(OH)_2 + 2H^+$	$pH_{Fe^{2+}/Fe(OH)_2} = -\log \left(K_{Fe^{2+}/Fe(OH)_2} c_{Fe^{2+}} \right)^{\frac{1}{2}}$
4.	$Fe(OH)_2 + 2H^+ + 2e^- \rightleftharpoons Fe + 2H_2O$	$E_{rev(Fe(OH)_2/Fe)} = E_{rev(Fe(OH)_2/Fe)}^o + \frac{RT}{2F} \ln(c_{H^+}^2)$
5.	$Fe_3O_4 + 2H_2O + 2H^+ + 2e^- \rightleftharpoons 3Fe(OH)_2$	$E_{rev(Fe_3O_4/Fe(OH)_2)} = E_{rev(Fe_3O_4/Fe(OH)_2)}^o + \frac{RT}{2F} \ln(c_{H^+}^2)$
6.	$6Fe_2O_3 + 4H^+ + 4e^- \rightleftharpoons 4Fe_3O_4 + 2H_2O$	$E_{rev(Fe_2O_3/Fe_3O_4)} = E_{rev(Fe_2O_3/Fe_3O_4)}^o + \frac{RT}{4F} \ln(c_{H^+}^4)$

Table 8 (continued)

No.	Reaction	Equilibrium Potential in V or pH
7.	$Fe_3O_4 + 8H^+ + 2e^- \rightleftharpoons 3Fe^{2+} + 4H_2O$	$E_{rev(Fe_3O_4/Fe^{2+})} = E_{rev(Fe_3O_4/Fe^{2+})}^o - \frac{RT}{2F} \ln \left(\frac{c_{Fe^{2+}}^3}{c_{H^+}^8} \right)$
8.	$2Fe_2O_3 + 12H^+ + 4e^- \rightleftharpoons 4Fe^{2+} + 6H_2O$	$E_{rev(Fe_2O_3/Fe^{2+})} = E_{rev(Fe_2O_3/Fe^{2+})}^o - \frac{RT}{4F} \ln \left(\frac{c_{Fe^{2+}}^4}{c_{H^+}^{12}} \right)$
9.	$Fe_3O_4 + 8H^+ + 8e^- \rightleftharpoons 3Fe + 4H_2O$	$E_{rev(Fe_3O_4/Fe)} = E_{rev(Fe_3O_4/Fe)}^o + \frac{RT}{8F} \ln(c_{H^+}^8)$
10.	$2Fe^{3+} + 3H_2O \rightleftharpoons Fe_2O_3 + 6H^+$	$pH_{(Fe^{3+}/Fe_2O_3)} = -\log \left(K_{(Fe^{3+}/Fe_2O_3)} c_{Fe^{3+}}^2 \right)^{\frac{1}{6}}$
11.	$Fe^{2+} + CO_{2(g)} + H_2O \rightleftharpoons FeCO_3 + 2H^+$	$pH_{(Fe^{2+}/FeCO_3)} = -\log \left(K_{(Fe^{2+}/FeCO_3)} c_{Fe^{2+}} p_{CO_2} \right)^{\frac{1}{2}}$
12.	$Fe_3O_4 + 3CO_{2(g)} + 2H^+ + 2e^- \rightleftharpoons 3FeCO_3 + H_2O$	$E_{rev(Fe_3O_4/FeCO_3)} = E_{rev(Fe_3O_4/FeCO_3)}^o + \frac{RT}{2F} \ln(c_{H^+}^2 p_{CO_2}^3)$
13.	$FeCO_3 + 2H^+ + 2e^- \rightleftharpoons Fe + CO_{2(g)} + H_2O$	$E_{rev(FeCO_3/Fe)} = E_{rev(FeCO_3/Fe)}^o - \frac{RT}{2F} \ln \left(\frac{p_{CO_2}}{c_{H^+}^2} \right)$
14.	$Fe_2O_3 + 2CO_{2(g)} + 2H^+ + 2e^- \rightleftharpoons 2FeCO_3 + H_2O$	$E_{rev(Fe_2O_3/FeCO_3)} = E_{rev(Fe_2O_3/FeCO_3)}^o + \frac{RT}{2F} \ln(c_{H^+}^2 p_{CO_2}^2)$

3.3 Experimental validation of generated Pourbaix diagrams

3.3.1 *Experimental procedures*

Experiments were conducted in a 1-liter SS316 autoclave, a closed system, under stagnant conditions. The electrolyte was an aqueous solution of 1 wt.% NaCl, saturated with CO₂ at 1 bar total pressure. API 5L X65 metal specimens (chemical composition listed in Table 9 and the dimensions shown in Figure 16) polished with 600-grit silicon carbide sand papers were used. For each test, 3 specimens were added to the fully purged solution in the autoclave, which was then sealed at 25°C. Conditions at the beginning of the experiment were: 1 bar of CO₂ at 25°C and pH 3.83. The water chemistry was calculated using the equilibrium constants as described in Chapter 2. The temperature in the autoclave was then increased to the desired value. At the end of each test, the temperature was lowered to 80°C and the samples were removed with special care. In order to remove salt from the surface and avoid oxidation, the samples were immediately rinsed with deoxygenated, deionized water followed by isopropanol, and then dried in a N₂ atmosphere. Sample surfaces were characterized by scanning electron microscopy (SEM), energy dispersive X-ray spectroscopy (EDX) and X-ray diffraction (XRD) techniques. Then, the corrosion product layer formed on the steel surface was removed by immersing the specimens into Clarke solution [97] to determine the weight loss and calculate the corrosion rate. In addition, the concentration of Fe²⁺ in the solution was measured after each experiment.

Table 9. Chemical composition of API 5L X65 (wt%).

C	Mn	Si	P	S	Cr	Cu	Ni	Mo	Al	Fe
0.050	1.32	0.31	0.013	0.002	0.042	0.019	0.039	0.031	0.032	Bal.

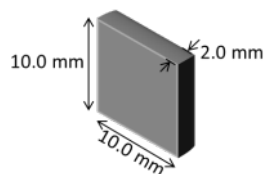


Figure 16. Weight-loss specimen.

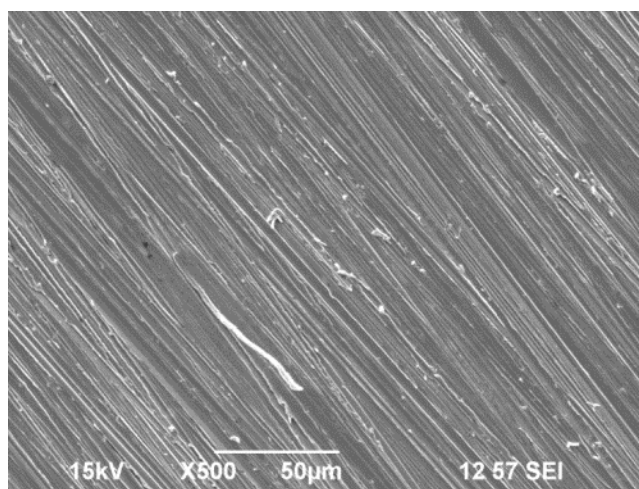


Figure 17. Specimen surface of X65 polished with 600-grit sand paper.

3.3.2 Results and discussion

3.3.2.1 Surface Characterization

i) Effect of temperature

The test condition is listed in Table 10. Scanning electron microscopy (SEM) and X-ray diffraction (XRD) results for the experimental conditions at 80, 100, 120, 150, 200, and 250°C are shown in Figure 18 - Figure 23, respectively. The additional EDX analyses of these specimens are shown in Appendix C. These figures directly correspond to the Pourbaix diagrams illustrated in Figure 12 b - Figure 12 g. The SEM results show a mixture of plate-like crystals (“plates”) and oblong prismatic-shaped crystals (“prisms”) on the steel surfaces at 80-150°C (Figure 18 a. - Figure 21 a.). No obvious crystal morphology was observed on the surfaces of samples exposed at 200°C and 250°C (Figure 22 a. - Figure 23 a.). XRD analysis indicated that FeCO_3 and $\text{Fe}_2(\text{OH})_2\text{CO}_3$ formed on the steel surface at 80-150°C (Figure 18 b. - Figure 21 b.). At 200-250°C, the corrosion product is exclusively Fe_3O_4 (Figure 22 b. - Figure 23 b.).

At a first glance, there seems to be a discrepancy between the experimental results and those suggested by the Pourbaix diagrams constructed for the same system, particularly at lower temperature. Using the typical open circuit potential for this Fe–CO₂–H₂O system (approximately -0.7 V vs. Ag/AgCl reference electrode or -0.5 V vs. H₂ electrode), and the calculated bulk pH, the operating point can be plotted in the Pourbaix diagrams for the purposes of comparison (solid circles on Figure 12 b. – Figure 12 g.). According to the Pourbaix diagrams, with the bulk solution at approximately pH 4, the dominant species in the range 80-150°C should be Fe^{2+} . However, the surface analysis

has indicated the presence of FeCO_3 and $\text{Fe}_2(\text{OH})_2\text{CO}_3$. At 250°C , the Pourbaix diagram suggests that Fe_3O_4 is the most stable iron containing phase and the surface analysis confirmed that.

Table 10. Test matrix for the experiments in Section 3.3.2.1 i).

Parameter	Description
System	1-Liter Autoclave
Material	API 5L X65
Temperature ($^\circ\text{C}$)	80, 100, 120, 150, 200, 250
pCO_2^*	1 bar at 25°C
Solution	1wt.% NaCl
Specimen surface finish (grit)	600 - uniform
Test duration (days)	4
Surface analysis	SEM and EDX, XRD

* See the water chemistry in Table 4, Set 2.

This apparent disagreement can be resolved by accounting for the higher pH at the corroding steel surface, compared to the bulk. Han, *et al.* [98], designed a new technique to measure the surface pH directly using the mesh-capped pH probe in CO_2 aqueous environments. Their results show that surface pH is significantly higher than bulk pH in stagnant solutions. For example, when the bulk solution was pH 4.0 at 80°C , the pH near a mild steel corroding surface could be as high as pH 6.2 in stagnant

solutions. The increase in pH near the surface is caused by the consumption of H^+ and release of Fe^{2+} from the steel due to corrosion. If the corrosion rate is high, the surface pH can be even higher than this measured value. If this elevated surface pH is used in the Pourbaix diagrams (as open circles), it can be seen that from 80-150°C, $FeCO_3$ will be the dominant phase, while Fe_3O_4 will be the most dominant compound from 200-250°C. Taking into account the surface pH, the experimental results agree well with those predicted with the Pourbaix diagrams, and the latter can be considered validated.

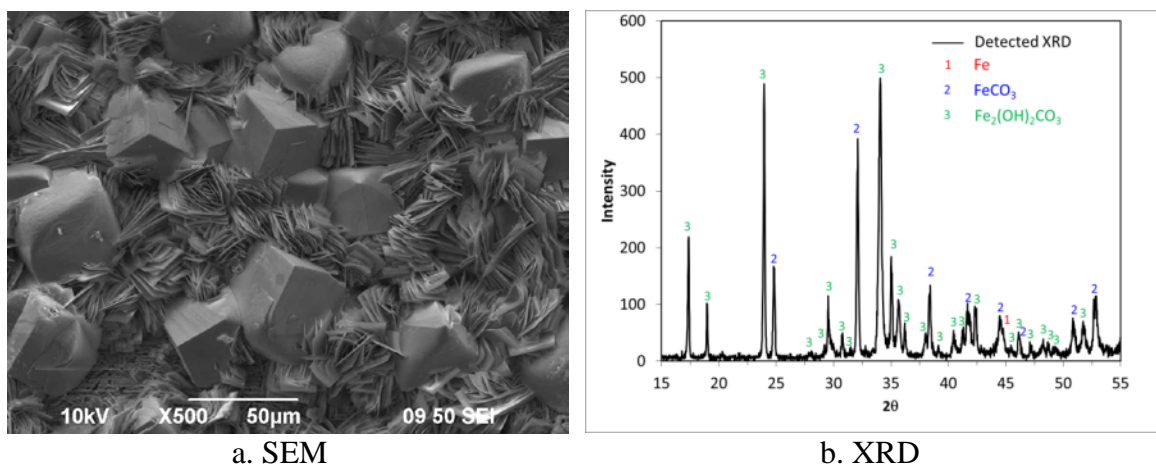
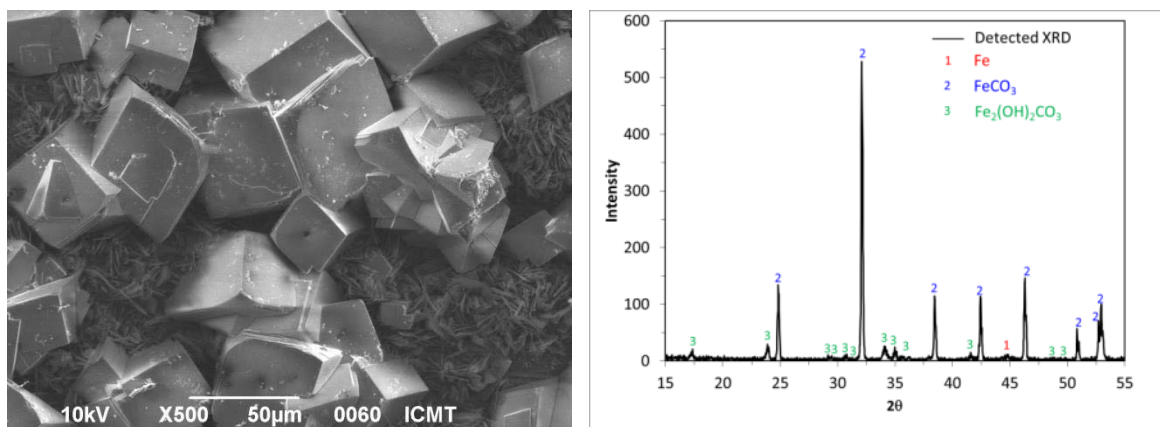


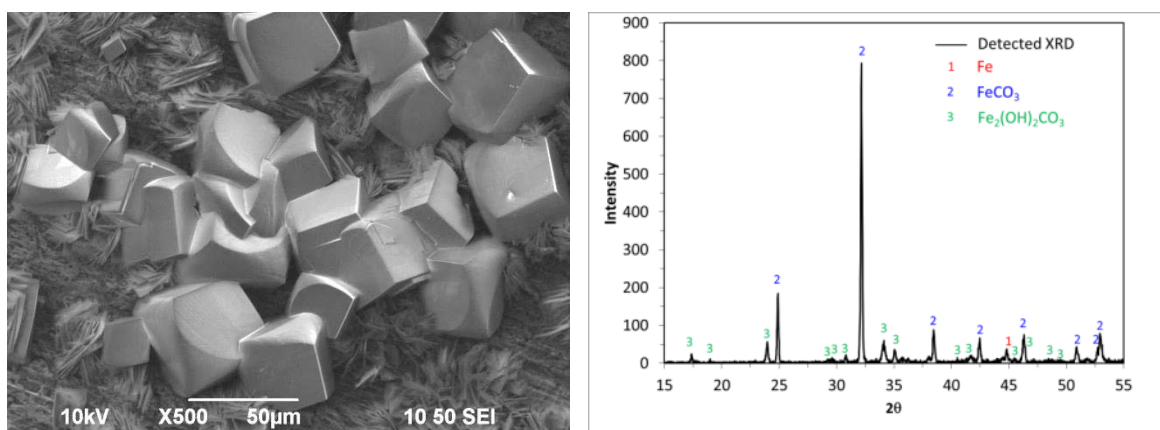
Figure 18. Morphology and compositional analysis of corrosion product layer at 80°C, 4 days, 1 wt.% NaCl, $pCO_2=1$ bar at 25°C.



a. SEM

b. XRD

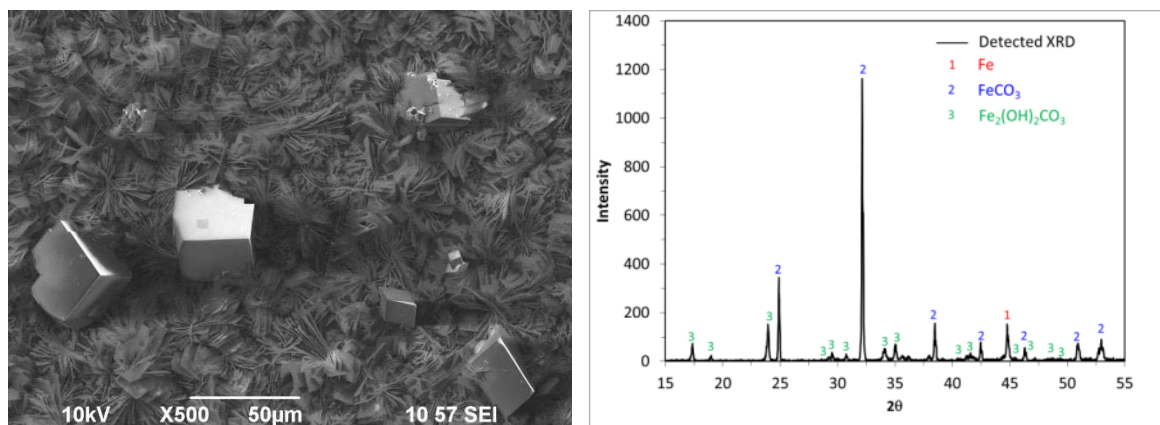
Figure 19. Morphology and compositional analysis of corrosion product layer at 100°C, 4 days, 1 wt.% NaCl, pCO₂=1 bar at 25°C.



a. SEM

b. XRD

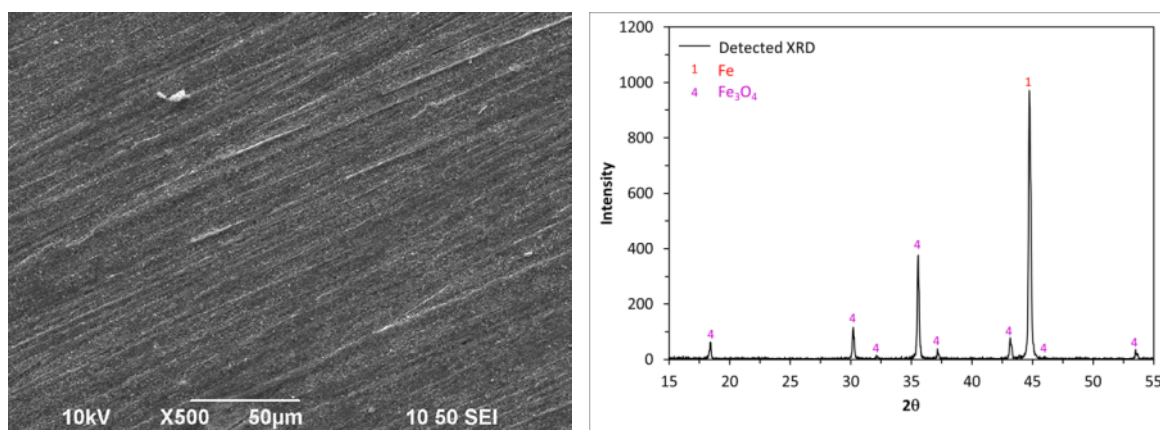
Figure 20. Morphology and compositional analysis of corrosion product layer at 120°C, 4 days, 1 wt.% NaCl, pCO₂=1 bar at 25°C.



a. SEM

b. XRD

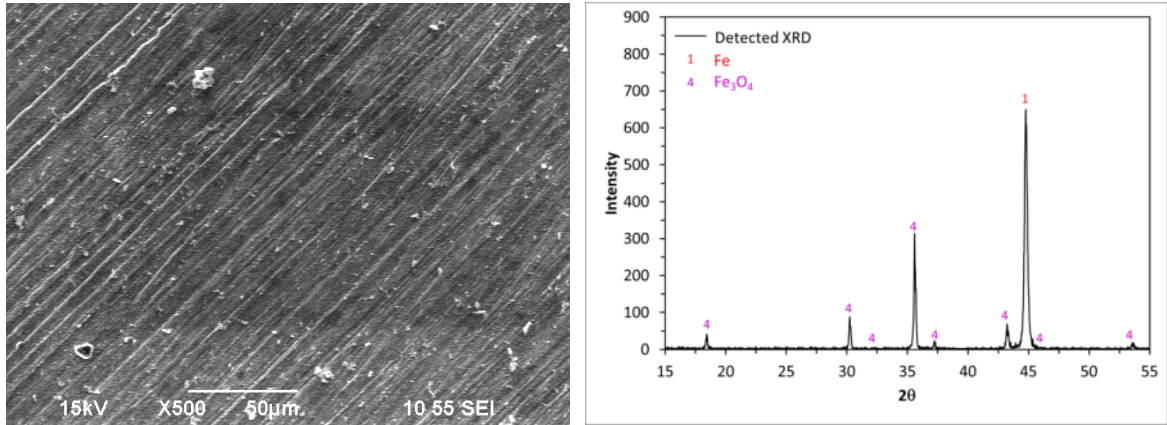
Figure 21. Morphology and compositional analysis of corrosion product layer at 150°C, 4 days, 1 wt.% NaCl, $p\text{CO}_2=1$ bar at 25°C.



a. SEM

b. XRD

Figure 22. Morphology and compositional analysis of corrosion product layer at 200°C, 4 days, 1 wt.% NaCl, $p\text{CO}_2=1$ bar at 25°C.

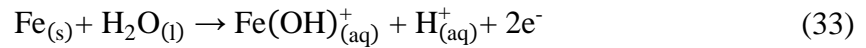


a. SEM

b. XRD

Figure 23. Morphology and compositional analysis of corrosion product layer at 250°C, 4 days, 1 wt.% NaCl, $p\text{CO}_2=1$ bar at 25°C.

To elaborate on the identified corrosion products, FeCO_3 and $\text{Fe}_2(\text{OH})_2\text{CO}_3$ were observed in all experiments below 200°C. However, $\text{Fe}_2(\text{OH})_2\text{CO}_3$ was not considered in the Pourbaix diagram construction as it is considered to be an intermediate, metastable species, leading to the formation of FeCO_3 *via* the following multistep mechanism [62], [65], [66], [99]:



Due to the limitation of the availability of the thermodynamic data of $\text{Fe}_2(\text{OH})_2\text{CO}_3$, the Gibbs free energy of formation of $\text{Fe}_2(\text{OH})_2\text{CO}_3$ is known only at 25°C (-1,175.1 kJ/mol) as given by Azoulay *et al.* [100]. The authors also suggested that $\text{Fe}_2(\text{OH})_2\text{CO}_3$ is metastable with respect to FeCO_3 . By inspecting the Gibbs free energy

of transformation of $\text{Fe}_2(\text{OH})_2\text{CO}_3$ to FeCO_3 Reaction (36), the Gibbs free energy of formation of FeCO_3 is more negative than that of $\text{Fe}_2(\text{OH})_2\text{CO}_3$. Therefore, $\text{Fe}_2(\text{OH})_2\text{CO}_3$ will be converted to FeCO_3 eventually.



$$\Delta G^\circ = -25.1 \text{ kJ/mol}$$

To confirm this scenario, variable duration experiments were conducted at 120°C , and are described in the following section.

ii) Evolution of the growth of corrosion product layers with time

Since $\text{Fe}_2(\text{OH})_2\text{CO}_3$ was observed as a dominant corrosion product in the experiments mentioned above at 120°C , a progression of tests lasting 1 – 30 days were performed to determine the chemical kinetics of the suggested transformation of $\text{Fe}_2(\text{OH})_2\text{CO}_3$ into FeCO_3 . The test condition is listed in Table 11. The SEM images and XRD analysis for 1, 2, 4, 10, and 30 day tests at 120°C confirm that the transformation of $\text{Fe}_2(\text{OH})_2\text{CO}_3$ into FeCO_3 is occurring.

Figure 24 a. shows the corrosion product layer on the steel surface after 1 day. The SEM image shows that the steel surface was partially covered by a mixture of thin plates and oblong prisms with an average size of approximately $15 \mu\text{m}$. From the XRD analysis, the detected XRD pattern (Figure 24 b.) suggest shows the presence of $\text{Fe}_2(\text{OH})_2\text{CO}_3$ with small amounts of FeCO_3 .

After 2 days (Figure 25) and 4 days (Figure 20) of exposure time, there were more crystals formed on the steel surface and the size of prisms was larger than those observed

after the 1-day test. The average size of the prisms was 28 and 39 μm , respectively.

Similarly, there were morphological mixtures of plates and prisms thoroughly covering the steel surfaces after 7 and 10 days of exposure, as illustrated in Figure 26 a. - Figure 27 a. The average size of the prisms was 50 μm . In contrast to the previous three experiments, only FeCO_3 was detected by XRD analysis (Figure 26 b. - Figure 27 b.).

After 30 days of exposure, the SEM image and XRD pattern (Figure 28) demonstrated only inter-grown prisms of FeCO_3 formed on the steel surface. Therefore, it is concluded that all the plate-shaped crystals were transformed to the prisms during the 30-day exposure. These experiments have confirmed that the plate-like $\text{Fe}_2(\text{OH})_2\text{CO}_3$ was a transition state phase in forming more stable FeCO_3 .

Table 11. Test matrix for the experiments in Section 3.3.2.1 ii).

Parameter	Description
System	1-Liter Autoclave
Material	API 5L X65
Temperature ($^{\circ}\text{C}$)	120, 200
pCO_2 (bars)*	1 bar at 25°C
Solution	1 wt.% NaCl
Specimen surface finish (grit)	600 - uniform
Test duration (days)	1 to 30
Surface analysis	SEM and EDX, XRD

* See the water chemistry in Table 4, Set 2.

Table 12 shows the quantitative analysis of XRD results on the steel surface. The percentage of $\text{Fe}_2(\text{OH})_2\text{CO}_3$ with respect to FeCO_3 covered on the surface decreased over time, which was consistent with the change of the morphology, i.e. changing from the plate-like shape to the prismatic-like one.

Referring back to the generated Pourbaix diagram (Figure 12 d.) and taking surface pH into consideration, it is concluded that the expected corrosion product at 120°C is FeCO_3 . Although FeCO_3 and $\text{Fe}_2(\text{OH})_2\text{CO}_3$ were both observed after the 4-day experiments, FeCO_3 was the only thermodynamically favored stable corrosion product after 10 and 30 days. Thus, the result from the Pourbaix diagram agrees with the experimental observations.

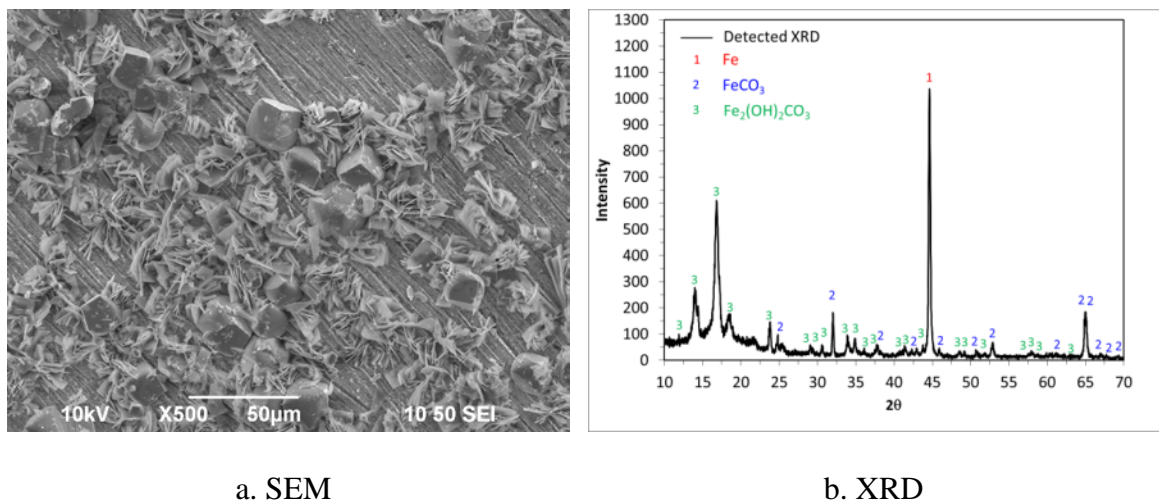
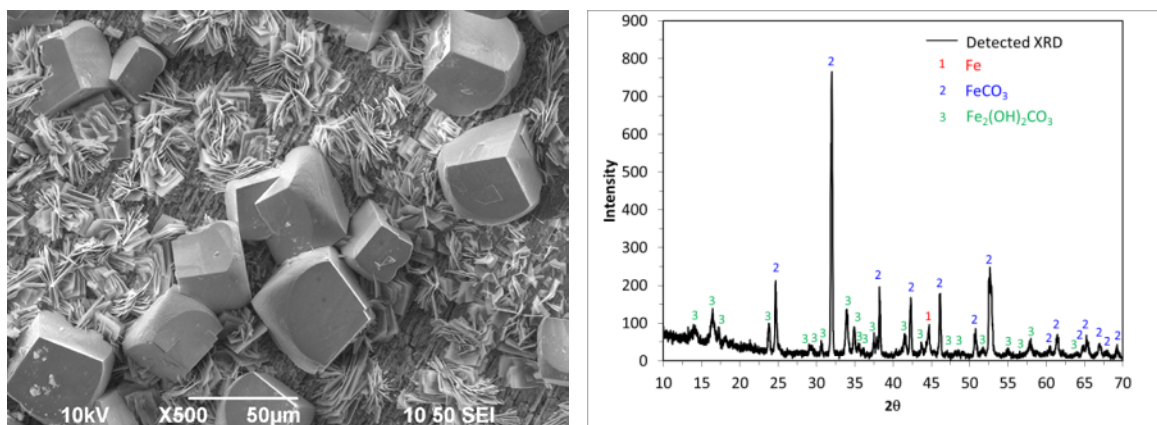


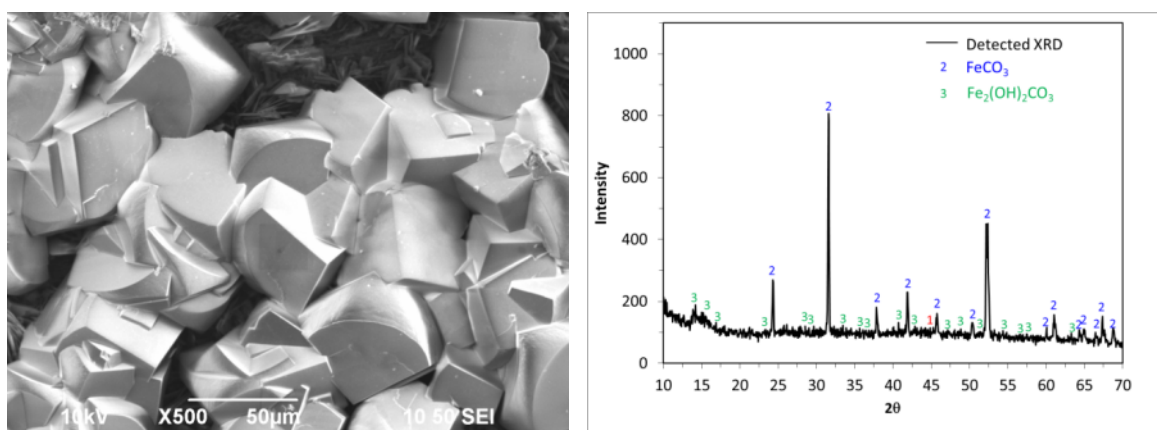
Figure 24. Morphology and compositional analysis of corrosion product layer at 120°C , 1 day, 1 wt.% NaCl, $p\text{CO}_2=1$ bar at 25°C .



a. SEM

b. XRD

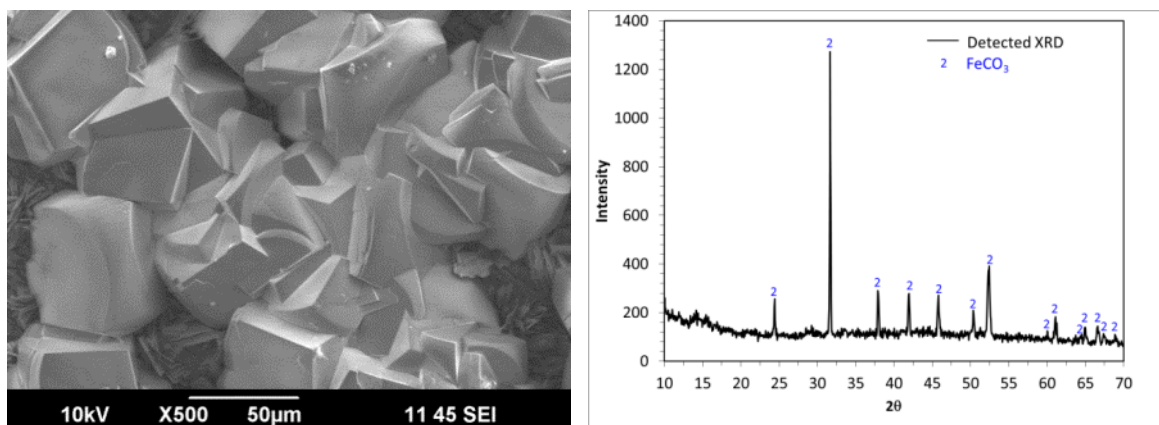
Figure 25. Morphology and compositional analysis of corrosion product layer at 120°C, 2 days, 1 wt.% NaCl, pCO₂=1 bar at 25°C.



a. SEM

b. XRD

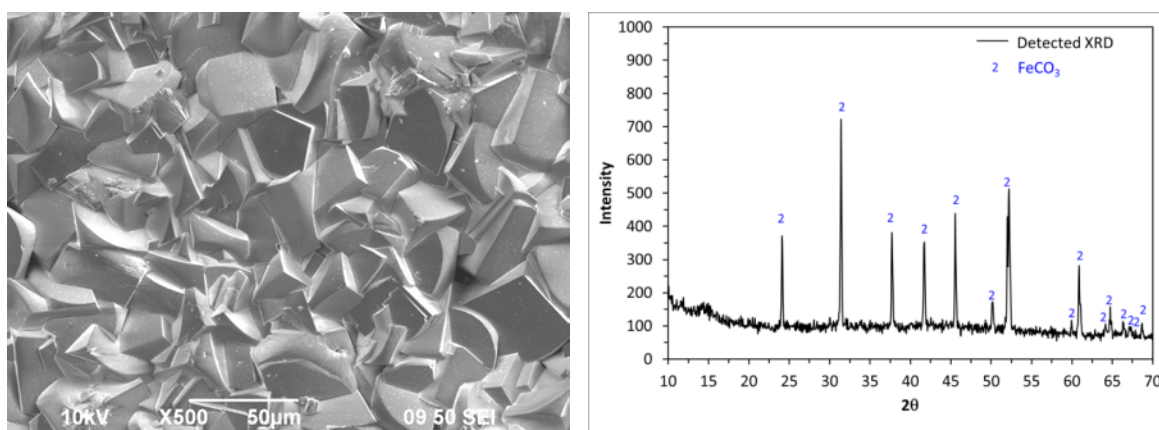
Figure 26. Morphology and compositional analysis of corrosion product layer at 120°C, 7 days, 1 wt.% NaCl, pCO₂=1 bar at 25°C.



a. SEM

b. XRD

Figure 27. Morphology and compositional analysis of corrosion product layer at 120°C, 10 days, 1 wt.% NaCl, pCO₂=1 bar at 25°C.



a. SEM

b. XRD

Figure 28. Morphology and compositional analysis of corrosion product layer at 120°C, 30 days, 1 wt.% NaCl, pCO₂=1 bar at 25°C.

Table 12. XRD quantitative analysis for the experiments at 120°C (Data from Figure 20b., Figure 24b. - Figure 28b.)

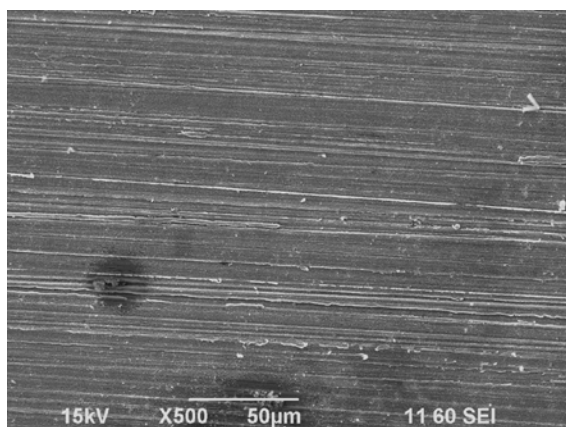
Test duration (days)	% Fe ₂ (OH) ₂ CO ₃ on the surface*
1	73
2	16
4	12
7	7
10	<7**
30	<7**

* The percentage of Fe₂(OH)₂CO₃ intensity was calculated from area under intensity curve from the detected XRD peaks.

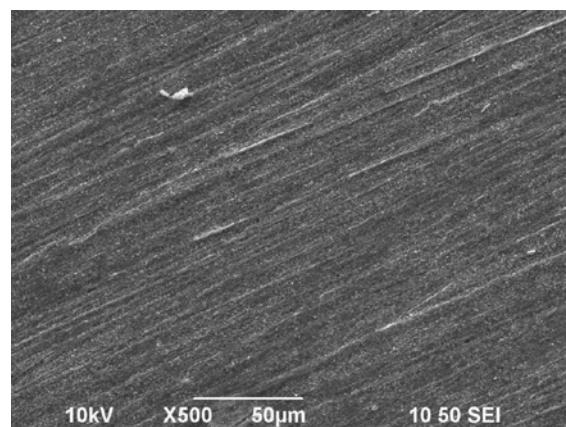
** The Fe₂(OH)₂CO₃ peaks were unable to distinguished from the diffractometer noise.

In addition, the surface topography of corrosion products at 200°C was observed with different test durations; 1, 4, 10 and 30 days as shown in Figure 29 a. – d., respectively. The corrosion product was exclusively Fe₃O₄ for all exposure times tested as they were analyzed by XRD (Figure 30 a. - c.).

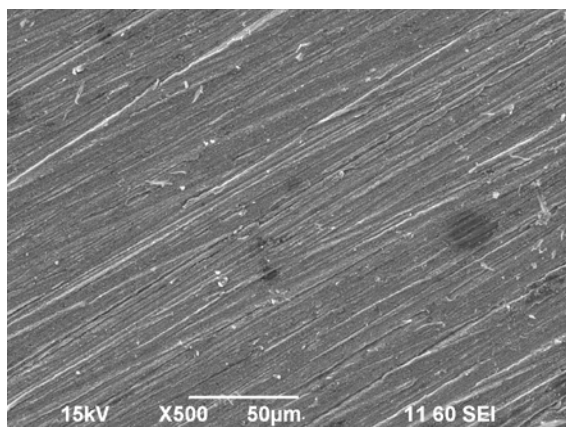
Correlating the generated Pourbaix diagram at 200°C (Figure 12 f.) to the surface characterized experiments, the expected corrosion phase is Fe₃O₄ and it was the only corrosion product detected in the experiments. Therefore, these results agree with the generated Pourbaix diagram.



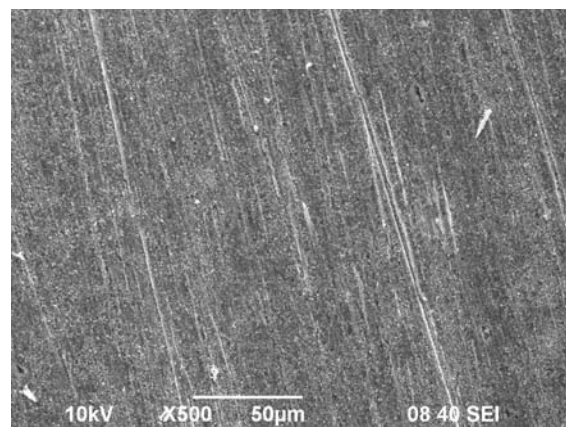
a. 1 day



b. 4 days

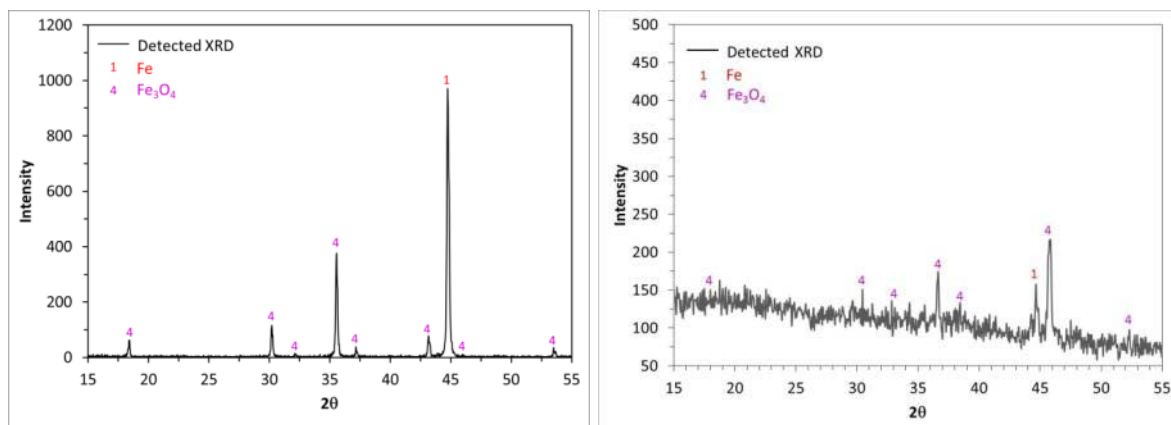


c. 10 day



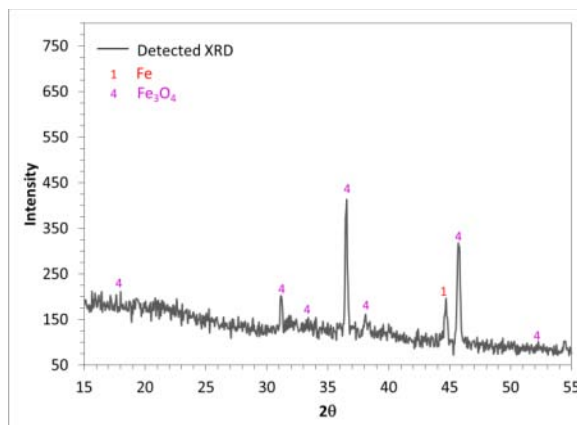
d. 30 days

Figure 29. SEM images of corrosion product layers at 200°C, 1 wt.% NaCl, $p\text{CO}_2=1$ bar at 25°C (test conditions listed in Table 11).



a. 4 day

b. 10 days



c. 30 days

Figure 30. XRD analysis of corrosion product layers at 200°C, 1 wt.% NaCl, $p\text{CO}_2=1$ bar at 25°C (test conditions listed in Table 11).

iii) Effect of partial pressure of CO₂

The effects of $p\text{CO}_2$ were further studied with four different $p\text{CO}_2$ experiments at 200°C: 0.8 bar, 2.7 bar (equivalent to 1 bar of CO₂ at 25°C), 3.8 bar (equivalent to 0.030 M of dissolved CO₂, used in Chapter 4) and 25 bars of $p\text{CO}_2$. Figure 31 a. - Figure 34 a. shows SEM images from the tests at 0.8, 2.7, 3.8 and 25 bars of $p\text{CO}_2$, respectively. At

0.8 and 2.7 bars of $p\text{CO}_2$, no obvious crystals were formed on the steel surface, but it was covered by Fe_3O_4 as confirmed by XRD results (Figure 31 b. and Figure 32 b., respectively). However, crystals were found on the surface at 3.8 and 25 bars. XRD analysis (Figure 33 b. - Figure 34 b.) indicated that a mixture of FeCO_3 and Fe_3O_4 was the corrosion products. By analyzing the XRD intensity results quantitatively, the ratio of Fe_3O_4 to FeCO_3 decreased as an increase in $p\text{CO}_2$, which was approximately 3% and $<<1\%$ for the tests at 3.8 bars and 25 bars, respectively.

Table 13. Test matrix for the experiments in Section 3.3.2.1 iii).

Parameter	Description
System	1-Liter Autoclave
Material	API 5L X65
Temperature ($^{\circ}\text{C}$)	200
$p\text{CO}_2$ (bars)*	0.8, 2.7, 3.8, 25
Solution	1 wt.% NaCl
Specimen surface finish (grit)	600 - uniform
Test duration (days)	4
Surface analysis	SEM and EDX, XRD

* See the water chemistry in Table 14.

Table 14. Water chemistry at 200°C for the conditions used in Section 3.3.2.1 iii).

pCO ₂ (bar)	Conc. Of CO _{2,aq} (Molar)	Natural pH
0.8	0.006	4.56
2.7*	0.022	4.30
3.8	0.030	4.22
25.0	0.197	3.81

*It is 1 bar at 25°C.

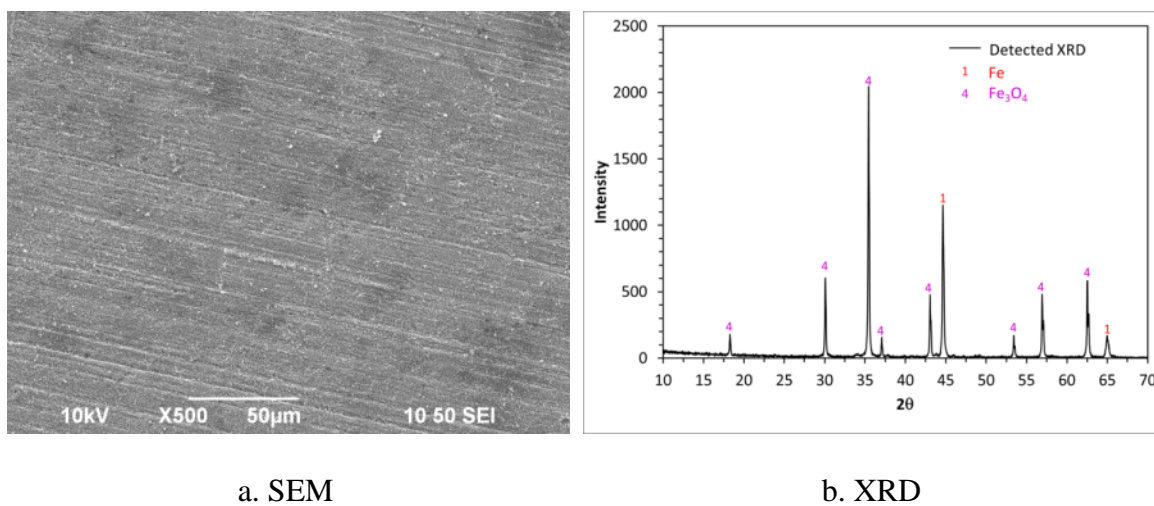
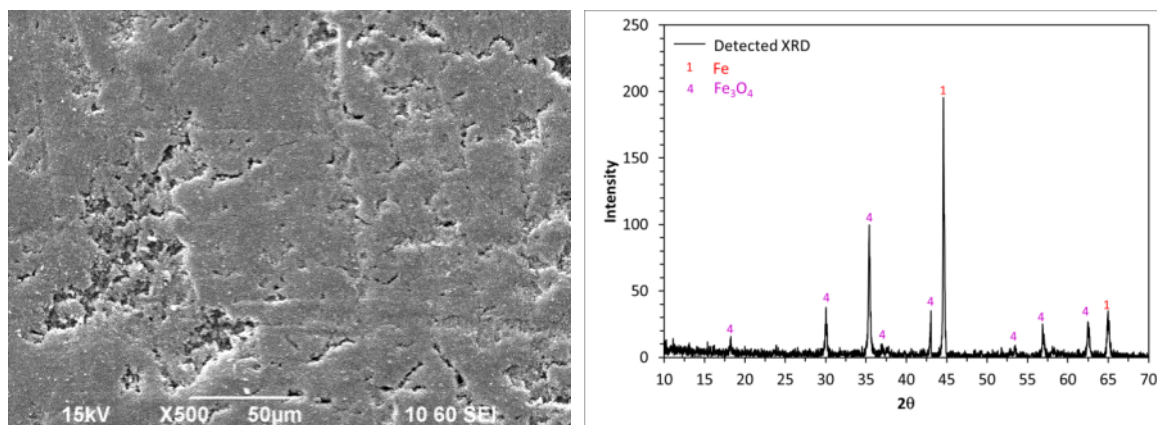


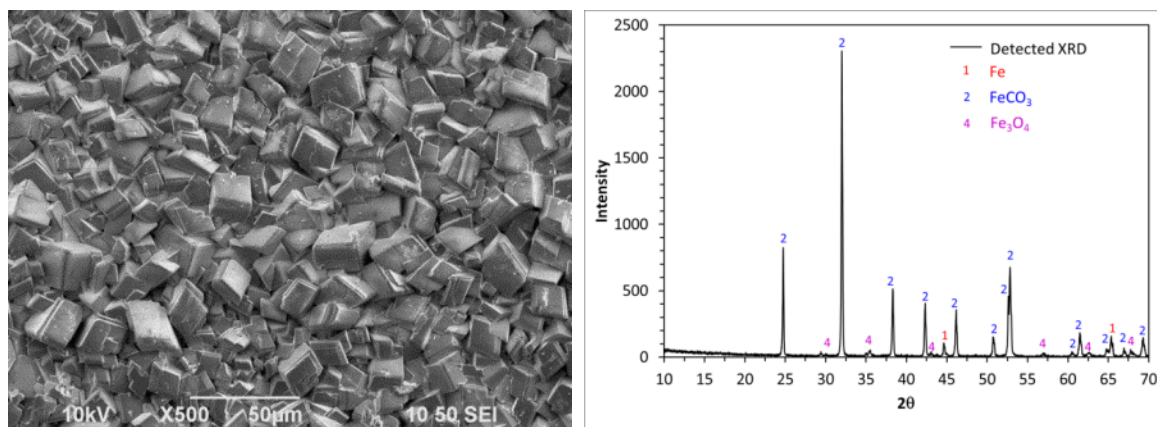
Figure 31. Surface analysis at 200°C, pCO₂=0.8bars, 4 days , 1 wt.% NaCl, pCO₂=1 bar at 25°C (test conditions listed in Table 13).



a. SEM

b. XRD

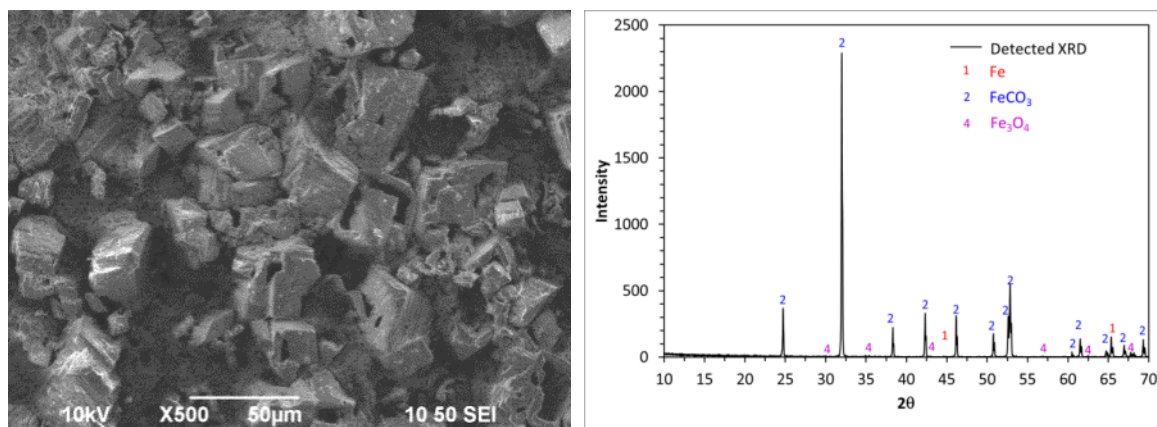
Figure 32. Morphology and compositional analysis of corrosion product layer at 200°C, $p\text{CO}_2=2.7$ bars (equivalent to 1 bar @ 25°C), 1 wt.% NaCl, 4 days (test conditions listed in Table 13).



a) SEM

b) XRD

Figure 33. Morphology and compositional analysis of corrosion product layer at 200°C, $p\text{CO}_2=3.8$ bars, 1 wt.% NaCl, 4 days (test conditions listed in Table 13).



a) SEM

b) XRD

Figure 34. Morphology and compositional analysis of corrosion product layer at 200°C, $p\text{CO}_2=25$ bars, 1 wt.% NaCl, 4 days (test conditions listed in Table 13).

The Pourbaix diagram at 200°C with respect to $p\text{CO}_2$ was constructed as shown in Figure 35. The FeCO_3 region is larger at higher $p\text{CO}_2$. When using the bulk pH, the main corrosion product is Fe^{2+} for each condition. With the consideration of the surface pH, Fe_3O_4 is predicted to be (and was detected as) the dominant species for all the tests. However, FeCO_3 was also a corrosion product detected in the tests at 3.8 bar and 25 bars of $p\text{CO}_2$. Since a Pourbaix diagram predicts only the most thermodynamically stable compound, the experimental results can be considered to be in good agreement with the generated Pourbaix diagrams.

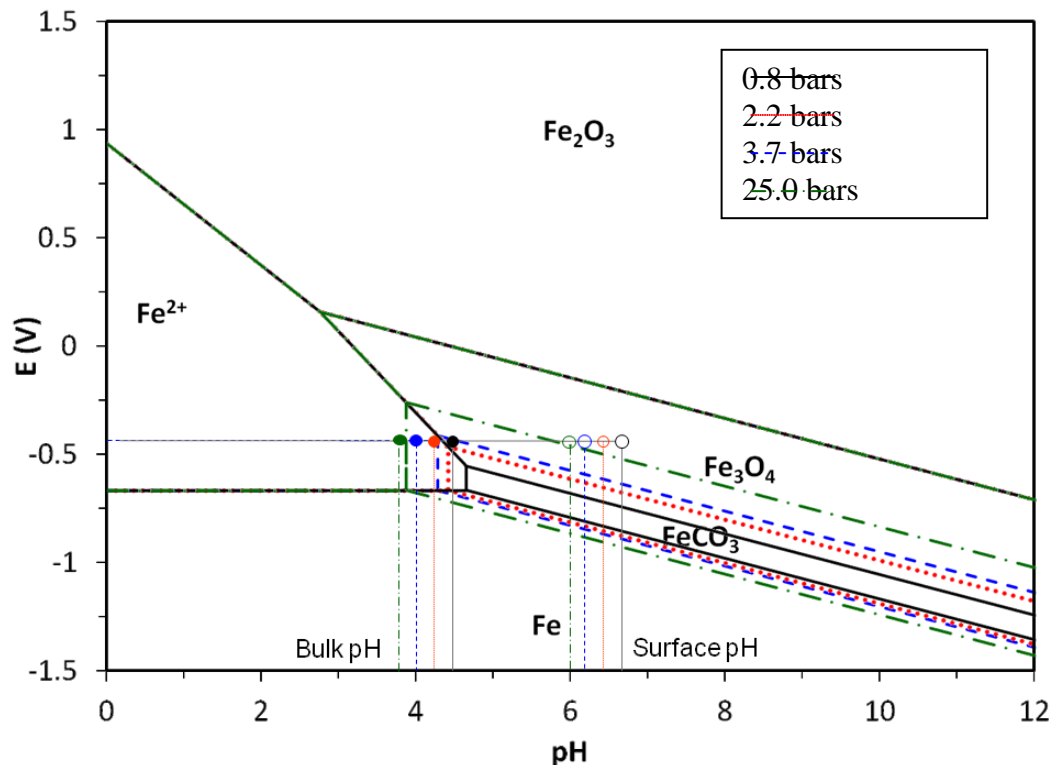


Figure 35. Generated Pourbaix diagrams at 200°C, $c_{\text{Fe}^{2+}}=10$ ppm; corresponding to the experimental conditions as listed in Table 14.

3.3.2.2 Corrosion rates

The uniform corrosion rates determined by weight loss for 4-day experiments are shown in Figure 36. In experimentation from 80°C to 100°C, the corrosion rates increased with temperature. The maximum corrosion rates were observed at around 100-120°C. The corrosion rates decreased at temperatures above 120°C due to the formation of a protective layer. The higher the temperature, the higher the corrosion rate should be due to the accelerating kinetics of electrochemical and chemical reactions. However, the kinetics of FeCO_3 precipitation also increases with temperature [44]. Consequently, the

corrosion rate is lowered because FeCO_3 forms on the steel surface and acts as a barrier [26], [81]. In addition, according to XRD analysis, the corrosion product was Fe_3O_4 for temperatures above 200°C . The morphology of the Fe_3O_4 layer (Figure 42) is denser and thinner but more protective, leading to a decrease in corrosion rate. Ikeda, *et al.* [24] and de Waard and Lotz [54] saw a similar corrosion behavior as the maximum corrosion rate was achieved between 90°C and 120°C .

Figure 38 shows the average weight loss corrosion rates at 120°C over time. In experimentation at 120°C , the corrosion rates decreased with time due to the fact that the protective layer formed more extensively on the steel surface.

The weight loss corrosion rates at 120 and 200°C are shown in Figure 38 and Figure 39, respectively. In experimentation at 120°C and 200°C , the corrosion rates decreased with time due to the fact that the protective layer formed more extensively on the steel surface.

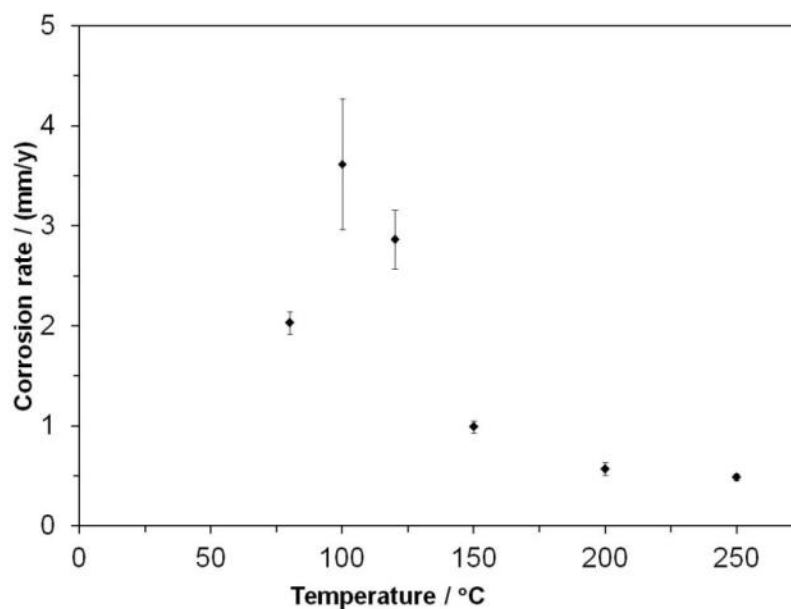


Figure 36. Weight loss corrosion rates vs temperature; $p\text{CO}_2=1$ bar at 25°C, 1 wt.%

NaCl, 4-day exposure (test conditions listed in Table 10).

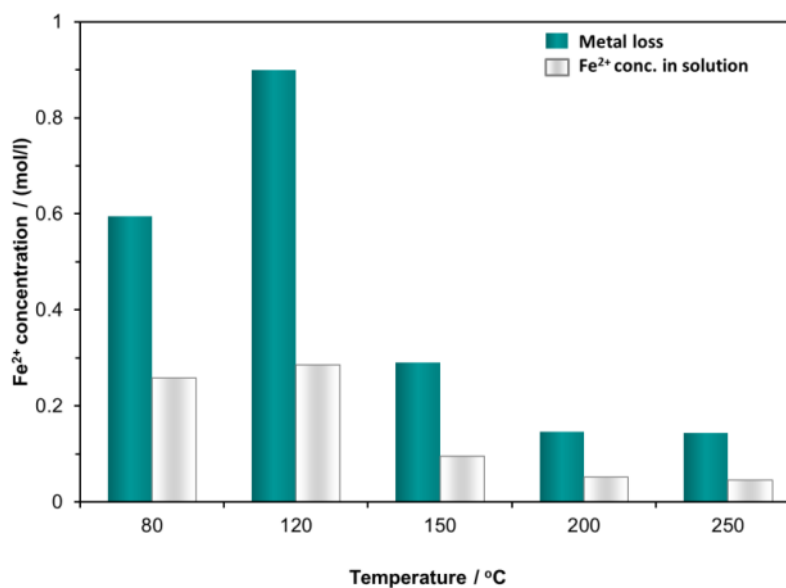


Figure 37. Metal loss and Fe^{2+} concentration in mol/l vs temperature; 1 $p\text{CO}_2=1$ bar at

25°C, 1 wt.% NaCl, 4-day exposure.

Figure 40 and Figure 41 show the rough comparisons of the weight loss corrosion rates to the scale weight and the measured Fe^{2+} concentration in solution after tests at 120°C and 200°C , respectively. The total weight loss slightly increased with time independent of temperature. Theoretically, the corrosion product layer weight and total mass of Fe^{2+} concentration should account for the total weight loss of specimens. Nevertheless, the results show that the amount of the corrosion product layer weight and Fe^{2+} concentration was less than the total weight loss. It can be explained by two possible reasons. First, the Fe^{2+} concentration was measured after the test when the system was cooled down, so the Fe^{2+} concentration may have changed during that time. Second, the corrosion product may have precipitated on the autoclave vessel instead of on the specimens.

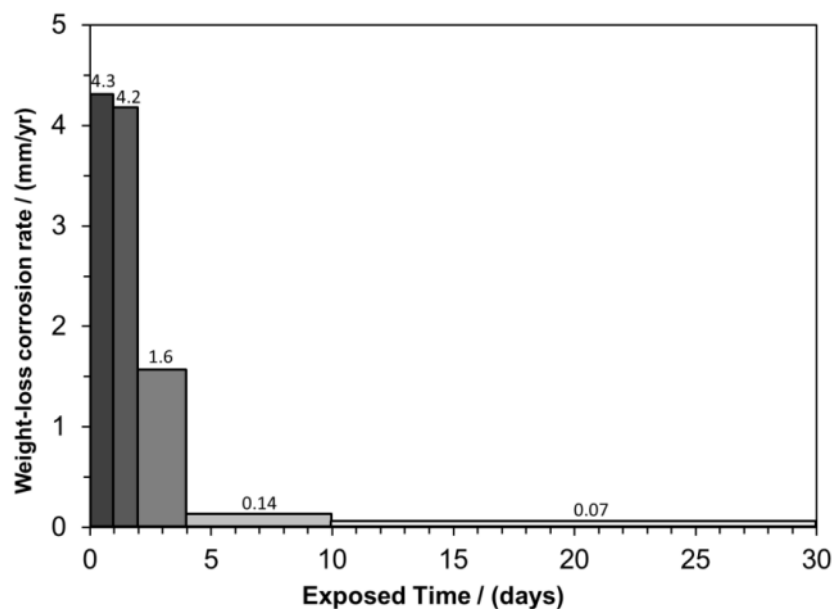


Figure 38. Average weight loss corrosion rate over time at 120°C ; $\text{pCO}_2=1$ bar at 25°C , 1 wt.% NaCl.

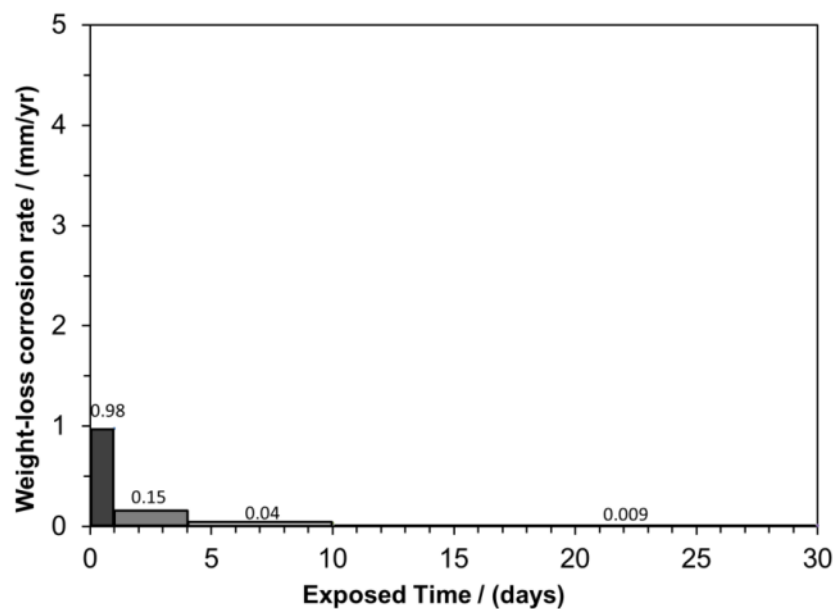


Figure 39. Average weight loss corrosion rate over time at 200°C; $p\text{CO}_2=1$ bar at 25°C, 1 wt.% NaCl.

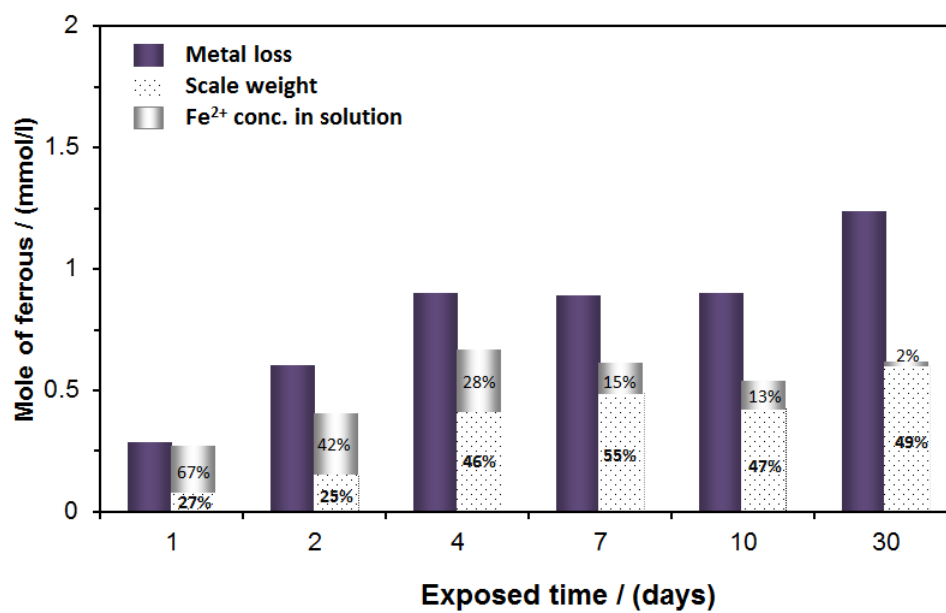


Figure 40. Moles of iron from X65 samples in autoclave testing at 120°C; $p\text{CO}_2=1$ bar at 25°C, 1 wt.% NaCl.

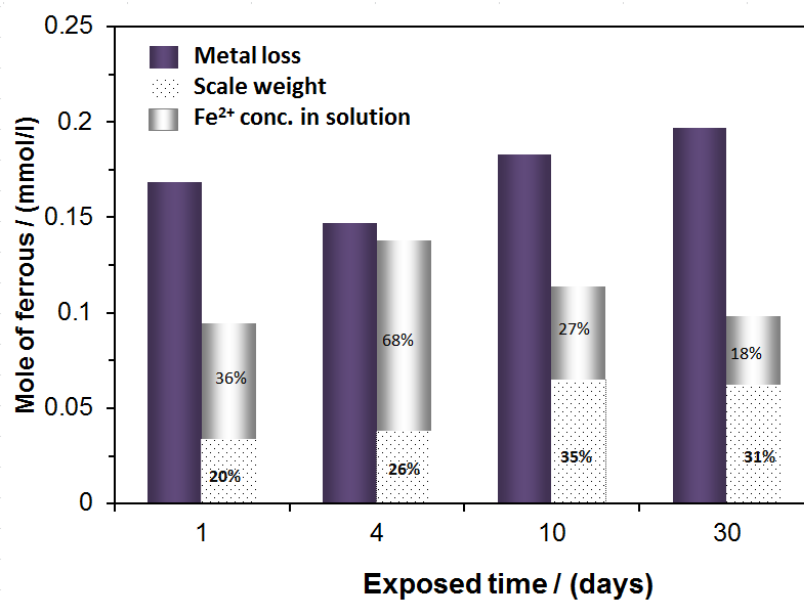


Figure 41. Moles of iron from X65 samples in autoclave testing at 200°C; pCO₂=1 bar at 25°C, 1 wt.% NaCl.

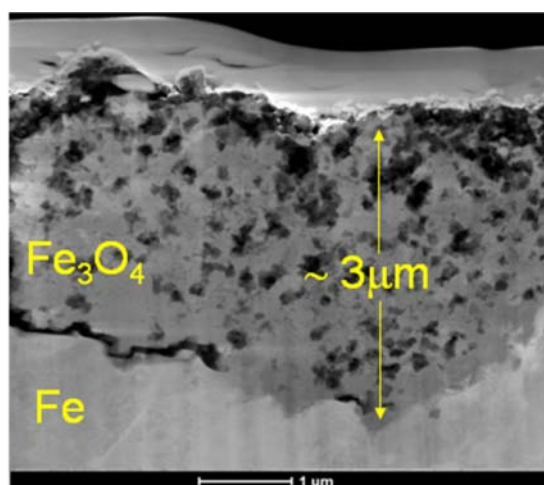
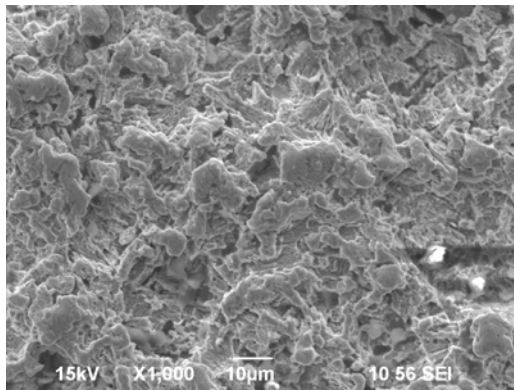
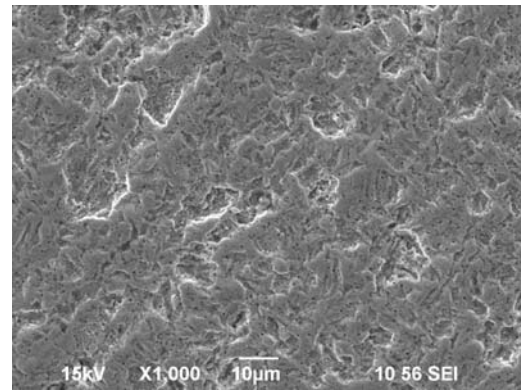


Figure 42. TEM analysis: Cross section of steel surface at 200°C; pCO₂=1 bar at 25°C, 1 wt.% NaCl, 4-day exposure; corresponding to Figure 22.

The specimens from the experiments at 120°C and 200°C from the 4-day experiments in Section 3.3.2.1 i) were selected for further analysis, since they had the highest and the lowest corrosion rates, respectively. After removing the corrosion product layer on the sample surfaces at 120°C and 200°C, SEM images (Figure 43) show the surface of steel at 120°C was rougher than that at 200°C. For 3D profilometry analysis (Figure 44), the maximum thickness losses of the sample at 120°C and 200°C were 47.7 μm and 8.7 μm , respectively. As a consequence, the maximum corrosion rates at 120°C and 200°C were 4.3 and 0.8 mm/year. Comparing those to their general corrosion rates (3.1 and 0.5 mm/year, respectively), they appeared to be reasonably close to the uniform corrosion rate.



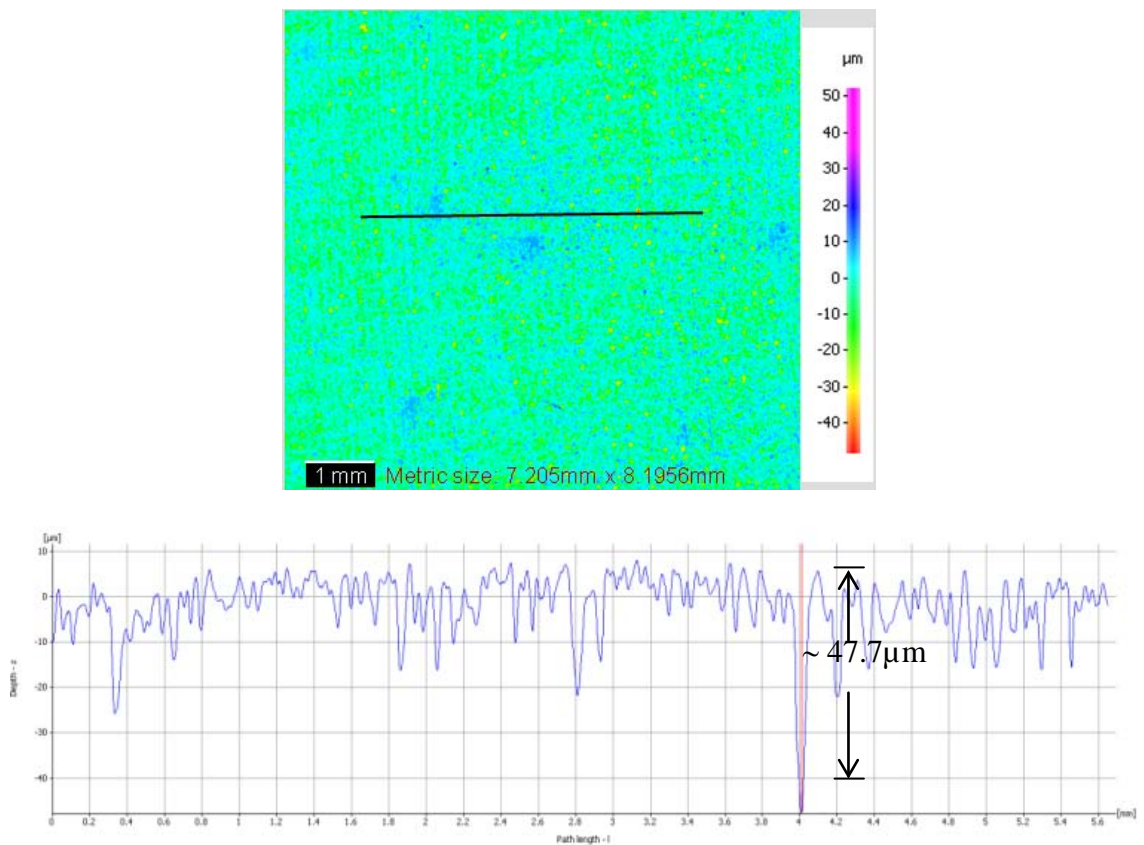
a. 120°C



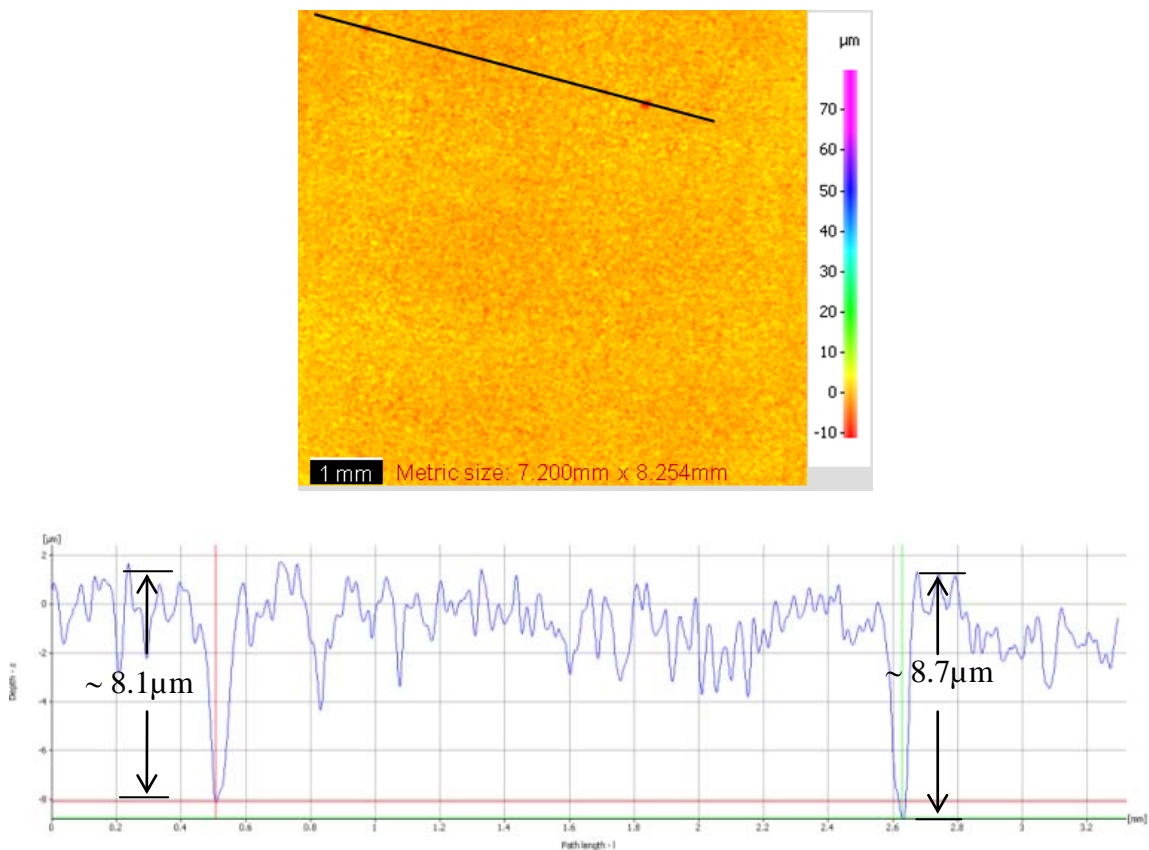
b. 200°C

Figure 43. SEM images of steel surfaces after cleaning from Figure 20 and Figure 22, respectively, for the 4-day experiments.

For the 30-day exposure, the maximum depths at 120°C and 200°C were ~ 87 and ~16 μm as shown in Figure 45 and Figure 46, which were 1.0 and 0.2 mm/year, respectively whereas the general corrosion rate after 30 days was 0.6 and 0.09 mm/year, respectively. In these both cases, it is not considered to be pitting corrosion because the ratio of the maximum to general corrosion rates was less than 3.

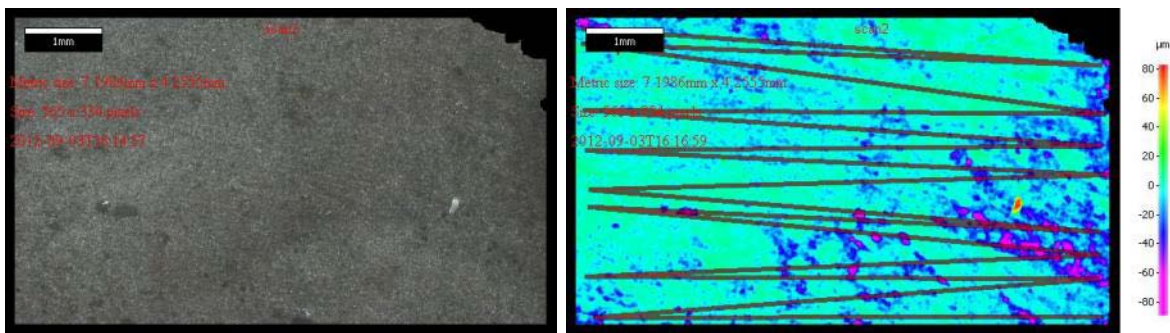


a. 120°C



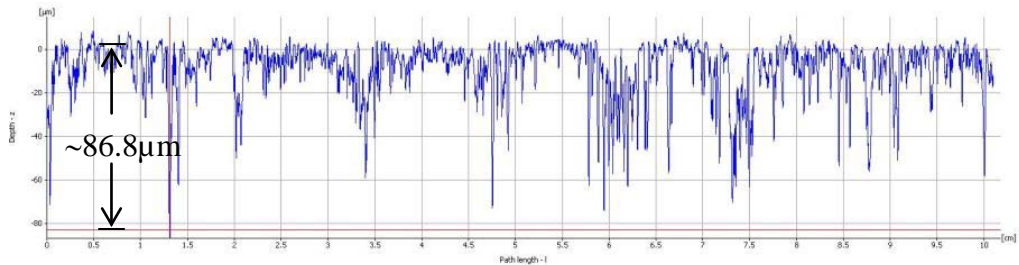
b. 200°C

Figure 44. 3D profilometry analysis of steel surfaces after cleaning from Figure 43 a. and b., respectively.

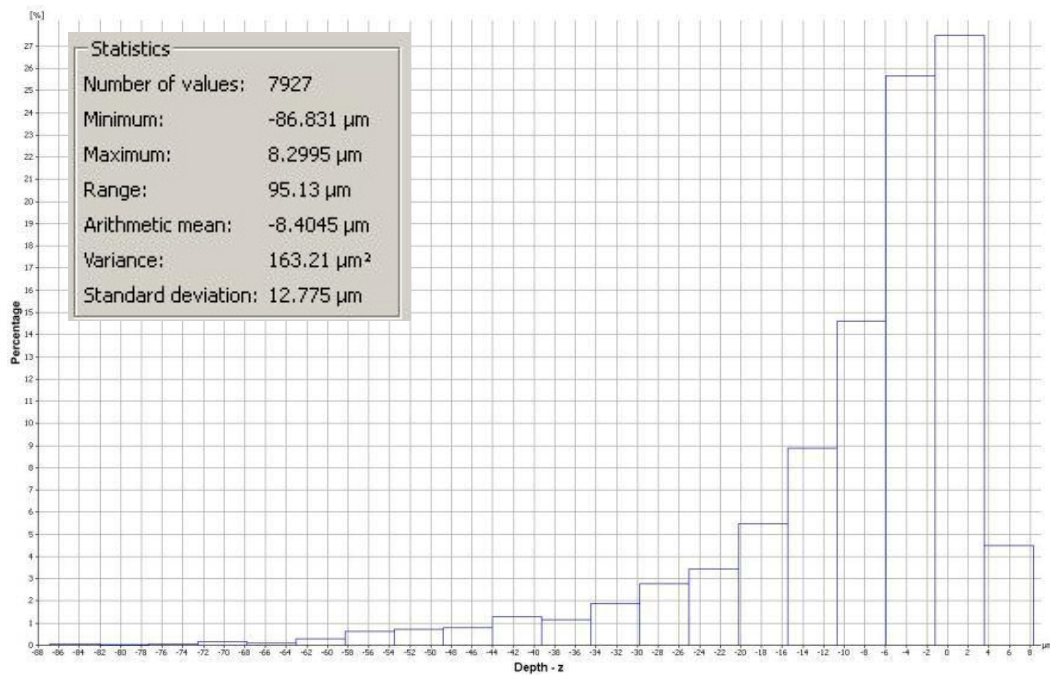


a. IFM image

b. IFM color image

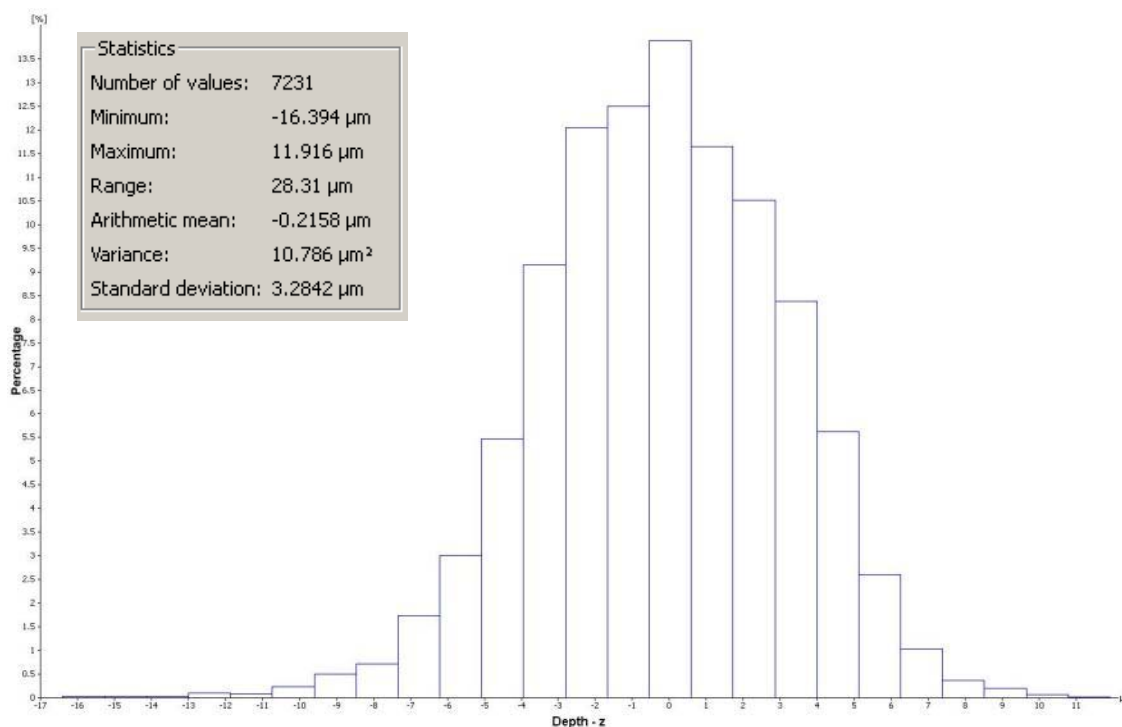


c. Depth profile



d. Depth/area distribution

Figure 45. 3D Profilometry at 120°C, 30 days after cleaning the surface from Figure 28.



d. Depth/area distribution

Figure 46. 3D Profilometry at 200°C, 30 days after cleaning the surface from Figure 29 d.

Figure 47 shows the weight loss corrosion rates at 200°C at $p\text{CO}_2$ of 0.8, 2.7, 3.8 and 25 bars (in Section 3.3.2.1 iii). The corrosion rate increased with $p\text{CO}_2$. The corrosion rate at 25 bars of $p\text{CO}_2$ was the highest, 2.2 mm/yr. However, the corrosion rate at 200°C and 25 bars of $p\text{CO}_2$ was compared to that at 80°C and 20 bars of $p\text{CO}_2$ (~20 mm/year) [101]. The steel surface at 200°C had more protection by the corrosion product layer. A mixture of FeCO_3 and Fe_3O_4 at 200°C was found while the condition at 80°C had only FeCO_3 on the steel surface. It is possible that Fe_3O_4 helps "passivate" the surface underneath the FeCO_3 layer [64], [102].

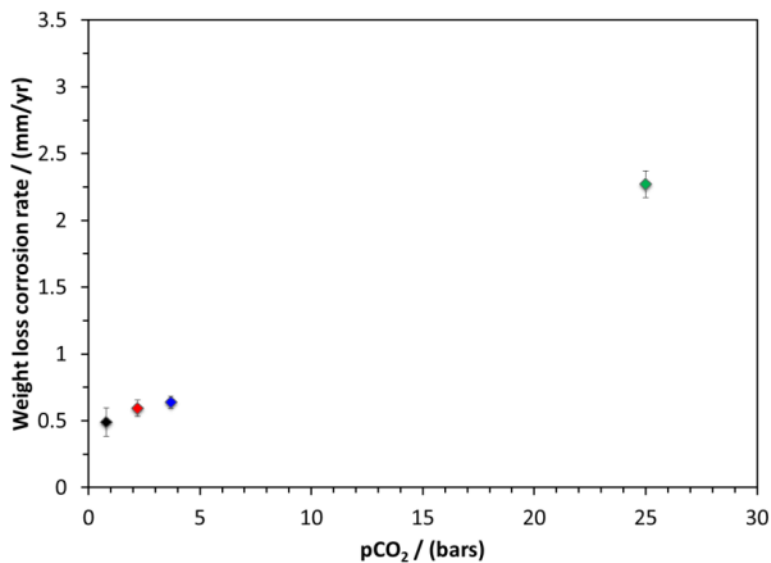


Figure 47. Weight loss corrosion rate vs pCO₂ at 200°C, 1 wt.% NaCl, 4 days (test conditions listed in Table 13).

3.4 Summary

In a CO₂ system, the typical range of pH is 3-7. By inspecting the generated Pourbaix diagrams, the stable states of iron in this range are Fe²⁺, FeCO₃ and Fe₃O₄. For the effect of temperature, XRD analysis indicates that FeCO₃ and Fe₂(OH)₂CO₃ formed on the steel surface at 80-150°C. At 200-250°C, the corrosion product is exclusively Fe₃O₄. The evolution of the growth of corrosion product layers at 120°C with time was also observed. The results show that the Fe₂(OH)₂CO₃ was an intermediate phase, or transition state, leading to FeCO₃ formation. In relation to pressure effects, the presence of FeCO₃ and Fe₃O₄ at 200°C depends on the partial pressure of CO₂. At a pCO₂ of higher than 3.7 bars, FeCO₃ is the more favored corrosion product. The generated

Pourbaix diagrams were validated with the experimental result with the surface pH consideration.

Chapter 4: Electrochemical Kinetics of Fe-CO₂-H₂O Systems at Elevated Temperatures

4.1 Introduction

Results reported in the Chapter 3 showed that in electrochemical thermodynamics the CO₂ corrosion at elevated temperatures is strongly affected by the formation of corrosion products. To have a better understanding of mechanisms of CO₂ corrosion of mild steel over a range of 80-200°C, the electrochemical kinetics has been studied *in situ* by using electrochemical measurements. This also included the effect of pH and flow. In addition, long-term experiments were performed in order to observe if there are any changes of the corrosion mechanisms or if there is initiation of localized corrosion.

4.2 Experimental procedure

Experiments were carried out in a 4-liter autoclave equipped to perform *in situ* electrochemical measurements as shown in Figure 48 and Figure 49. Two types of working electrodes were used; stationary working electrode and rotating cylindrical working electrode (RCE) as shown in Figure 49 a. and b., respectively. The electrolyte was 1 wt.% NaCl saturated with CO₂. To study the effect of temperature on CO₂ corrosion, the dissolved CO₂ concentration needs to be controlled to eliminate the temperature effect on the CO₂ solubility. In addition, the dissolved CO₂ corresponds to the total amount of carbonic acid in the system, so it is the best controlling parameter to adjust. Thus, the concentration of dissolved CO₂ was fixed at 0.030M for each experiment. For this condition, the partial pressure of CO₂ is as listed in Table 15. An

autoclave system was used to contain the system at different temperatures and pressures. The speciation was calculated using the equilibrium constants for a CO₂-H₂O system based on the approach presented in Chapter 2. Corrosion tests were conducted at temperatures of 80, 120, 150 and 200°C, pH values of 4.0 and 6.0 were used. A high temperature/pressure ZrO₂-based pH probe was used for monitoring pH.

Three types of API 5L X65 samples were employed:

- 1) Cylindrical specimens (Figure 50 a.) for electrochemical experiments in stagnant conditions.
- 2) RCE specimens (Figure 50 b.) for electrochemical experiments in flowing conditions.
- 3) Flat square specimens (Figure 50 c.) for XRD analysis.

A Gamry Reference 600™ potentiostat, with DC105 and EIS300 V5.30 software packages, was used for linear polarization resistance (LPR) and electrochemical impedance spectroscopy (EIS) measurements. The frequency range of EIS was 0.01 – 100,000 Hz. Corrosion rates from LPR were calculated using $B = 26$ mV/decade [103]. After 20 hour tests, the specimens were analyzed by scanning electron microscopy (SEM), energy-dispersive X-ray spectroscopy (EDX) and X-ray diffraction (XRD).

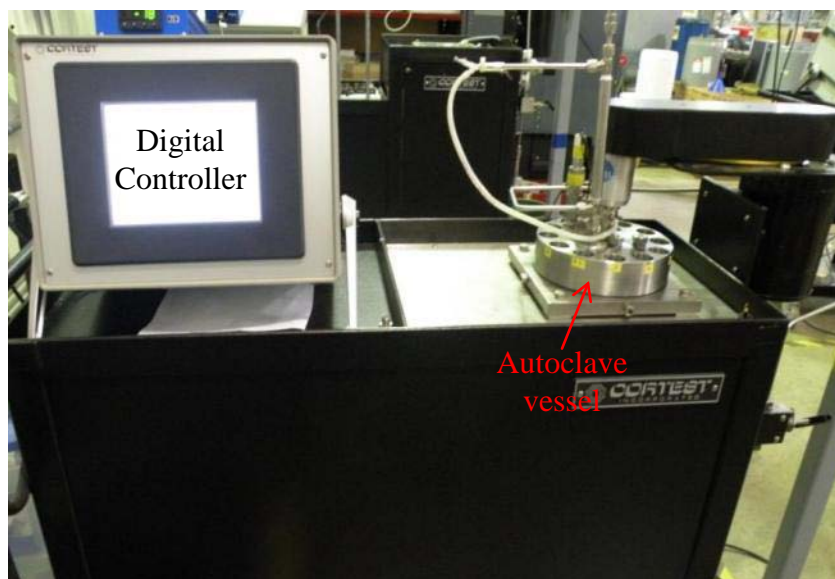
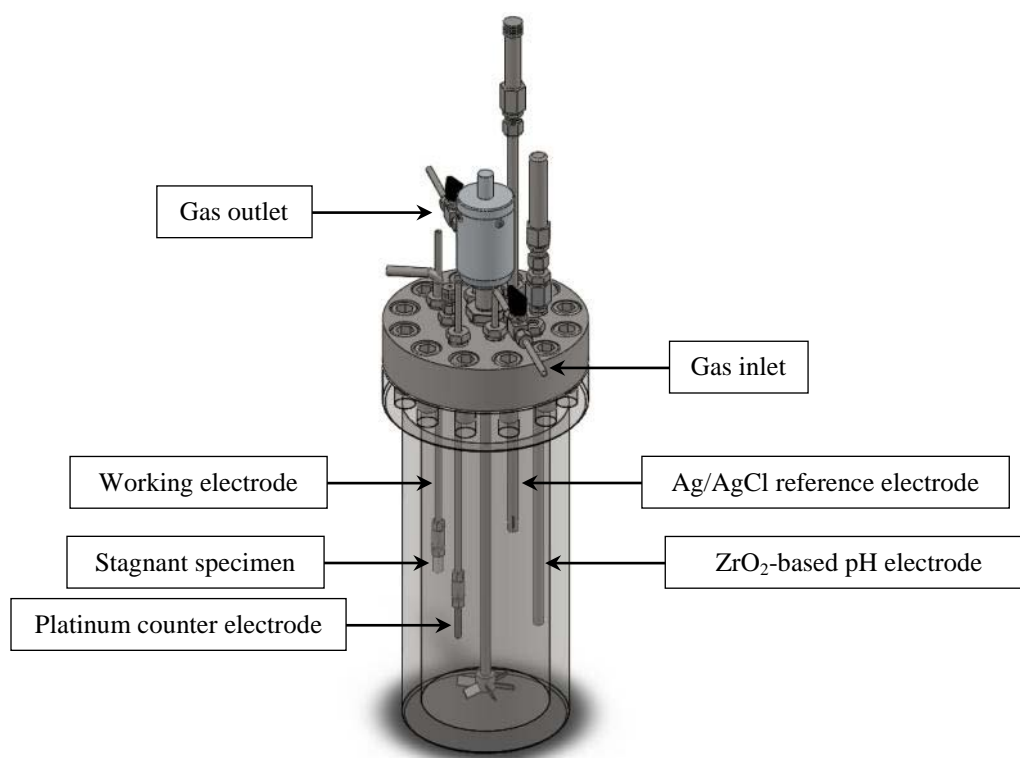
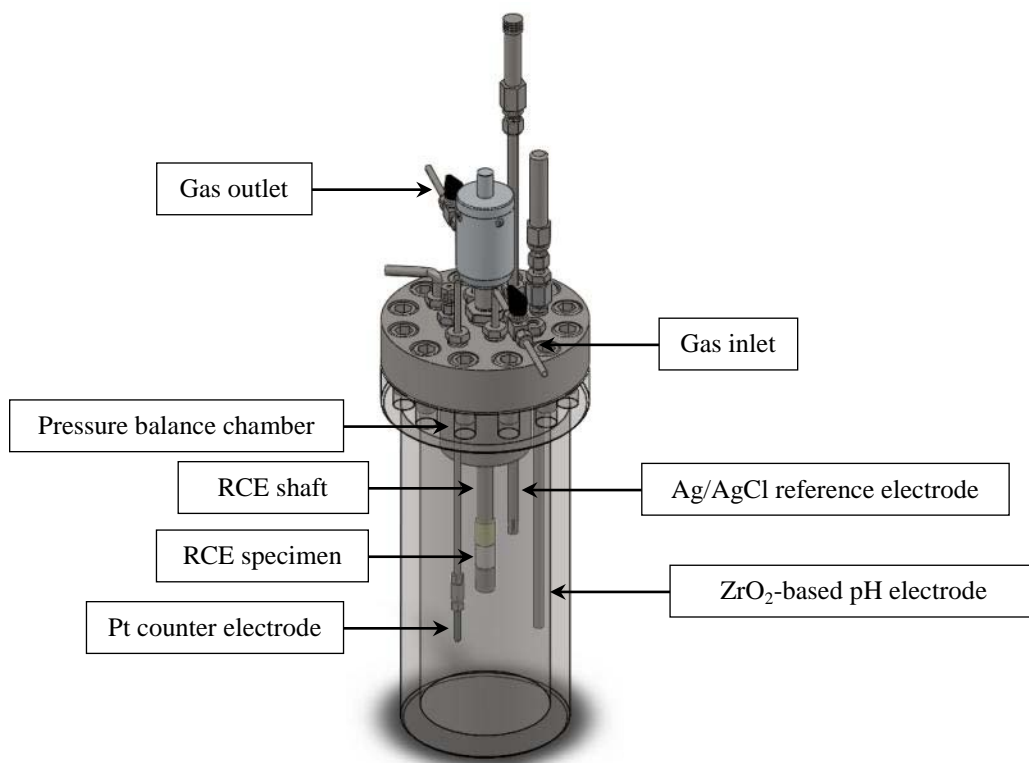


Figure 48. 4-Liter autoclave system from Cortest, Incorporated.

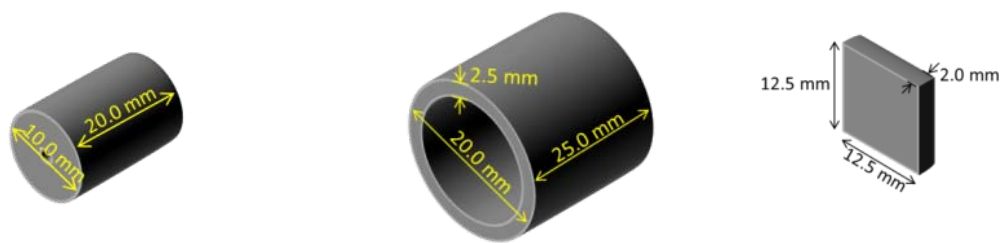


a. Stagnant conditions



b. Flowing conditions

Figure 49. Drawings of autoclave configurations with electrochemical measurements equipped.



a. Electrochemical specimen
in stagnant conditions

b. Electrochemical specimen in
flowing conditions

c. Flat specimen for
surface analysis

Figure 50. Drawings of specimen configuration.

Table 15. Effect of temperature on CO₂ solubility and pressure (calculated based on Chapter 2).

T (°C)	CO _{2, aq} (molar)	pCO ₂ (bar)	Total pressure (bar)
25	0.030	0.97	1.0
80	0.030	2.2	2.7
120	0.030	3.2	5.2
150	0.030	3.7	8.4
200	0.030	3.8	19.3

4.3 Results and discussion

4.3.1 Preliminary results at 25-80°C in corrosion product free environments

The test conditions are listed in Table 16. Two sets of the experiments were performed; the glass cell and autoclave tests. In the glass cell tests, the total pressure is always atmospheric - at 1 bar. With the effect of increasing temperature, the CO₂ solubility and vapor pressure of water increase, and the amount of dissolved CO₂ in solution decreases as it shows in Table 4 and Table 16. Figure 51 displays the potentiodynamic sweeps obtained from glass cell experiments at 25, 50 and 80°C. The results show that the cathodic curves slightly shifted forward when temperature increased. However, the anodic lines did not change significantly because of a decrease in the CO₂ solubility when the temperature increased. Therefore, the amount of the corrosive species related to the concentration of dissolved CO₂ in the solution decreases. These results are consistent with the results of Nešić, *et al.* [14]. The kinetic rate of the

anodic dissolution is not accelerated when the temperature increases because the anodic dissolution also depends on CO₂ concentration in the solution.

Table 16. Test conditions for Section 4.3.1.

Parameter	Set 1: Glass Cell			Set 2: Autoclave
	(Total pressure = 1 bar)			(Constant $c_{\text{CO}_2,\text{aq}}$ 0.030M)
System	2-Liter glass cell			4-Liter Autoclave
Material	API 5L X65			API 5L X65
Temperature (°C)	25	50	80	25, 50, 80
$c_{\text{CO}_2,\text{aq}}$ (molar)*	0.030	0.018	0.007	0.030
pH	4.0			4.0
Solution	1wt.% NaCl			1wt.% NaCl
Specimen surface finish (grit)	600 - uniform			600 - uniform
Electrochemical techniques	LPR and potentiodynamic sweep			LPR and potentiodynamic sweep

* See the water chemistry in Table 4 Set 1 and 3.

Unlike the experiments in a glass cell, the concentration of dissolved CO₂ in the solution was controlled at 0.030 M for each temperature in an autoclave i.e. the total amount of acid is constant with temperature and only the effect of temperature is investigated. The potentiodynamic sweeps from the autoclave experiments at 25, 50 and

80°C are shown in Figure 52. Both anodic and cathodic curves shifted forward when temperature increased.

The corrosion rates at different temperatures are shown in Figure 53. It is concluded that the corrosion rate increased when temperature increased in both cases. However, the corrosion rates in the glass cell experiments did not increase as high as those in the autoclave tests. This is because the CO₂ concentration in the solution decreased when the temperature increased in the glass cell.

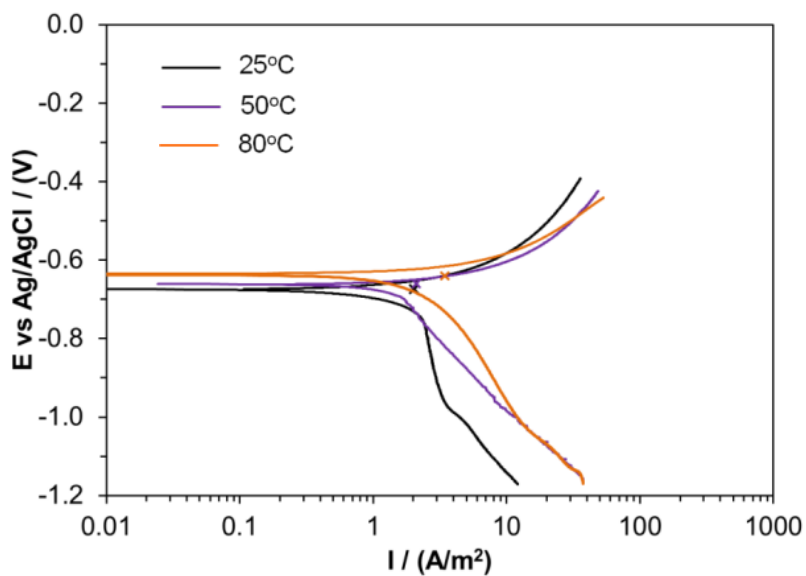


Figure 51. Potentiodynamic sweep: Glass cell tests, total pressure = 1 bar (test condition listed in Table 16, Set 1).

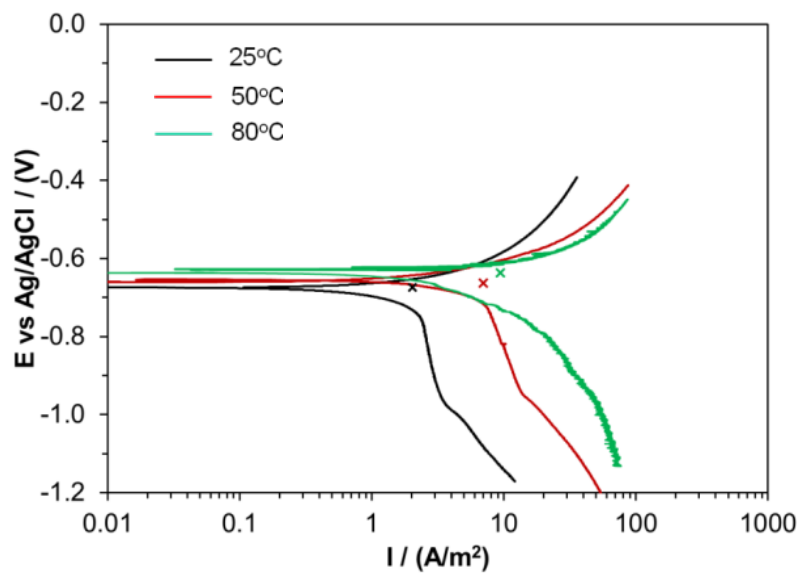


Figure 52. Potentiodynamic sweep: Autoclave tests, $c\text{CO}_2 = 0.030 \text{ M}$ (test condition listed in Table 16, Set 2).

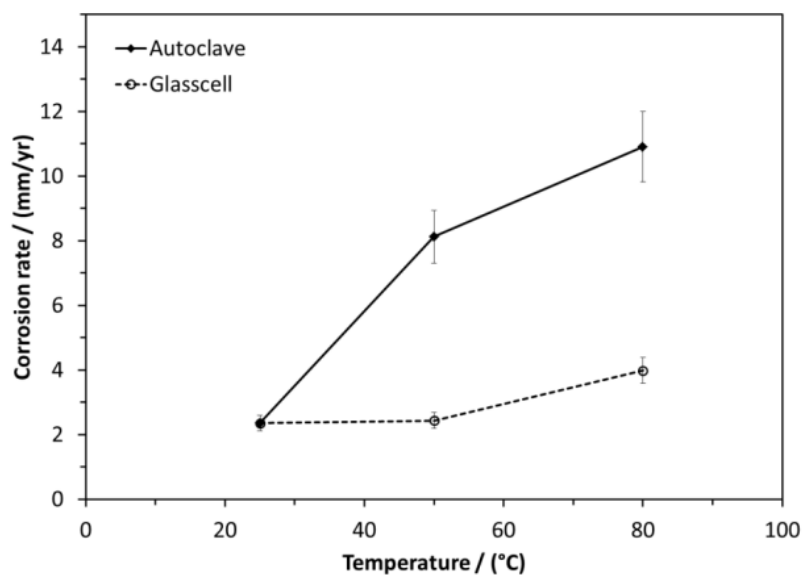


Figure 53. LPR corrosion rate vs temperature: 1 wt.NaCl%, pH 4.0, total pressure=1 bar for glass cell tests and $c\text{CO}_2 = 0.030 \text{ M}$ for autoclave experiments (test condition listed in Table 16).

4.3.2 Effect of specimen size

Since the experiments in the autoclave are considered to be a closed (constant inventory) system, the aqueous solution can become saturated over time with corrosion products: Fe^{2+} , leading to artifacts stemming from changing water chemistry. Therefore, to examine the extent of this problem, three different sizes of specimens were used in separate experiments, as shown in Figure 54. The effect of specimen size on the corrosion rate is shown in Figure 55. The initial corrosion rates for the three specimen were all high and then decreased with time because the corrosion product formed on the steel surfaces, as shown in Figure 56. Comparing the corrosion rates among the sizes of specimen, no significant difference in the corrosion rate was observed suggesting that this is not a significant concern in the current experimental setup.

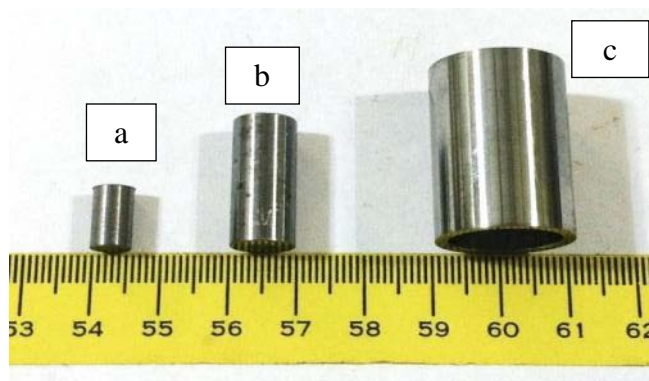


Figure 54. Specimens used in Section 4.3.2: a. $A/V=0.7\text{cm}^2/\text{l}$, b. $A/V=2.1\text{cm}^2/\text{l}$ and c. $A/V=6.3\text{cm}^2/\text{l}$.

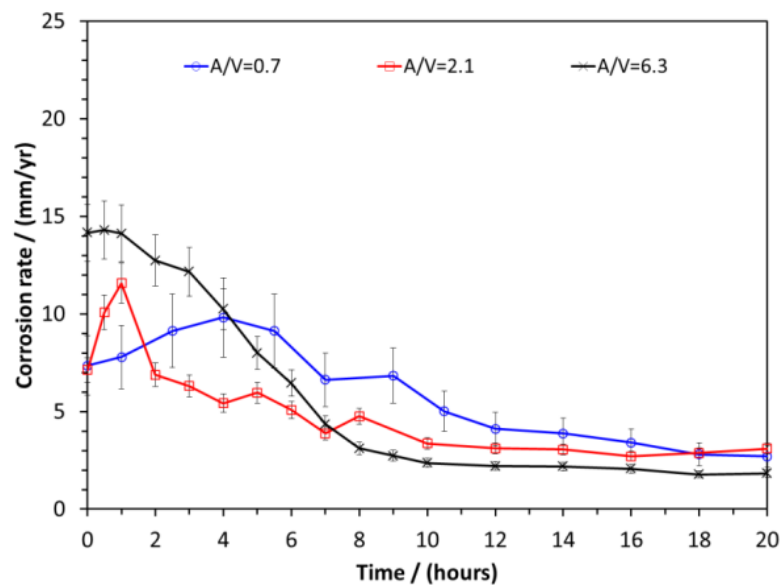
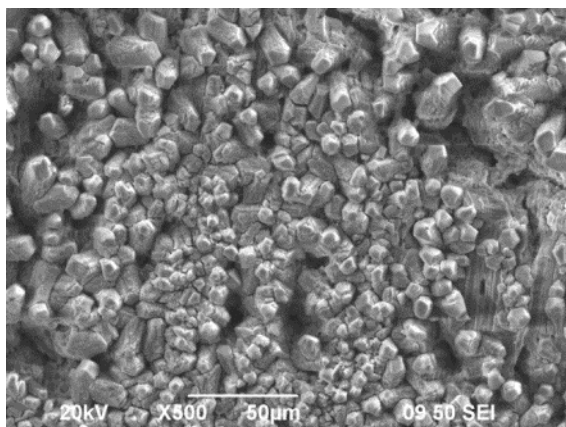
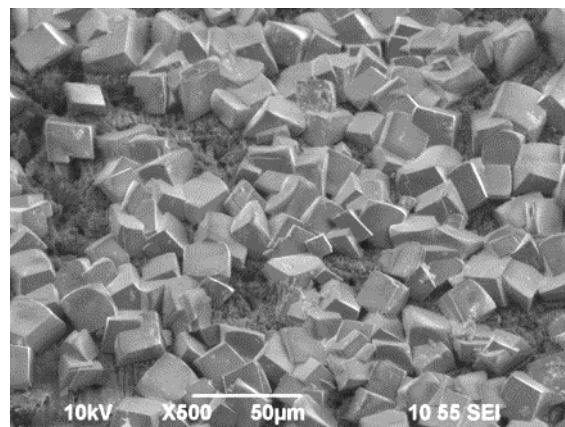


Figure 55. Effect of specimen size on corrosion rate over temperature; 120°C, 1 wt.%

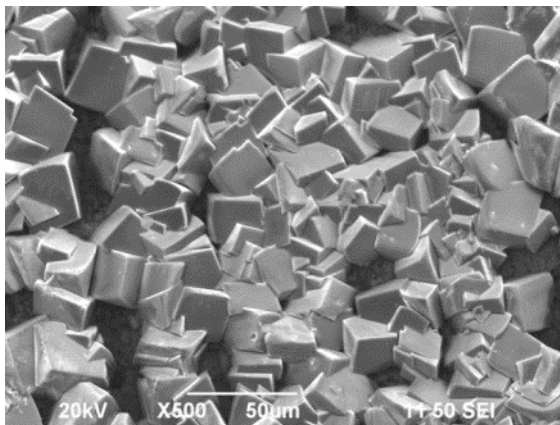
NaCl, $c\text{CO}_2 = 0.030 \text{ M}$, pH 4.0 (water chemistry in Table 4, Set C).



a. $A/V=0.7 \text{ cm}^2/\text{l}$



b. $A/V=2.1 \text{ cm}^2/\text{l}$



c. $A/V=6.3\text{cm}^2/l$

Figure 56. SEM images of the steel surface for different specimen sizes at 120°C, after 20 hours, corresponding to the corrosion rate results in Figure 55.

4.3.3 *Effect of pH*

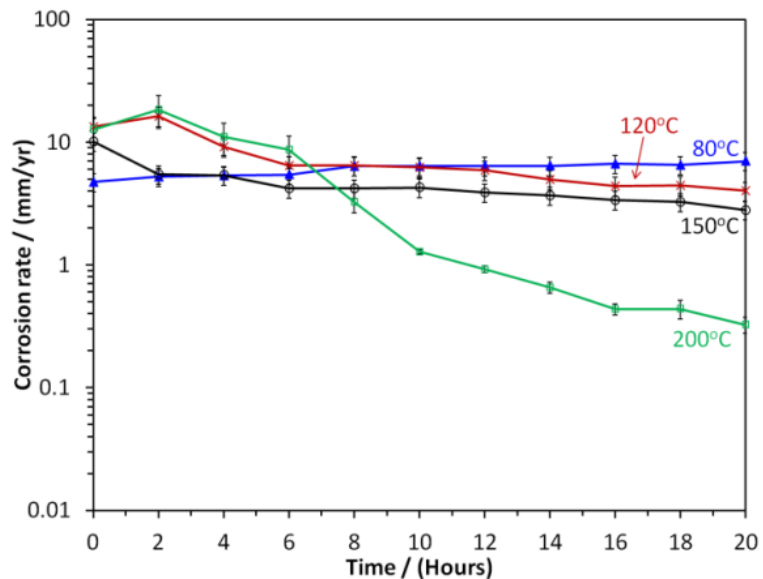
The effects of pH on CO₂ corrosion at temperatures of 80, 120, 150 and 200°C are summarized in Figure 57 a. and b. The test conditions are listed in Table 17. Starting with 80°C and pH 4.0, the corrosion rate remained constant with time. The EIS results are shown in Figure 58a. The Nyquist plot represents corrosion behavior indicative of the charge transfer process. The SEM image in Figure 59a. shows a uniformly corroded steel surface, and only iron was detected by EDX. In contrast, the corrosion rate at pH 6.0 in Figure 57 b. was initially high and then decreased with time, due to the formation of a protective FeCO₃ layer. The Nyquist plots in Figure 58 b. at 0 – 8 hours show semi-circles which is the characteristics of Faradaic impedance implying activity from corroding phenomena [104], [105]. However, at 20 hours it changed to a double semi-circle which indicated mass transfer dependence [104]. This means that the steel surface

became covered by a corrosion product layer as seen in the SEM image making it harder for species to diffuse and react (Figure 59 b.).

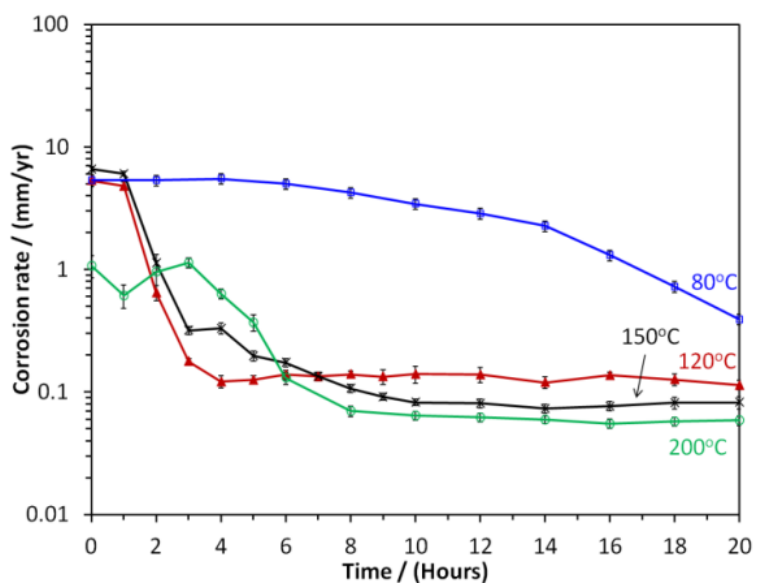
Table 17. Test matrix for the experiments in Section 4.3.3.

Parameter	Description
System	4-Liter Autoclave in stagnant conditions
Material	API 5L X65
Temperature (°C)	80, 120, 150, 200
cCO ₂ (molar)*	0.030
pH	4.0 and 6.0
Solution	1 wt.% NaCl
Specimen surface finish (grit)	600 - uniform
Test duration (hours)	20
Electrochemical techniques	LPR and EIS
Surface analysis	SEM and EDX, XRD

*See the water chemistry in Table 15.

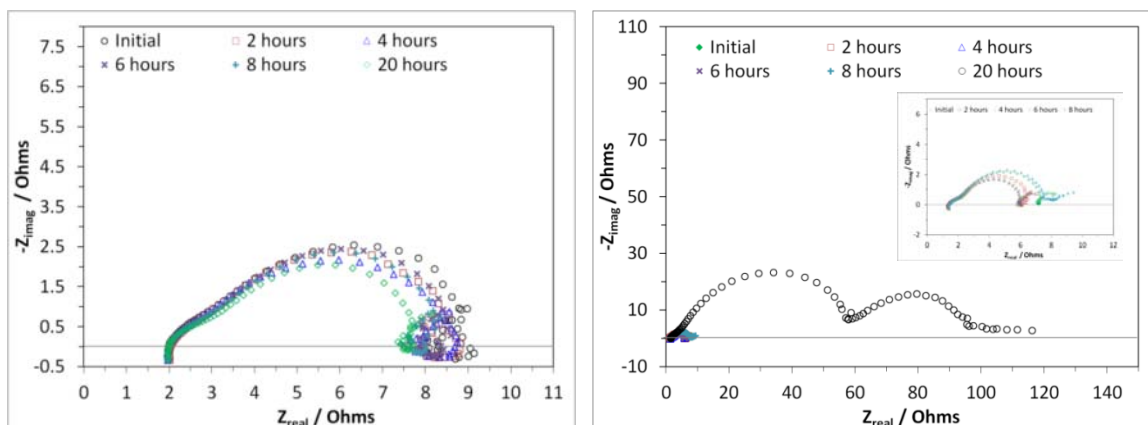


a. pH 4.0



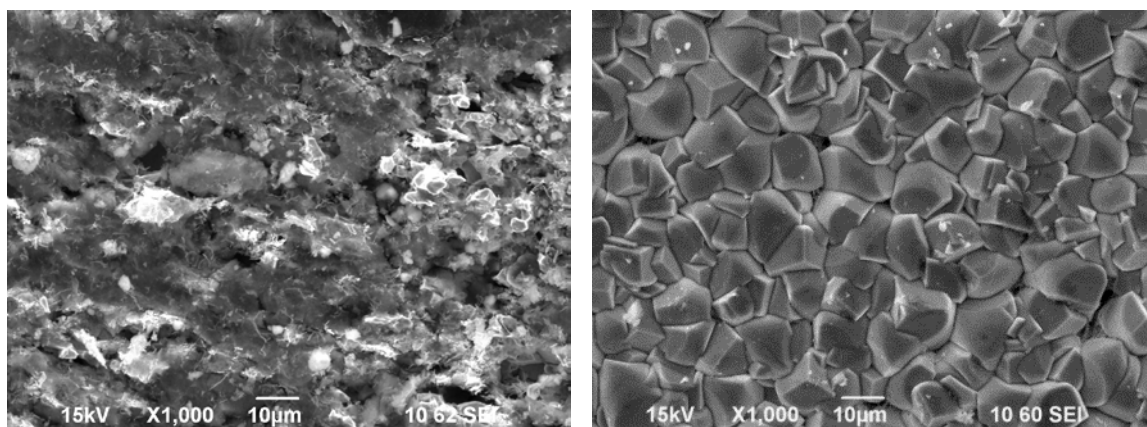
b. pH 6.0

Figure 57. LPR corrosion rate over time; $T=80\text{-}200^{\circ}\text{C}$, 1 wt.% NaCl, $c\text{CO}_2 = 0.030\text{ M}$, 20 hours.



a. pH 4.0

b. pH 6.0

Figure 58. EIS at 80°C, 1 wt.% NaCl, $c\text{CO}_2 = 0.030$ M, 20 hours.

a. pH 4.0

b. pH 6.0

Figure 59. SEM images at 80°C, 1 wt.% NaCl, $c\text{CO}_2 = 0.030$ M, 20 hours.

At 120°C, the measured corrosion rates at pH 4.0 and 6.0 were the highest at the beginning, and then decreased with time as illustrated in Figure 57 a. and b. For EIS analysis (Figure 60 a. and b.), the Nyquist plots showed semi-infinite linear diffusion for both cases at low frequency. However, the resistance in the test at pH 6.0 was two orders

of magnitude higher than that at pH 4.0. This is due to the formation of FeCO_3 layers, as presented in Figure 61 a. and b. The FeCO_3 layers at pH 6.0 more thoroughly covered the steel surface than those at pH 4.0. Therefore, the corrosion rate at pH 6.0 was lower than that at pH 4.0.

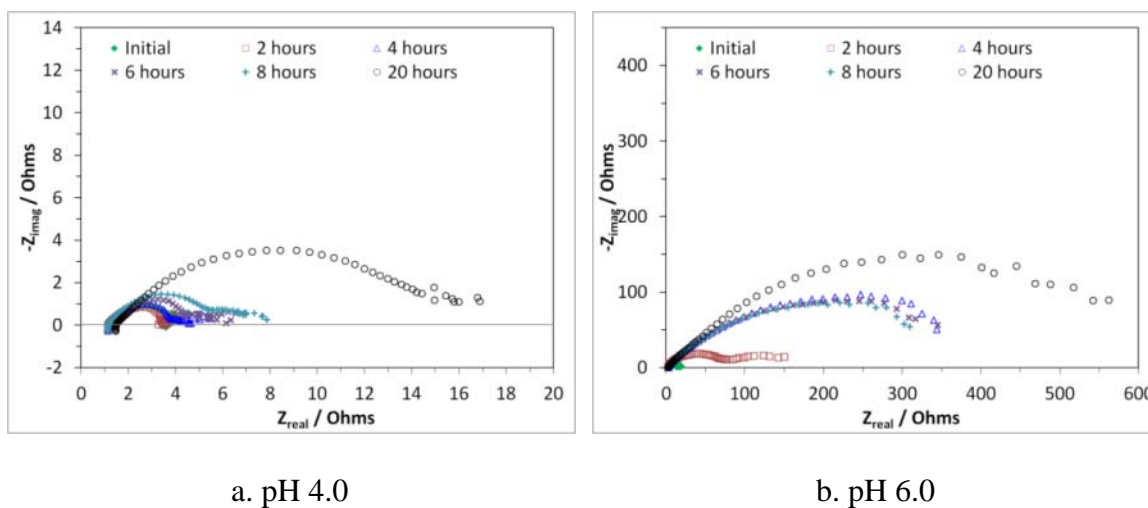
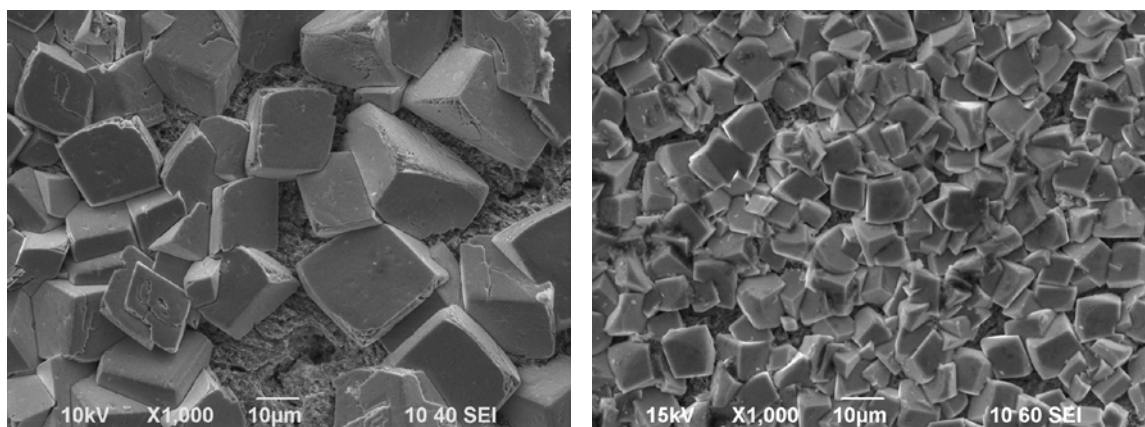
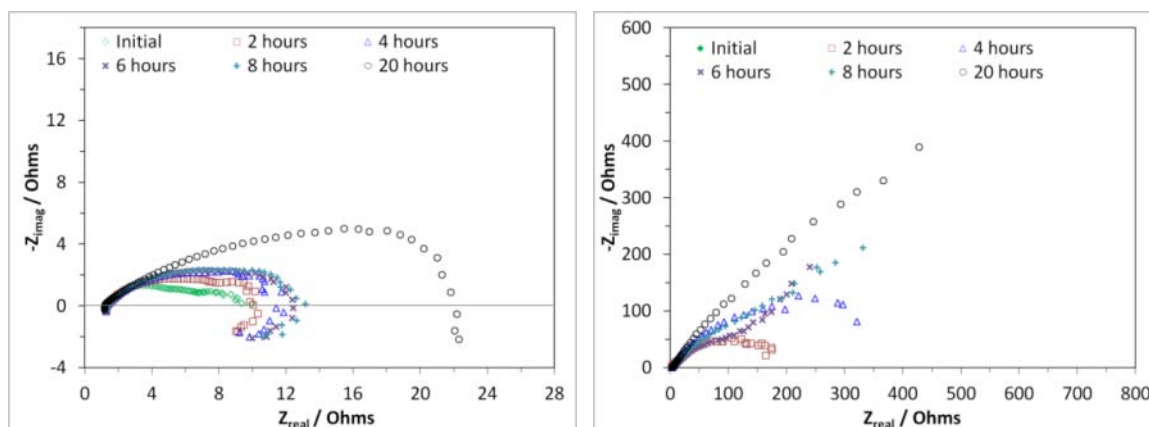


Figure 60. EIS at 120°C, 1 wt.% NaCl, $c\text{CO}_2 = 0.030$ M, 20 hours.



a. pH 4.0

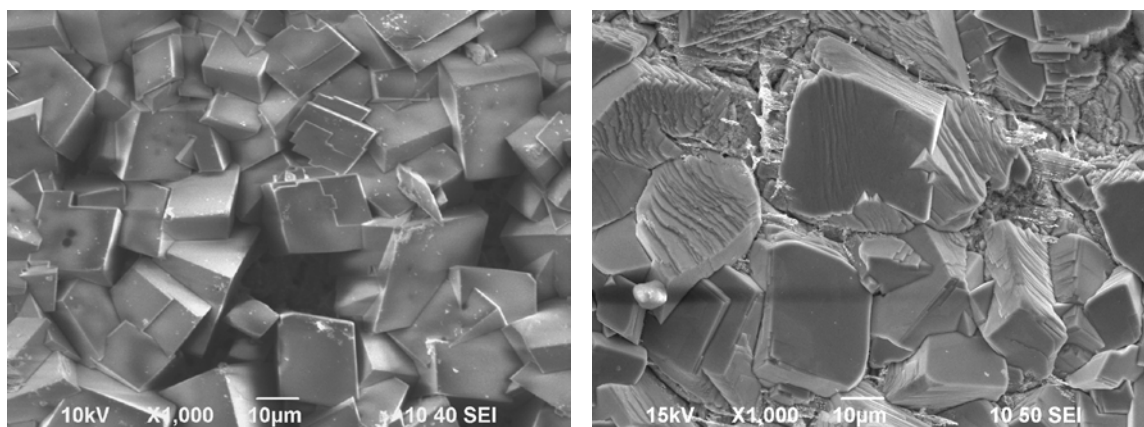
b. pH 6.0

Figure 61. SEM images at 120°C, 1 wt.% NaCl, $c\text{CO}_2 = 0.030 \text{ M}$, 20 hours.

a. pH 4.0

b. pH 6.0

Figure 62. EIS at 150°C, 1 wt.% NaCl, $c\text{CO}_2 = 0.030 \text{ M}$, 20 hours.

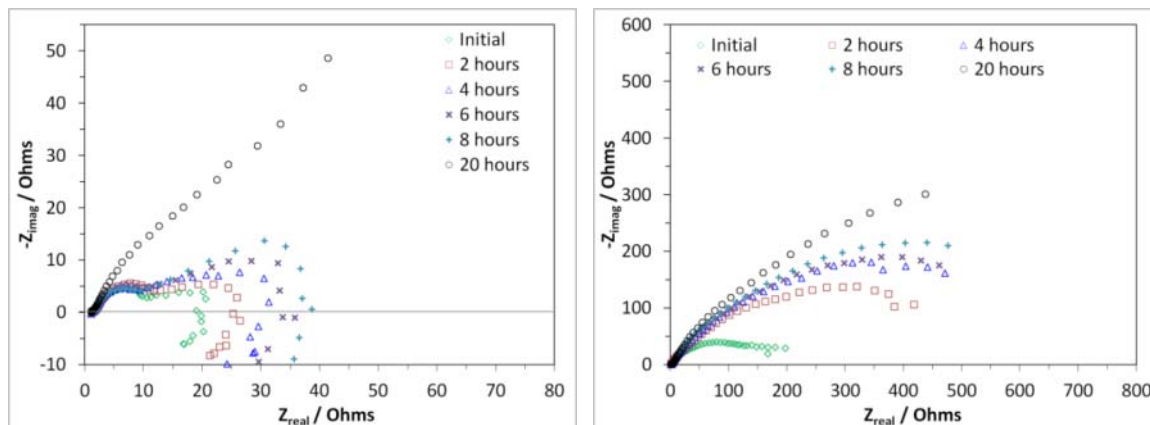


a. pH 4.0

b. pH 6.0

Figure 63. SEM images at 150°C, 1 wt.% NaCl, $c\text{CO}_2 = 0.030$ M, 20 hours.

At 150°C and 200°C, the corrosion rates (Figure 57 a. and b.), the Nyquist plots (Figure 62 and Figure 64), surface morphology (Figure 63 and Figure 65) for both pH 4.0 and 6.0 were similar to those results at 120°C. The corrosion rates at pH 4.0 were higher than those at pH 6.0. The semi-infinite linear diffusion appears on the Nyquist plots for both cases. The steel surfaces were covered by corrosion products. However, at pH 4.0 the Nyquist plots show an inductance behavior at low frequency at both 150°C and 200°C, which represents a multi-step process or any reaction that has intermediate steps, such as iron dissolution and magnetite formation [106–109]. At pH 6.0, the inductance loops did not appear on the Nyquist plot. This is due to much larger value for the resistance (real part) than on the reactance (imaginary part).

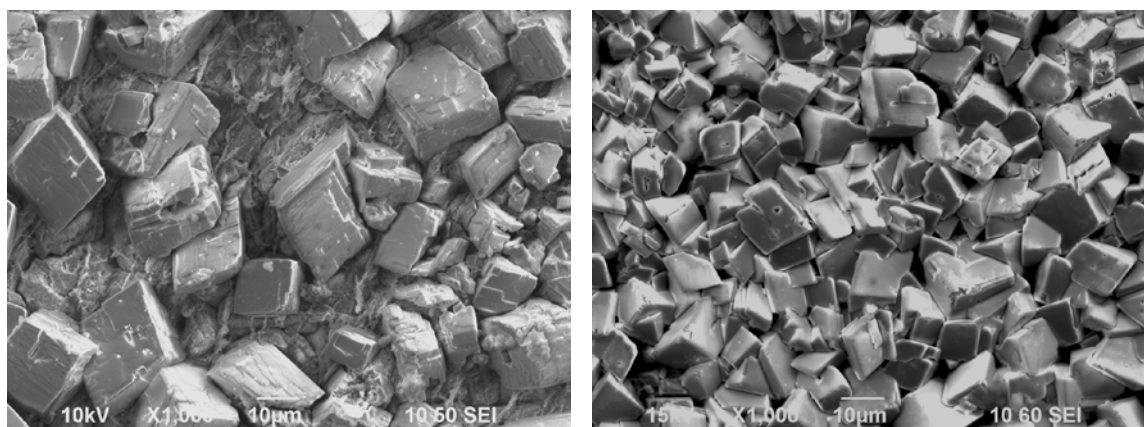


a. pH 4.0

b. pH 6.0

Figure 64. EIS at 200°C, 1 wt.% NaCl, $c\text{CO}_2 = 0.030 \text{ M}$, 20 hours.

For surface analysis, the steel surfaces for the experiments at 120, 150 and 200°C at the pH value of 4.0 were analyzed by XRD, as shown in Figure 66 a., b. and c., respectively. The results show that FeCO_3 was the main corrosion product at 120°C. A mixture of FeCO_3 and Fe_3O_4 was found at 150°C and 200°C. These corrosion products are thermodynamically favored, which can be confirmed by using the corrosion product predictions constructed based on the electrochemical thermodynamic principles in Chapter 3. Figure 68 a., b. and c. show the generated Pourbaix diagrams corresponding to the conditions in this section at 120, 150 and 200°C, respectively. The presence of Fe_3O_4 is expected at temperatures greater than 150°C with surface pH consideration.



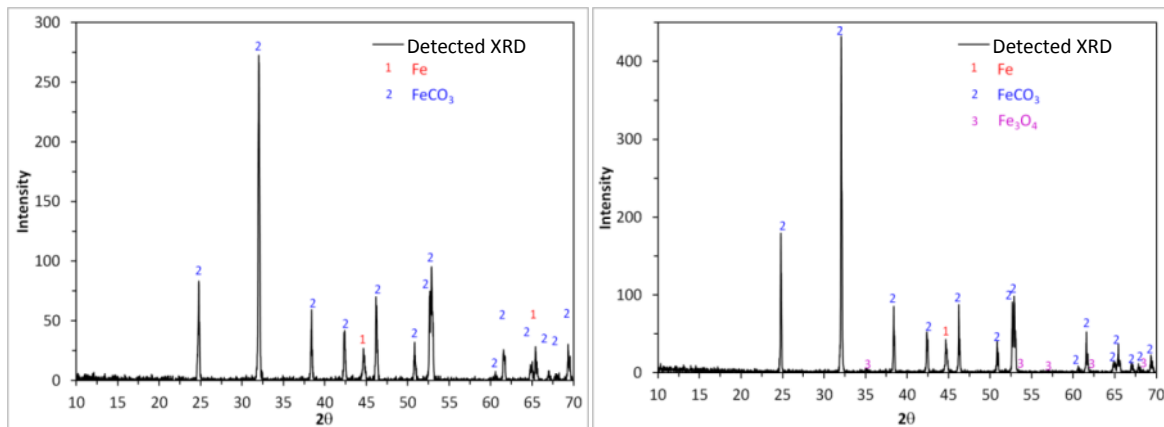
a. pH 4.0

b. pH 6.0

Figure 65. SEM images at 200°C, 1 wt.% NaCl, $c\text{CO}_2 = 0.030 \text{ M}$, 20 hours

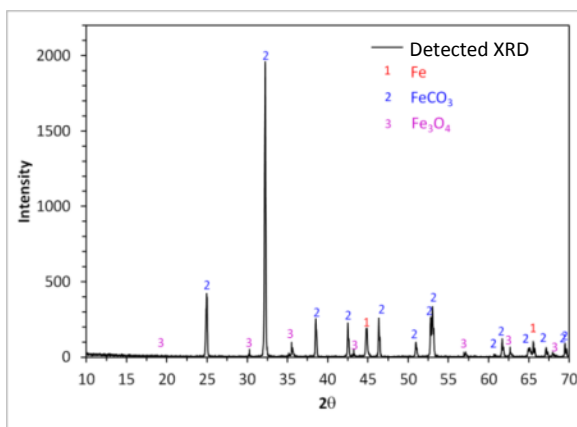
In all cases, the initial corrosion rates were much higher, releasing more corrosion products into the aqueous solution making the formation of FeCO_3 kinetically favorable [4], [50]. The higher the temperature, the higher the corrosion rate; this should be due to the accelerating kinetics of electrochemical and chemical reactions. However, the kinetics of FeCO_3 precipitation also increases with temperature [44]. Consequently, the corrosion rate is lowered because FeCO_3 forms on the steel surface and acts as a diffusion barrier [26], [81]. To be more precise, high corrosion rates mean the solutions had high concentration of Fe^{2+} . Once the Fe^{2+} and CO_3^{2-} concentrations become sufficiently large to exceed the FeCO_3 solubility limit (K_{sp}), FeCO_3 forms on the steel surface and the corrosion rate decreases over time. At 80°C and pH 4.0, the condition was thermodynamically unfavorable for FeCO_3 formation, so there was no FeCO_3 found on the steel surface. However, the equilibrium of FeCO_3 formation is shifted to lower pH when temperature increases [40], [86]. In other words, at higher temperature it is easier to

reach saturation with respect to FeCO_3 at low pH. At temperatures above 150°C , Fe_3O_4 is thermodynamically favored [40], [86]. Therefore, a mixture of FeCO_3 and Fe_3O_4 was observed.



a. 120°C corresponding to Figure 61

b. 150°C corresponding to Figure 63



c. 200°C corresponding to Figure 65

Figure 66. XRD analysis at pH 4.0, 1 wt.% NaCl, $c\text{CO}_2 = 0.030\text{ M}$, 20 hours.

Since a mixture of FeCO_3 and Fe_3O_4 is found at above 150°C , to locate the Fe_3O_4 on the steel surface, a back scatter cross section of the sample at 150°C was done (Figure

67 a.). The different contrast of image shows the different composition. The back scatter shows 4 different contrast areas (number 1-4 in Figure 67 a.). By the EDX analysis (Figure 67 b.), only Fe was detected in the first section ($\sim 0-3 \mu\text{m}$). At distance $\sim 3-5 \mu\text{m}$, Fe and O peaks were observed indicating Fe_3O_4 . Then, in the third section ($\sim 5-12 \mu\text{m}$), the intensity of the C element increased compared to the first and second sections. Therefore, it shows a presence of Fe, O and C or likely FeCO_3 . The last section ($\sim 12-14 \mu\text{m}$) had only C because it was an epoxy area. To summarize this observation, Fe_3O_4 was found in between Fe and FeCO_3 .

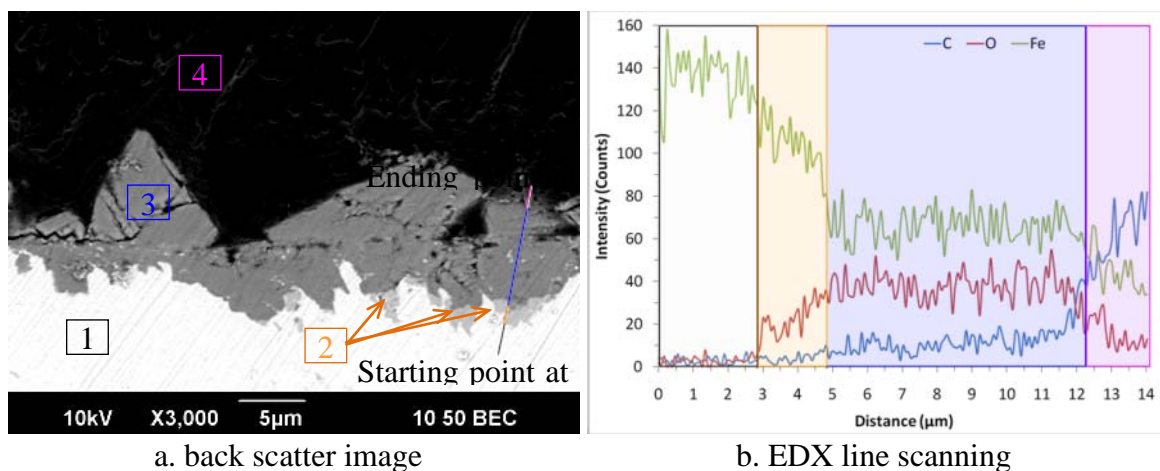
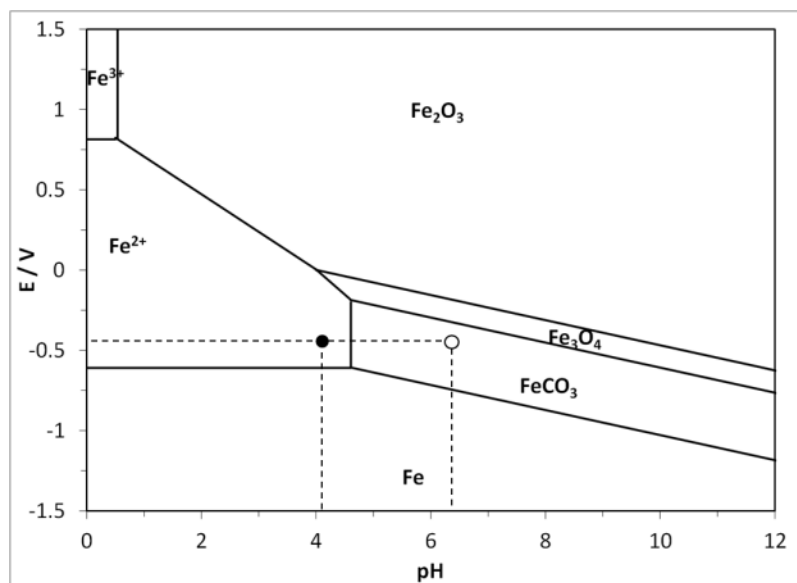
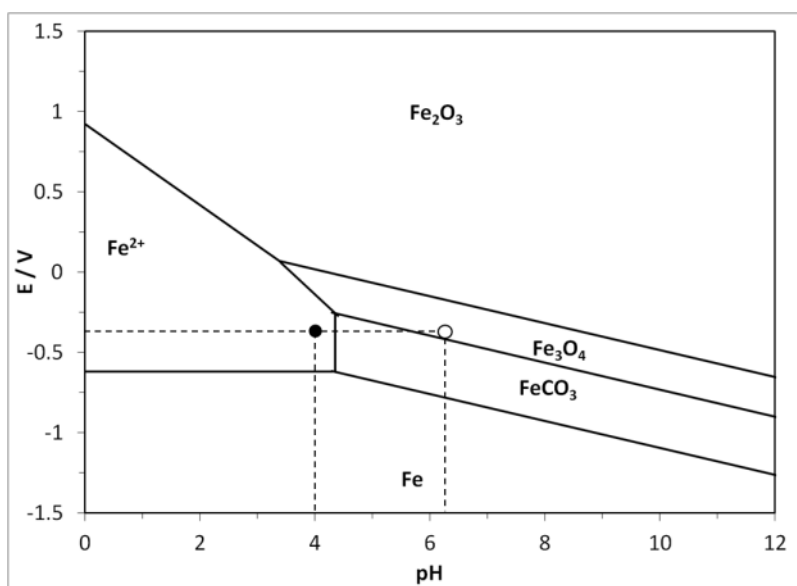


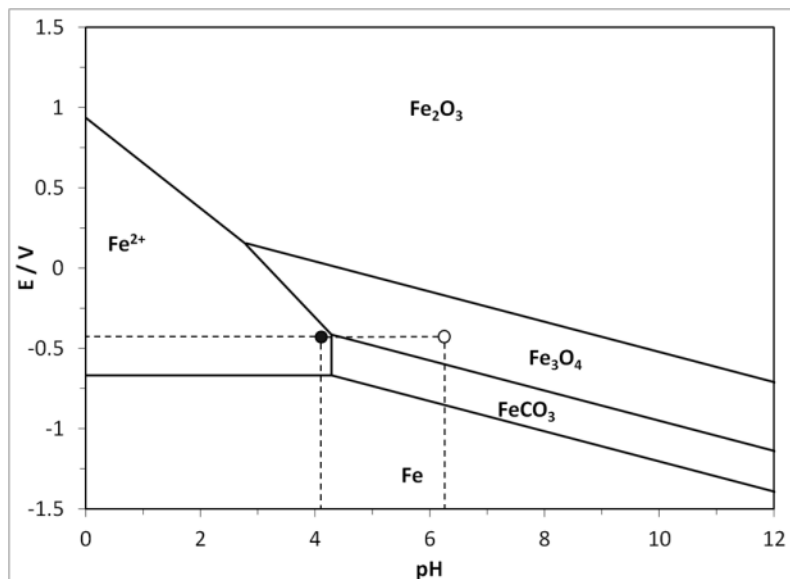
Figure 67. Cross-sectional analysis at 150°C , pH 4.0, 1 wt.% NaCl, $\text{cCO}_2 = 0.030 \text{ M}$, 20 hours, corresponding to Figure 63.



a. 120°C



b. 150°C



c. 200°C

Figure 68. Generated Pourbaix diagrams for Fe-CO₂-H₂O systems; cCO₂ = 0.030 M,

cFe²⁺ = 50 ppm. (● = bulk pH, ○ = surface pH).

To summarize the effect of pH on CO₂ corrosion over the temperature range of 25-250°C, the final corrosion rate from each temperature was plotted in Figure 69 and Figure 70 for pH 4.0 and 6.0, respectively. At pH 4.0, the corrosion rate increased with temperature. However, it decreased at temperature above 80°C due to the formation of protective corrosion product layer on the steel surface. At pH 6.0, the corrosion rate decreased with temperature because of the corrosion product formation. The higher pH is more favorable for the formation of corrosion product as described in Chapter 3.

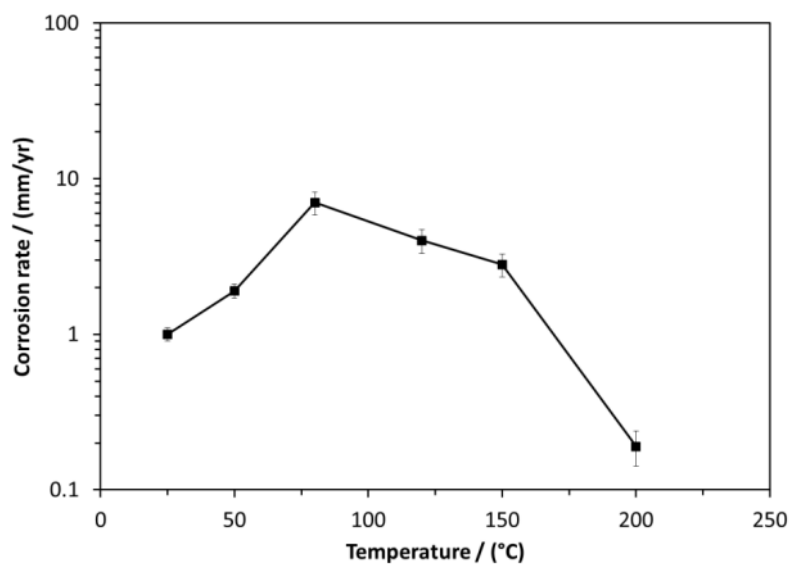


Figure 69. LPR corrosion rate at 20 hours vs temperature: 1 wt.% NaCl, $c\text{CO}_2 = 0.030$ M, pH 4.0.

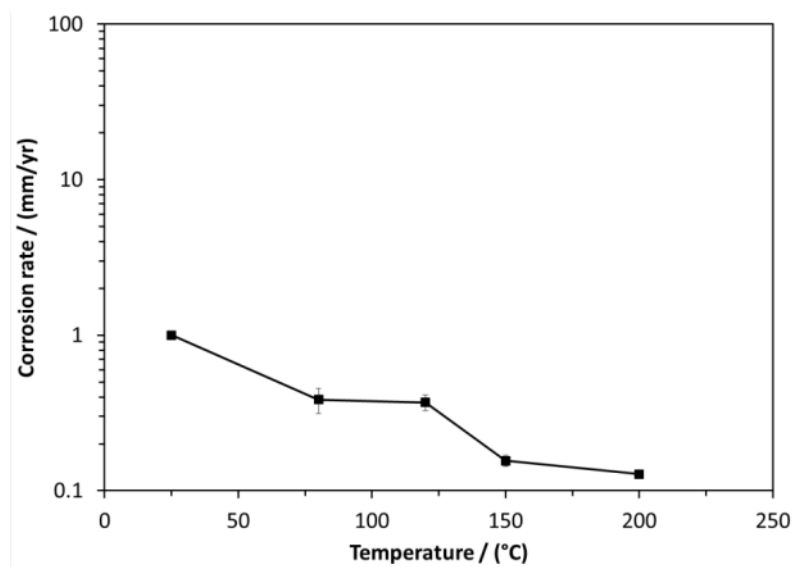


Figure 70. LPR corrosion rate at 20 hours vs temperature: 1 wt.% NaCl, $c\text{CO}_2 = 0.030$ M, pH 6.0.

4.3.4 *Effect of flow*

The effect of flow on CO₂ corrosion behavior at 120°C was studied using RCE. The test matrix is listed in Table 18. Figure 71 shows the corrosion rate from LPR at 120°C over time and Figure 72 shows the relationship between the corrosion rate at 20 hours and rotating speed. From the experiments, the corrosion rates decreased with time for all rotating speeds due to the formation of corrosion product layers (Figure 74). However, the corrosion rates at 100 rpm were the lowest. In Figure 73, the EIS spectrum shows diffusion dependent corrosion mechanisms for all cases.

By visual comparison of SEM images (Figure 74) from each test, it can be seen that the FeCO₃ crystals appear damaged at 1000 rpm (Figure 74 d.). This can be explained by using the generated Pourbaix diagram (Figure 75). Considering that the main corrosion product was FeCO₃, the surface pH must have been higher than the bulk pH. Without flow, the concentration of Fe²⁺ with corrosion will increase the pH, but, with flow, mass transfer of species reduces the difference in pH between the surface and the bulk conditions. In other words, the value of surface pH was close to bulk pH, and then the condition becomes under-saturation for the FeCO₃ formation. Thus, the FeCO₃ crystals dissolved back or were chemically damaged resulting in the increase in the corrosion rate at higher flow rate. The decrease in surface pH by flow to the bulk pH was confirmed experimentally by Ning [110].

The effects of flow were further investigated by varying the rotating speed at the beginning and the end of the test. Figure 76 a. shows the LPR corrosion rates for the first 6 hours. For the first hour, a “non-flowing condition” was used (0 rpm). After that, the

rotation rate was set at 100 rpm, 1000 rpm and 100 rpm for the second, third and fourth hours, respectively. The result shows that the corrosion rates increased and decreased as a function of flow rate. However, after 4 hours, the corrosion rates continuously decreased even if the flow rate was increased (Figure 76 b.). This was due to the formation of a protective corrosion product layer as shown in Figure 77. The results were consistent with the work done by Nešić, *et al.*[60].

Table 18. Test matrix for the experiments in Section 4.3.4.

Parameter	Description
System	4-Liter Autoclave in flow conditions (using rotating cylindrical electrode)
Material	API 5L X65
Temperature (°C)	120 and 200
cCO ₂ (molar) [*]	0.030
pH	4.0
Solution	1 wt.% NaCl
Rotating speed (rpm)	0, 100, 500 and 1000 ^{**}
Specimen surface finish (grit)	600 - uniform
Test duration (hours)	20
Electrochemical techniques	LPR and EIS
Surface analysis	SEM and EDX

^{*} See the water chemistry in Table 15.

^{**} Equivalent to 0, 0.1, 0.5 and 1 m/s, respectively.

At 200°C, the LPR corrosion rates (Figure 78) for 0, 100 and 1000 rpm had a similar trend. The flow-sensitivity of CO₂ corrosion at this temperature was not observed. All experiments started at high corrosion rate and decreased with time. Figure 80a. – c. show the SEM images for the experiments at 0, 100 and 1000 rpm, respectively. For 100 and 1000 rpm tests, FeCO₃ crystals did not entirely cover the surface; however, the corrosion rates did not increase with flow. The final corrosion rate was not significantly sensitive to the rotating speed as shown in Figure 79. This may be because the surface was not only covered by FeCO₃, but also a very thin Fe₃O₄ layer.

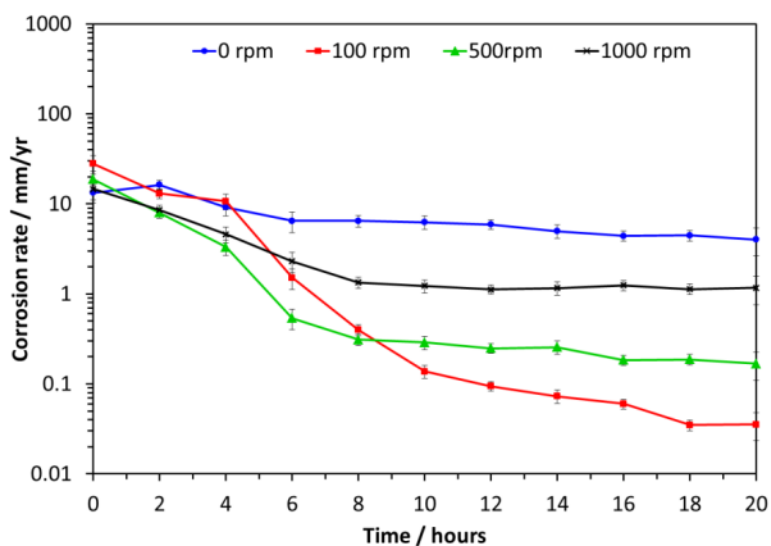


Figure 71. LPR corrosion rates at 120°C, pH 4.0, 1 wt% NaCl, cCO₂ = 0.030 M; Rotating speeds of 0, 100, 500 and 1000 rpm (equivalent to 0, 0.1, 0.5, 1.0 m/s, respectively).

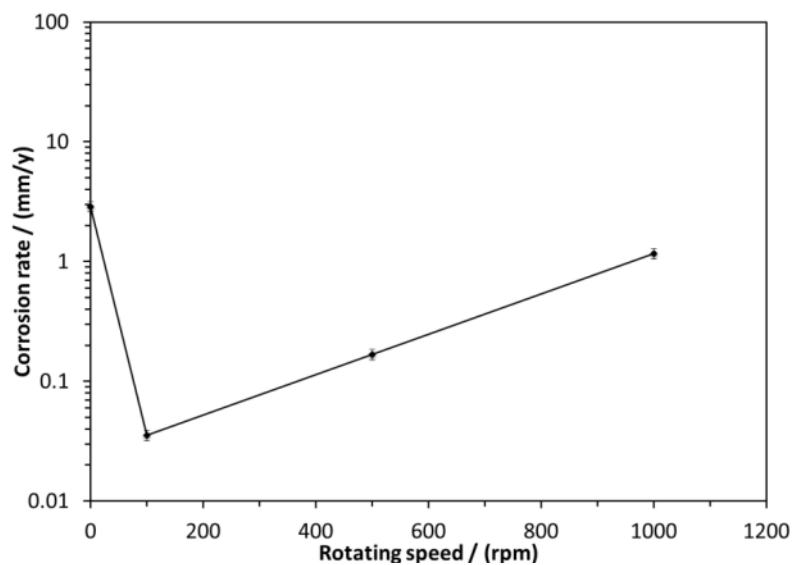
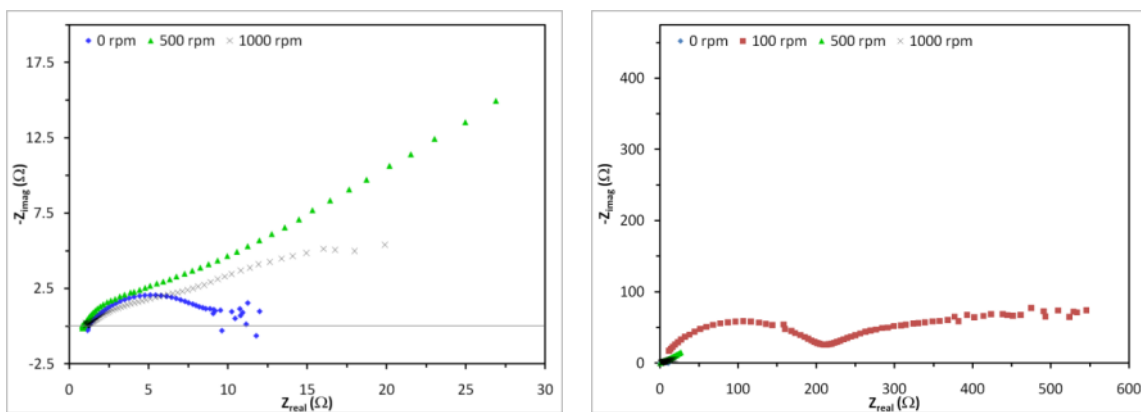


Figure 72. LPR corrosion rates at 20 hours: 120°C, pH 4.0, 1 wt% NaCl, $c\text{CO}_2 = 0.030\text{M}$:
0, 100, 500 and 1,000rpm (equivalent to 0, 0.1, 0.5 and 1.0 m/s, respectively).



a. 0, 500 and 1,000 rpm

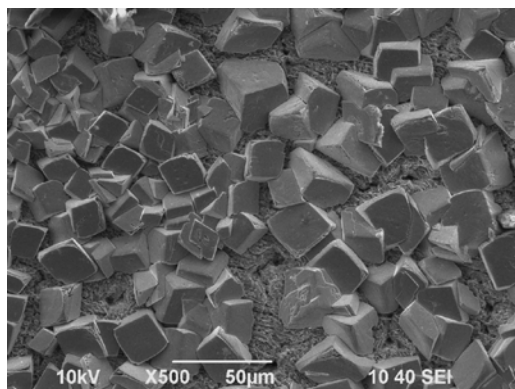
(equivalent to 0, 0.5 and 1.0m/s,

respectively)

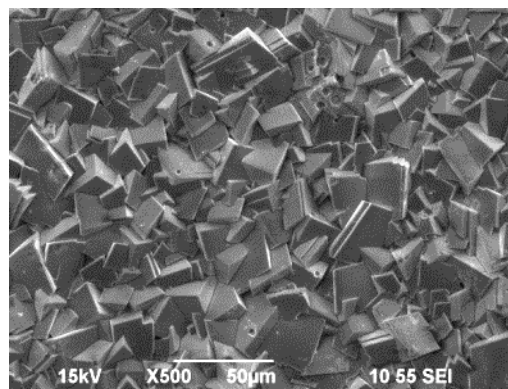
b. 100 rpm

(equivalent to 0.1 m/s)

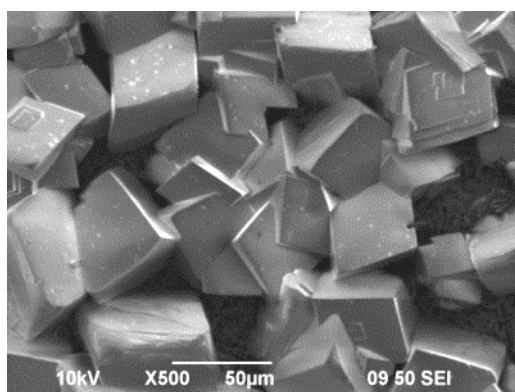
Figure 73. EIS spectrum at 120°C, pH 4.0, 1 wt% NaCl, $c\text{CO}_2 = 0.030\text{ M}$, 20 hours.



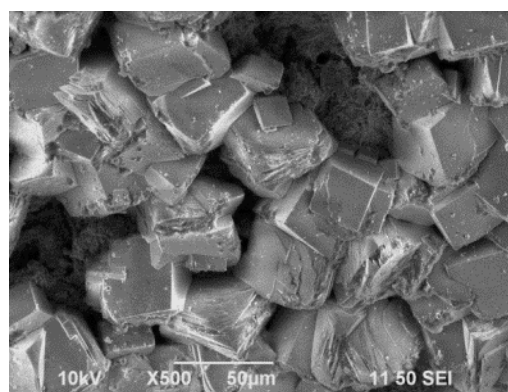
a. 0 rpm



b. 100rpm (equivalent to 0.1 m/s)



c. 500 rpm(equivalent to 0.5 m/s)



d. 1,000rpm (equivalent to 1.0 m/s)

Figure 74. SEM images of flow effects at 120°C, pH 4.0, 1 wt.% NaCl, $c\text{CO}_2 = 0.030 \text{ M}$,
20 hours.

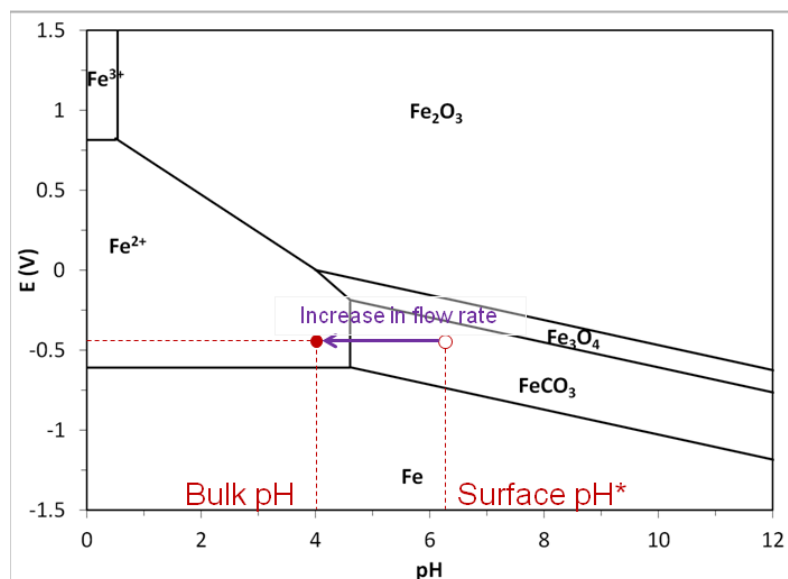
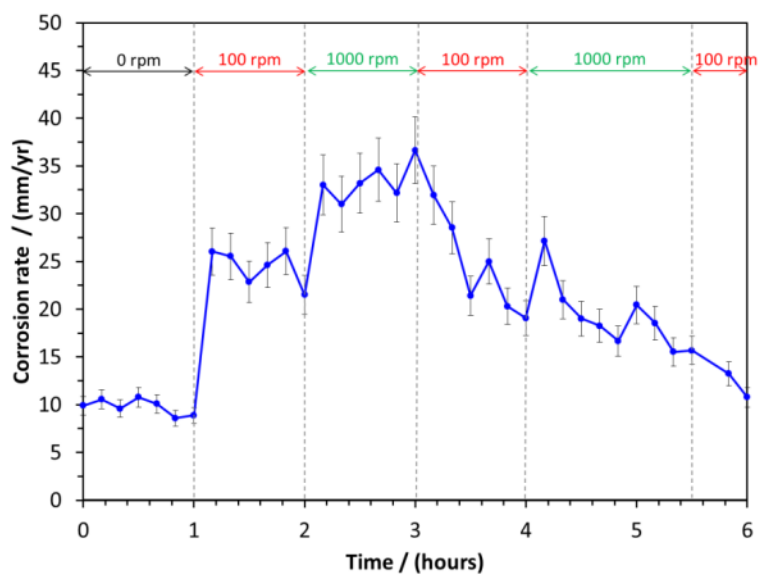
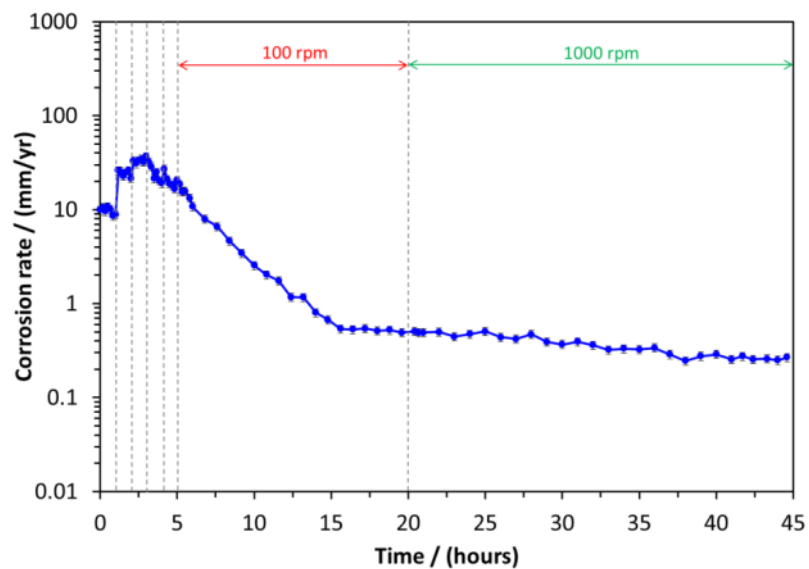


Figure 75. Generated Pourbaix diagram at 120°C, $c\text{CO}_2 = 0.030 \text{ M}$, $c\text{Fe}^{2+} = 50 \text{ ppm}$. (• = bulk pH, o = surface pH).



a. 0-6 hours



b. 0-46 hours

Figure 76. LRP corrosion rates with varying flow rates; at 120°C, pH 4.0, 1 wt.% NaCl, $c\text{CO}_2 = 0.030 \text{ M}$.

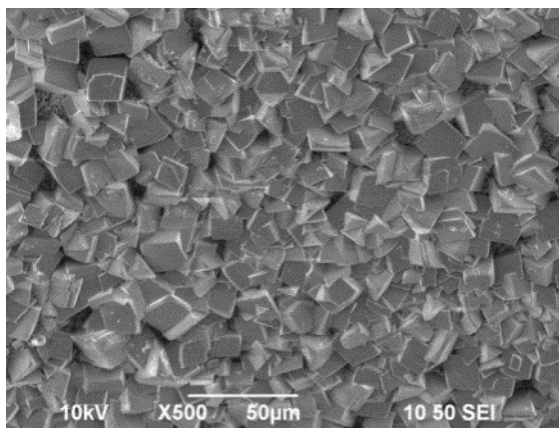


Figure 77. SEM image from the test at 120°C, pH 4.0, 1 wt.% NaCl, $c\text{CO}_2 = 0.030 \text{ M}$, after 46 hours.

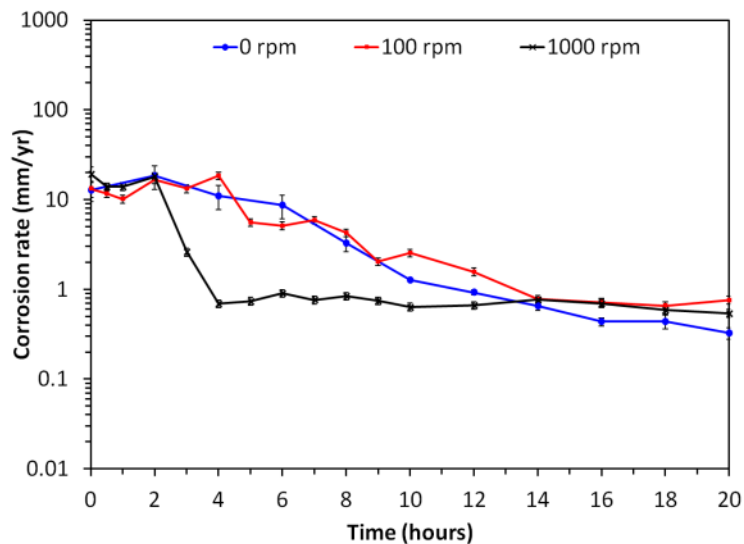


Figure 78. LPR corrosion rates at 200°C, pH 4.0, 1 wt.% NaCl, $c\text{CO}_2 = 0.030\text{M}$; Rotating speeds of 0, 100 and 1,000rpm (equivalent to 0, 0.1 and 1.0m/s, respectively).

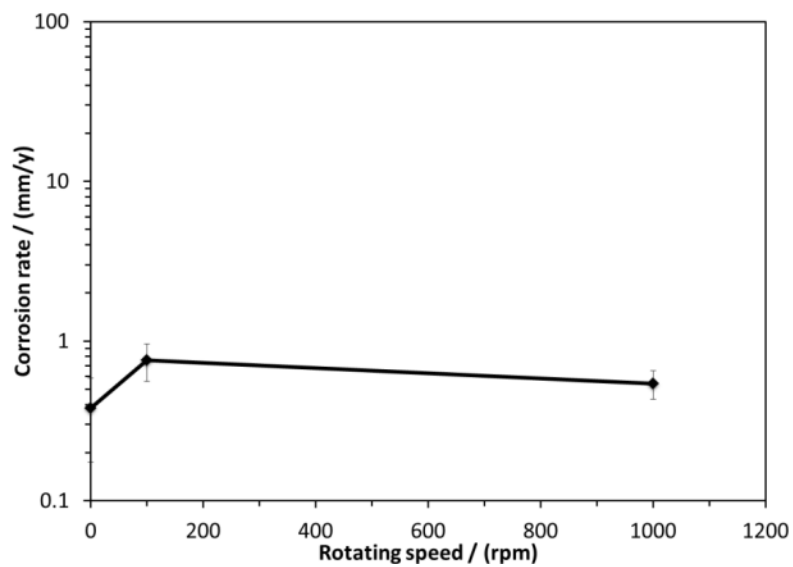
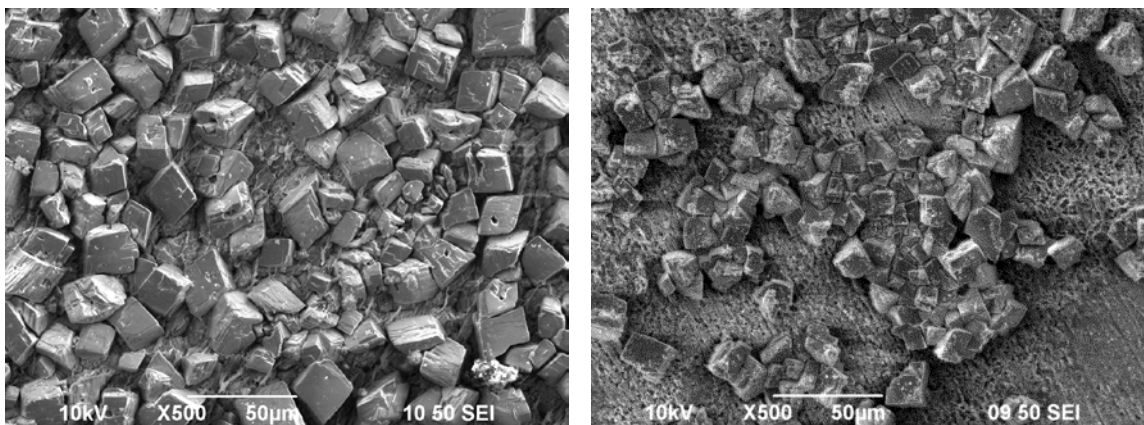
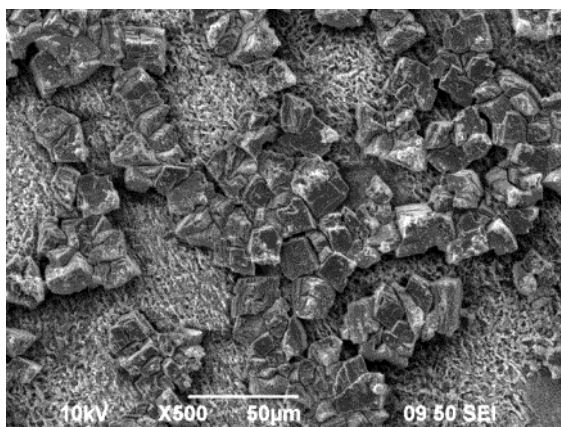


Figure 79. LPR corrosion rates at 20 hours: 200°C, pH 4.0, 1 wt.% NaCl, $c\text{CO}_2 = 0.030\text{M}$: 0, 100 and 1,000rpm (equivalent to 0, 0.1 and 1.0 m/s, respectively).



a. 0 rpm

b. 100 rpm (equivalent to 0.1 m/s)



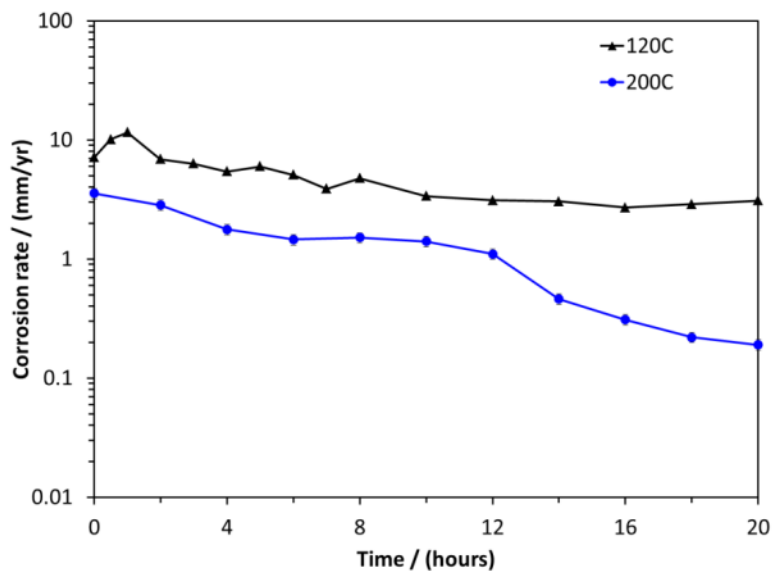
c. 1000 rpm (equivalent to 1.0 m/s)

Figure 80. SEM images at 200°C, pH 4.0, 1 wt.% NaCl, $c\text{CO}_2 = 0.030\text{M}$, 20 hours.

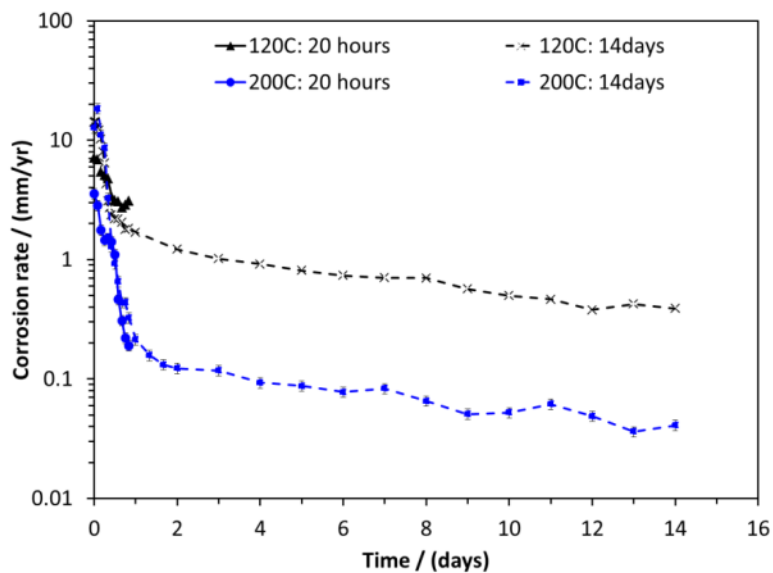
4.3.5 Long-term experimental study

From the 20-hour exposure experiments at 120 and 200°C in Section 4.3.3 (Figure 81a.), the corrosion rates decreased with time. However, the corrosion rate at 200°C was still decreasing and being an order of magnitude lower than that at 120°C after 20 hours. Therefore, the duration of these experiments were extended to 14 days. From Figure 81 b., the results shows that the corrosion rates at both temperatures

dramatically decreased with time, but they slightly changed after 2 days due to the corrosion product layers entirely covering the surfaces of both samples as shown in Figure 83 a. and Figure 88 a., respectively. Figure 87 a. and b. show EIS spectra for the experiments at 120 and 200°C, respectively. Those Nyquist plots demonstrate diffusion impedance (not semi-circle impedance) or infinite impedance. This implied that there is a diffusion barrier on the steel surface confirming formation of corrosion products on the sample surfaces and retarding the anodic dissolution of iron [102], [111] according to an increase in open circuit or corrosion potentials (Figure 82). By XRD analysis, the FeCO_3 crystals covered the steel surface at 120°C (Figure 83 b.) while a mixture of FeCO_3 and Fe_3O_4 was detected on the surface at 200°C (Figure 88 b.).



a. 0-20 hours



b. 0-14 days

Figure 81. LPR corrosion rates at 120 and 200°C, pH 4.0, 1 wt.% NaCl, $c\text{CO}_2 = 0.030$ M.

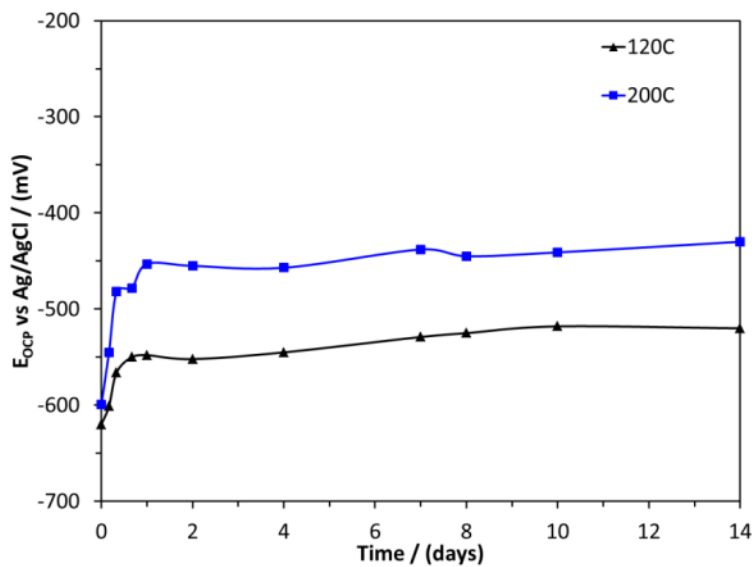
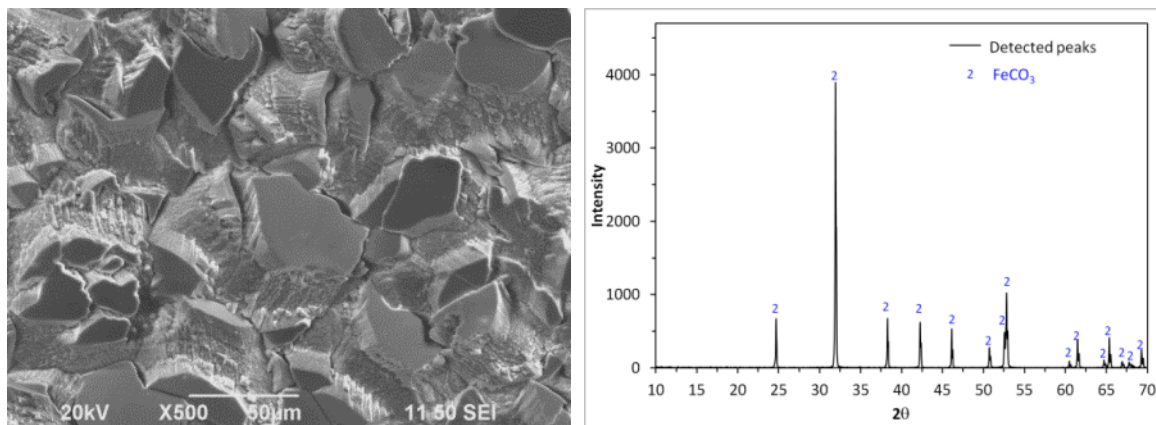


Figure 82. Open circuit potentials over time at 120 and 200°C, pH 4.0, 1 wt.% NaCl, $c\text{CO}_2 = 0.030$ M.



a. SEM

b. XRD

Figure 83. Surface analysis at 120°C, pH 4.0, 1 wt.% NaCl, $c\text{CO}_2 = 0.030 \text{ M}$, 14 days.

The surfaces of the samples tested at 120°C and 200°C were further characterized. At 120°C, the cross-section back-scatter images for 2 locations are shown in Figure 84. Uniform corrosion was observed for Location 1, but pitting ($\leq 50 \mu\text{m}$) was observed for Location 2. Figure 85 shows the surface after corrosion product removal, indicating multiple pitting locations. From IFM (Figure 86), the maximum depth was about 76 μm making the calculated pitting penetration rate more than 2 mm/yr. Compared to 0.7 mm/yr general corrosion rate, these may be considered to be possible pitting initiation locations. At 200°C, the cleaned surface (Figure 89) shows the similar morphology to that at 120°C. Nevertheless, from Figure 90, the maximum pit penetration depth by IFM was around 25 μm , so the pitting penetration rate was about 0.7 mm/yr. Compared to 0.5 mm/yr general corrosion rate, this is not considered to be pitting corrosion.

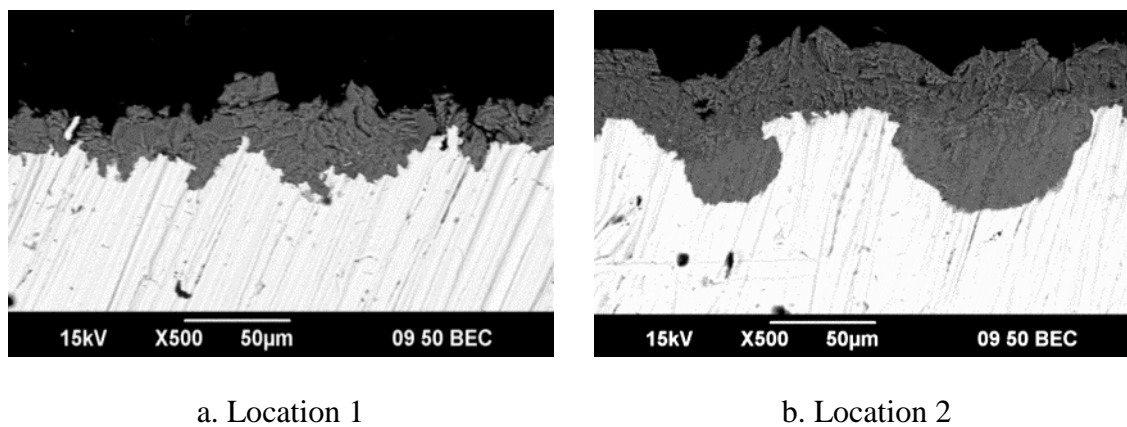


Figure 84. Back-scatter cross-sections for 120°C, pH 4.0, 1 wt.% NaCl, $c\text{CO}_2 = 0.030 \text{ M}$, 14 days.

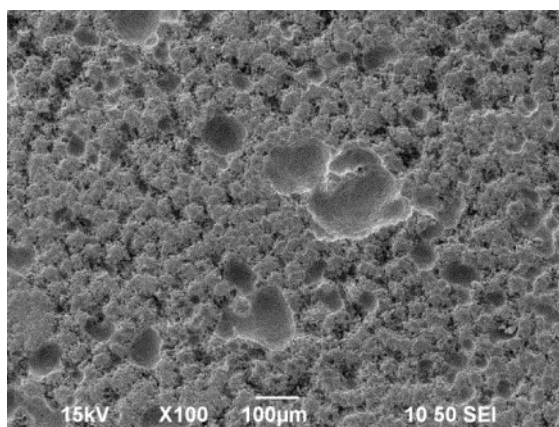
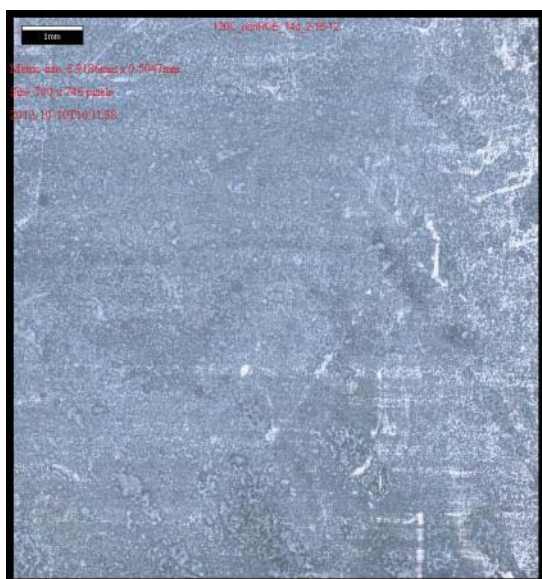
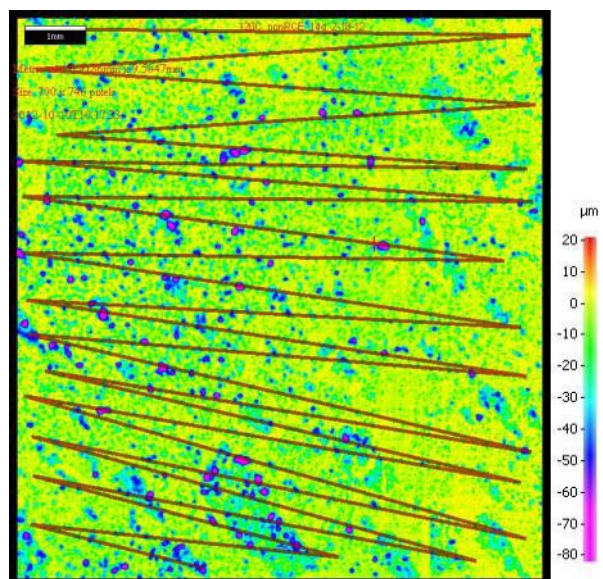


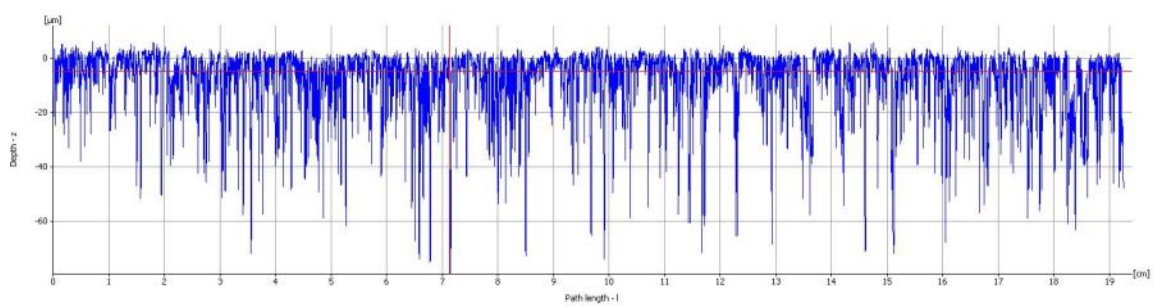
Figure 85. Surface after corrosion product removal at 120°C, pH 4.0, 1 wt.% NaCl, $c\text{CO}_2 = 0.030 \text{ M}$, 14 days.



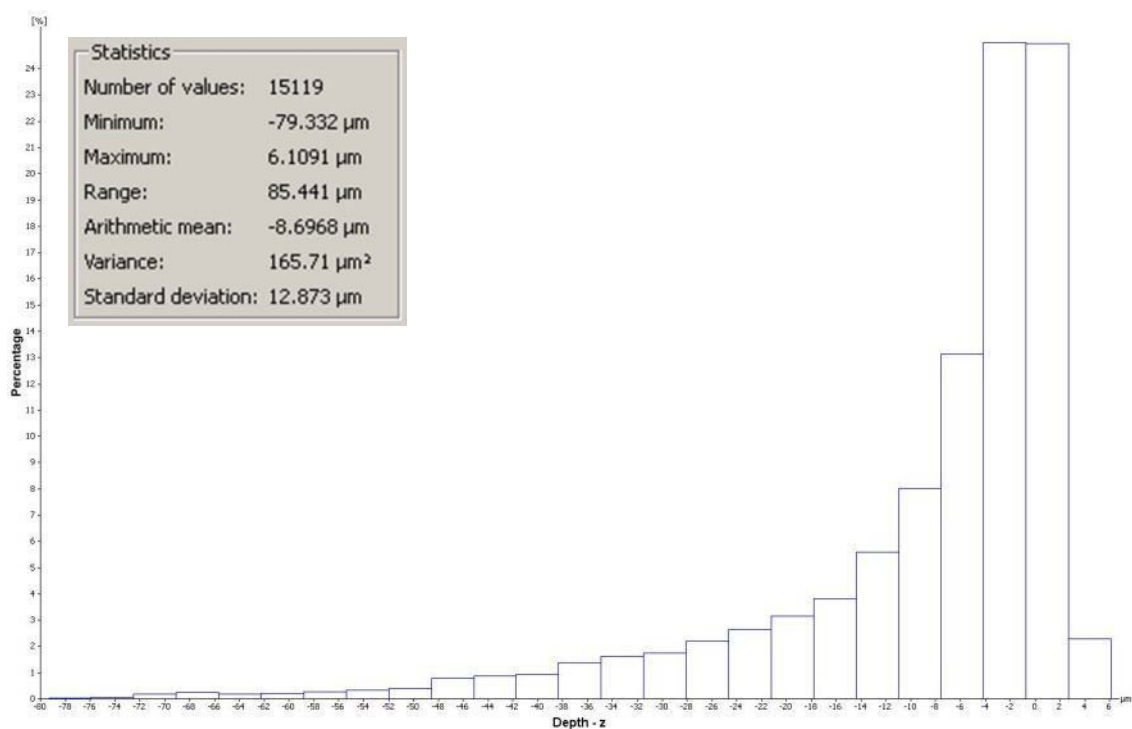
a. IFM image



b. IFM color image



b. Depth profile



c. Depth/area distribution

Figure 86. 3D Profilometry at 120°C, pH 4.0, 1 wt.% NaCl, $c\text{CO}_2 = 0.030 \text{ M}$, 14 days, corresponding to Figure 85.

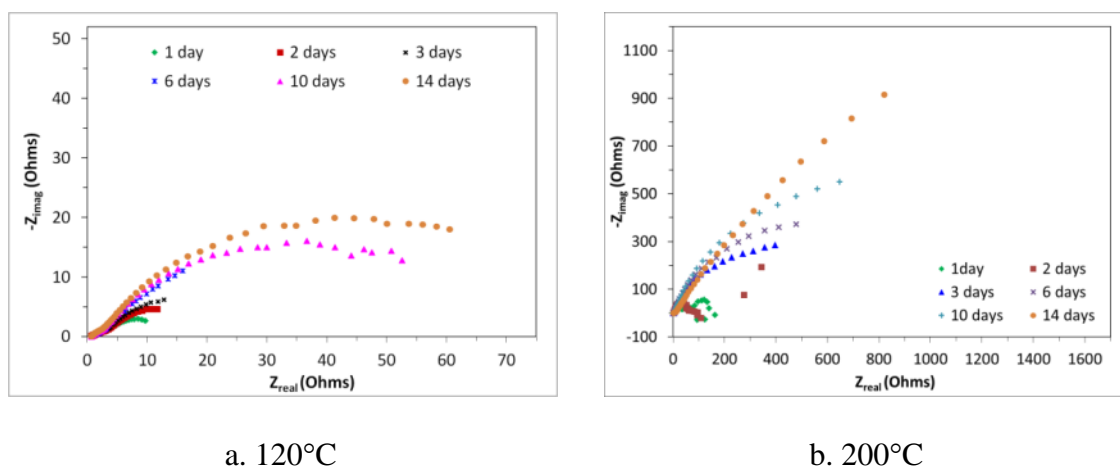
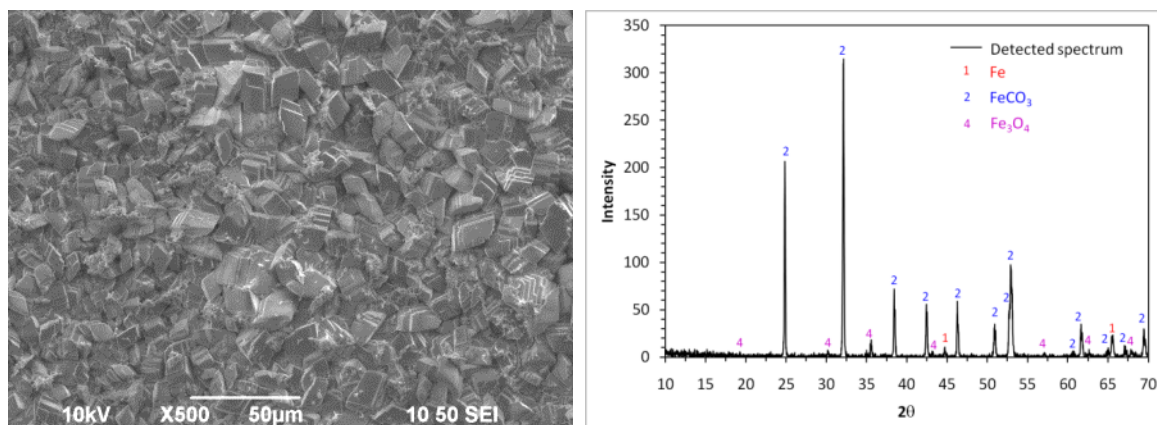
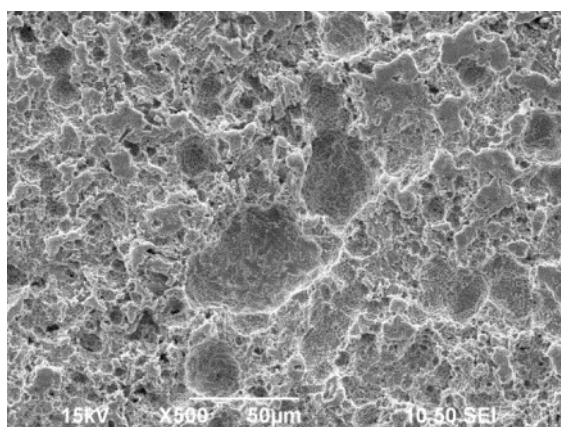


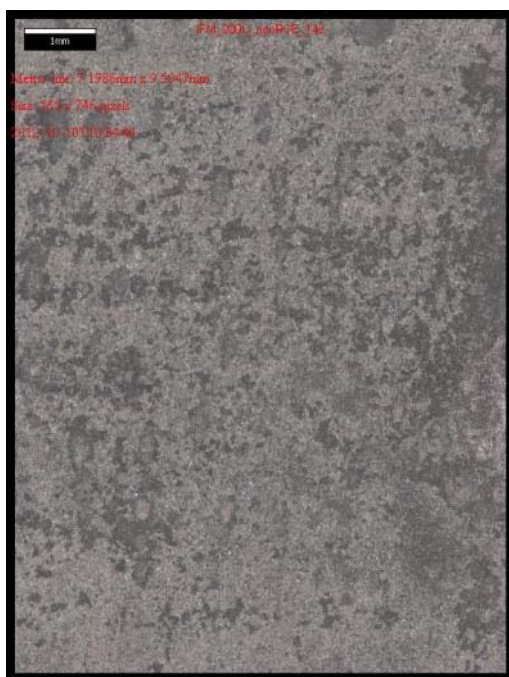
Figure 87. EIS results: pH 4.0, 1 wt.% NaCl, $c\text{CO}_2 = 0.030 \text{ M}$.



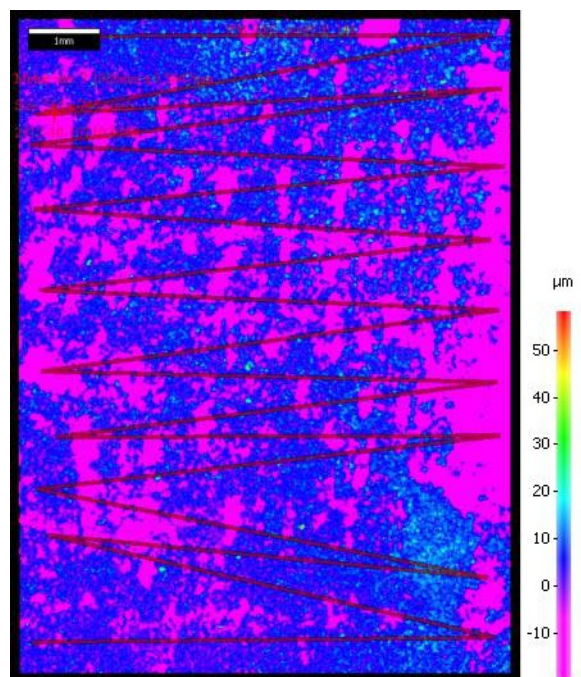
a. SEM

b. XRD

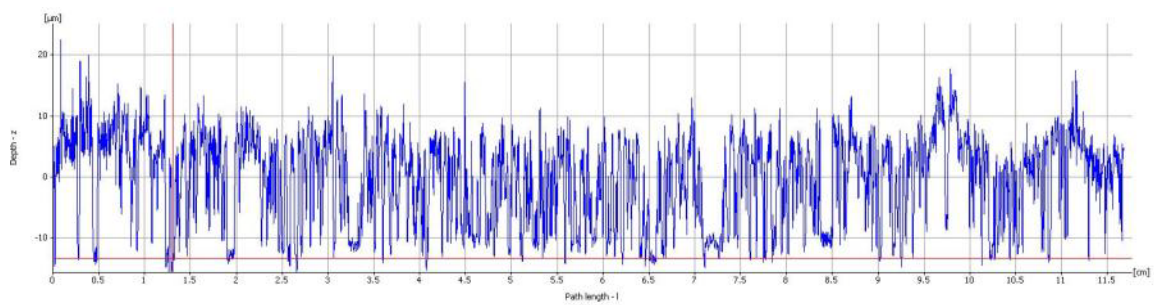
Figure 88. Surface analysis at 200°C, pH 4.0, 1 wt.% NaCl, $c\text{CO}_2 = 0.030 \text{ M}$, 14 days.Figure 89. Surface after corrosion product removal at 200°C, pH 4.0, 1 wt.% NaCl, $c\text{CO}_2 = 0.030 \text{ M}$, 14 days.



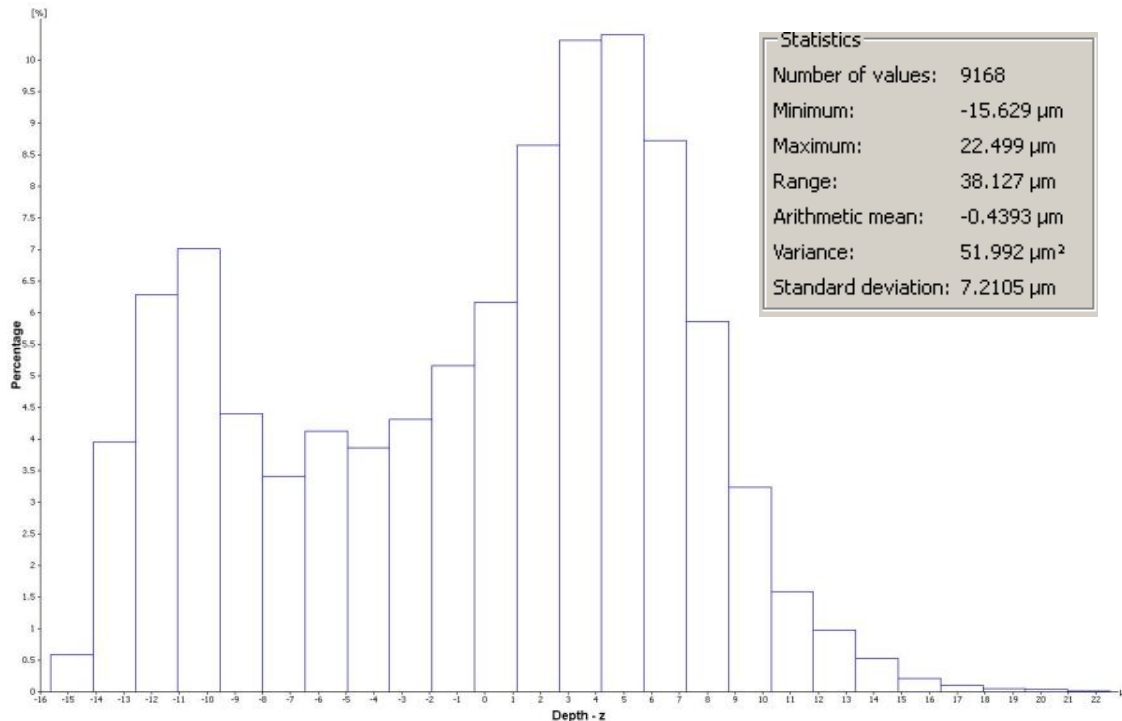
a. IFM image



b. IFM color image



b. Depth profile



c. Depth/area distribution

Figure 90. 3D Profilometry at 200°C, pH 4.0, 1 wt.% NaCl, $c\text{CO}_2 = 0.030 \text{ M}$, 14 days; corresponding to Figure 89.

The effect of flow on CO_2 corrosion at 120°C was studied using RCE. Figure 91 shows the corrosion rates from LPR at 120°C at 0 and 1000 rpm for extended test duration (14 days). From the experiments, the corrosion rates decreased with time for the stagnant condition due to the formation of corrosion product layers. However, the corrosion rate at 1000 rpm decreased to the lowest value on the second day of exposure. After that it increased and remained constant. These phenomena can be explained using Nyquist plots (Figure 92). At the beginning of the experiment, the EIS spectrum (Figure 92 a.) shows only a bare steel corrosion behavior or charge transfer controlled

corresponding to the high corrosion rate at 0 hour. Figure 92 b. shows the Nyquist plot measured on the 2nd day of the experiment. The impedance has become infinite implying a diffusion limitation on the steel surface resulting in a very low corrosion rate. For 4, 6, 10 and 14 days, the Nyquist plots as shown in Figure 92 c. and d. suggest that the mechanisms were similar to that at 0 hour (initial surface conditions). To elaborate, since the corrosion rate was very high at the beginning of the experiment, FeCO₃ formation was favored at the surface. Therefore, FeCO₃ formed and protected the steel surface as the corrosion rate decreased for the first 2 days of the experiment. However, the bulk condition was always under saturation of FeCO₃ as shown in the generated Pourbaix diagram (Figure 75). Considering that the main corrosion product was FeCO₃, the surface pH must have been higher than the bulk pH. Without flow, an increase in the concentration of Fe²⁺ with corrosion will increase the surface pH with respect to bulk pH, but, with flow, mass transfer of species reduces the difference in pH between the surface and the bulk conditions. Thus, under flowing conditions, the FeCO₃ layer was unable to remain on the surface due to the under-saturated condition. This is also confirmed by the SEM image of the steel surface after the test ended (Figure 93) as it was only partially covered by FeCO₃ crystals.

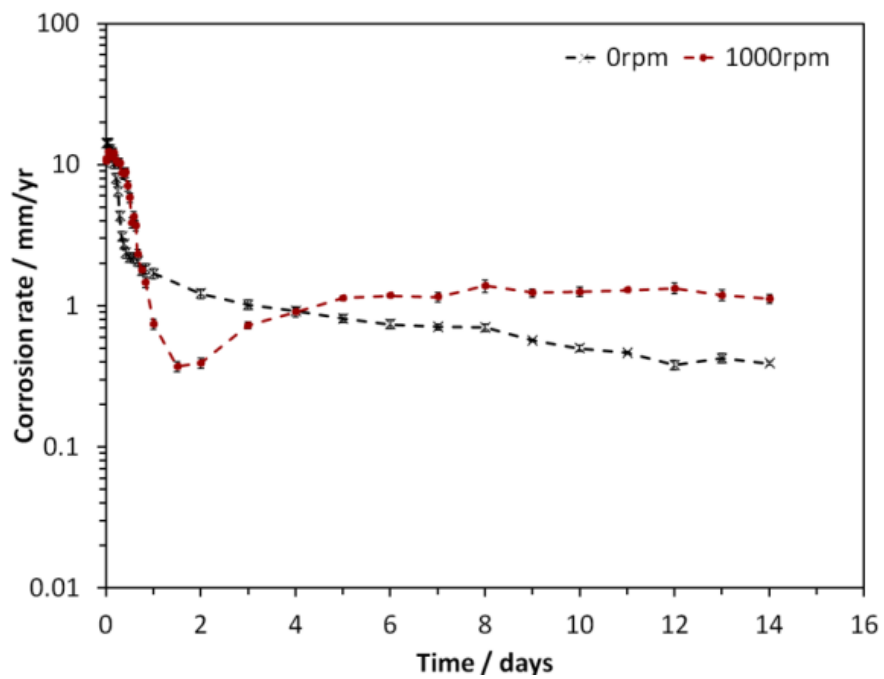
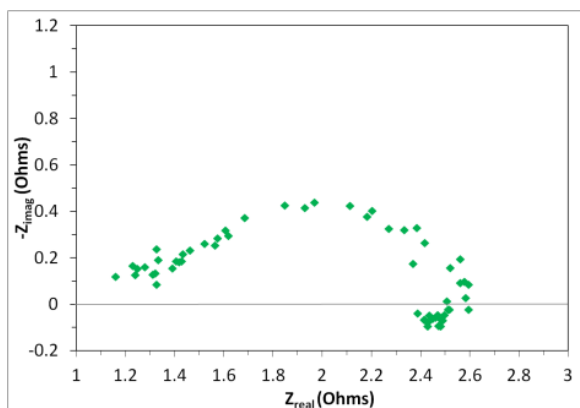
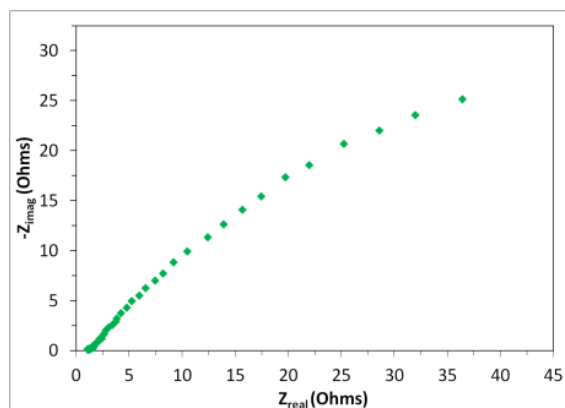


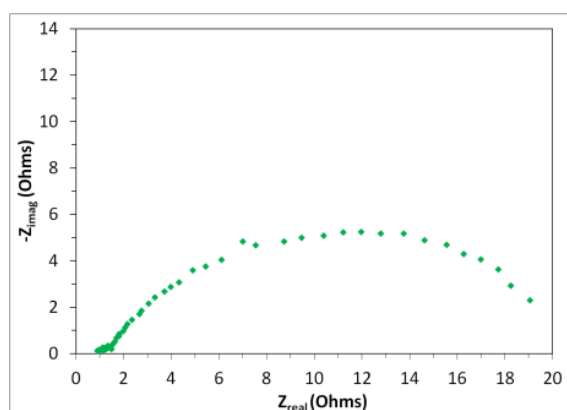
Figure 91. LPR corrosion rate at 120°C, pH 4.0, 1 wt.% NaCl, $c\text{CO}_2 = 0.030$ M, 14 days.



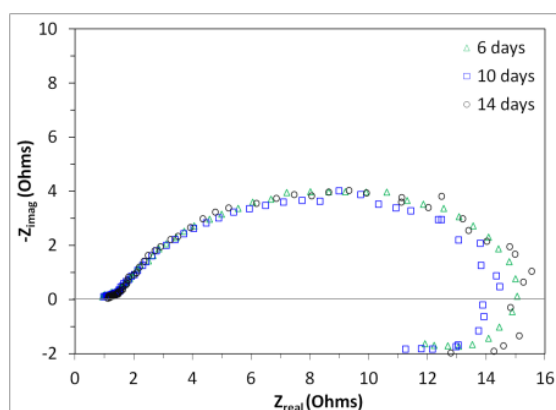
a. 0 hour



b. 2 days

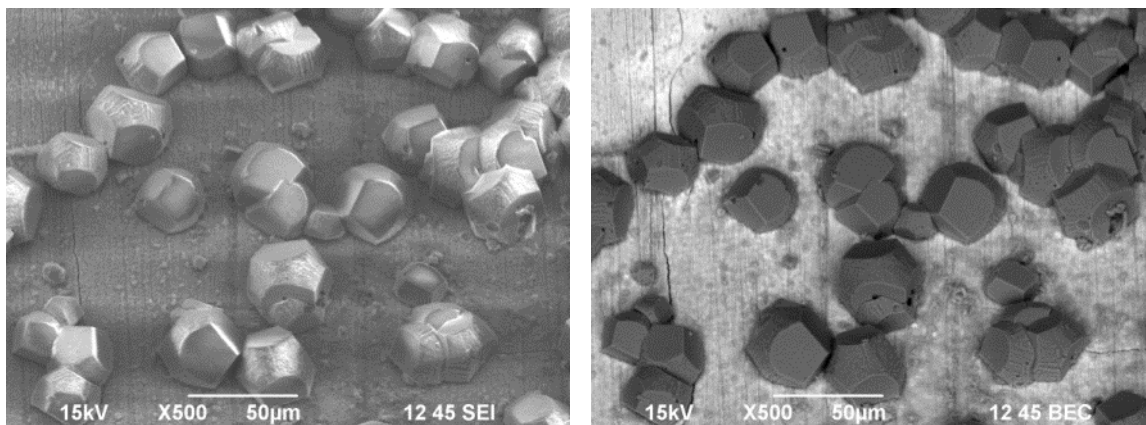


c. 4 days



d. 6, 10 and 14 days

Figure 92. Nyquist plots at 120°C, 1000 rpm, pH 4.0, 1 wt.% NaCl, $c\text{CO}_2 = 0.030$ M.



a. SEM image

b. Back-scatter image

Figure 93. Surface analysis at 120°C, 1000 rpm, pH 4.0, 1 wt.% NaCl, $c\text{CO}_2 = 0.030 \text{ M}$,
14 days.

4.4 Summary

The corrosion kinetic experiments at elevated temperatures were further investigated including the effects of pH and flow. Multiple 20-hour experiments were conducted using LPR and EIS. It was concluded that corrosion rates decrease with time for temperatures greater than 120°C due to formation of corrosion products. Corrosion rates at pH 4.0 are higher than those at pH 6.0, independent of temperature. From experimental observations, corrosion products form at lower pH with an increase in temperature. From XRD analysis, the main corrosion product was FeCO_3 with Fe_3O_4 present at temperatures above 150°C. No flow sensitivity was observed due to the formation of corrosion products.

Chapter 5: Mechanisms of CO₂ Corrosion at Elevated Temperatures

5.1 Scenario of CO₂ corrosion at temperatures up to 250°C

Based on the work discussed in Chapter 2 - Chapter 4, four classes of processes comprise the CO₂ corrosion mechanisms of mild steel, as shown in Figure 94:

1. Homogenous equilibria in an aqueous CO₂ system

In a CO₂-H₂O-NaCl system, five homogeneous chemical reactions are considered as shown in Equation (3) - (7). Gaseous CO₂ dissolves in a solution; dissolved CO₂ is hydrated to form H₂CO₃, then dissociates to HCO₃⁻ and H⁺; HCO₃⁻ dissociates to CO₃²⁻ and H⁺. Since these chemical reactions are linked *via* common species (such as H⁺) changing any one concentration, this will shift the equilibrium concentration for all the others.

2. Corrosion processes

When steel is in an aqueous environment with dissolved CO₂, corrosion processes will occur. Corrosion is an electrochemical process, consisting of two types of reactions: anodic and cathodic reactions as listed in Table 1. For CO₂ corrosion of mild steel, the main anodic reaction is iron oxidation and the main cathodic reactions are the reduction of H⁺ and H₂CO₃.

3. FeCO₃ formation at intermediate temperatures

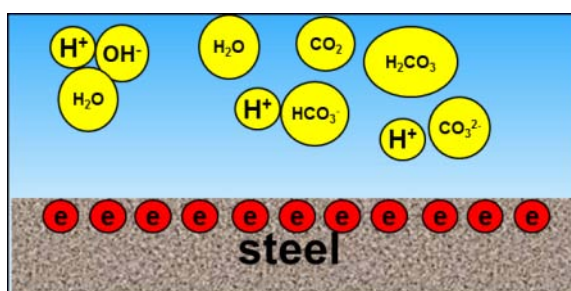
When steel corrodes, it releases Fe²⁺. Once conditions for forming FeCO₃ are achieved, FeCO₃ will precipitate and cover the steel surface what may lower the general corrosion rate. The key parameter is saturation level:

$$S = \frac{C_{\text{Fe}^{2+}} C_{\text{CO}_3^{2-}}}{K_{\text{SP, FeCO}_3}}$$

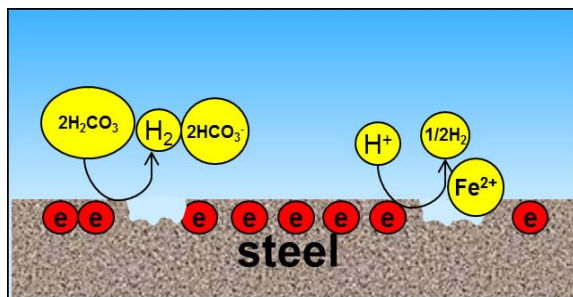
where K_{sp} is the solubility limit of $FeCO_3$. K_{sp} depends on temperature. At 25-80°C, $FeCO_3$ precipitates at elevated pH and/or high concentration of Fe^{2+} in the presence of dissolved CO_2 . $FeCO_3$ precipitation can occur at lower pH values as temperature is increased.

4. $FeCO_3$ and Fe_3O_4 formation at elevated temperatures

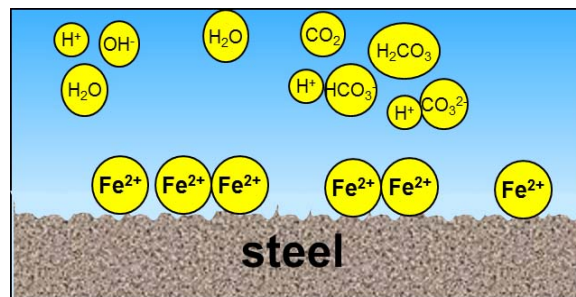
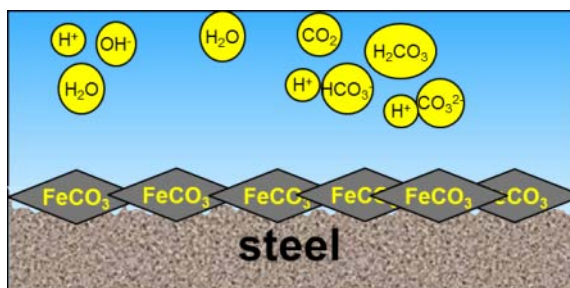
At higher temperature, there are two types of thermodynamically favored corrosion products, $FeCO_3$ and Fe_3O_4 , forming on the steel surface. The dominant corrosion product depends on the thermodynamics and kinetics of their formation. From Section 3.3.2.1 iii), for instance, at low pCO_2 , only Fe_3O_4 forms on the steel surface. However, at higher partial pressure of CO_2 , $FeCO_3$ and Fe_3O_4 may coexist on the steel surface. Since the study of $FeCO_3$ formation is well understood from the work of Sun, *et al.* [44], [81], only the mechanisms of Fe_3O_4 formation will be discussed in Section 5.2, including the thermodynamics and kinetics of Fe_3O_4 formation and interaction of $FeCO_3$ and Fe_3O_4 .



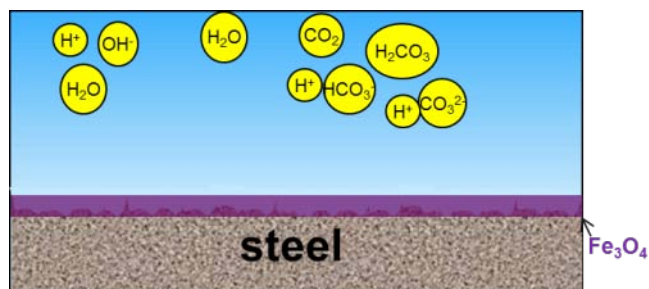
Step 1: Equilibria for CO_2 systems



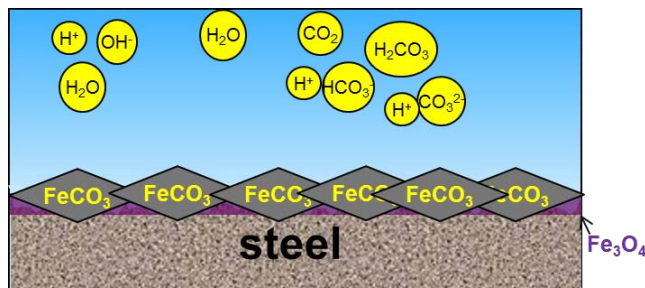
Step 2a: Corrosion process

Step 2b: Corrosion process with high
corrosion rate

Step 3: Corrosion product formation at intermediate temperature



Step 4a: Corrosion product at higher temperature



Step 4b: Corrosion product at higher temperatures at high $p\text{CO}_2$

Figure 94. Scenarios for CO_2 corrosion.

5.2 Mechanism of Fe_3O_4 formation

5.2.1 Thermodynamics of Fe_3O_4 formation

The Fe_3O_4 formation can be predicted using the understanding developed in the present study: the electro-chemical thermodynamics of $\text{Fe-CO}_2\text{-H}_2\text{O}$ systems (construction and validation of Pourbaix diagrams) in Chapter 3. Therefore, the formation of Fe_3O_4 written as Equation (37) can be predicted based on the solubility limit of Fe_3O_4 formation (K_{sp}):



$$K_{\text{sp},\text{Fe}_3\text{O}_4} = e^{-\frac{\Delta G}{RT}}$$

Figure 95 shows the K_{sp} of Fe_3O_4 formation calculated using Gibbs Free energy and compared with other literature values [108], [112]. These results are considered to be in good agreement.

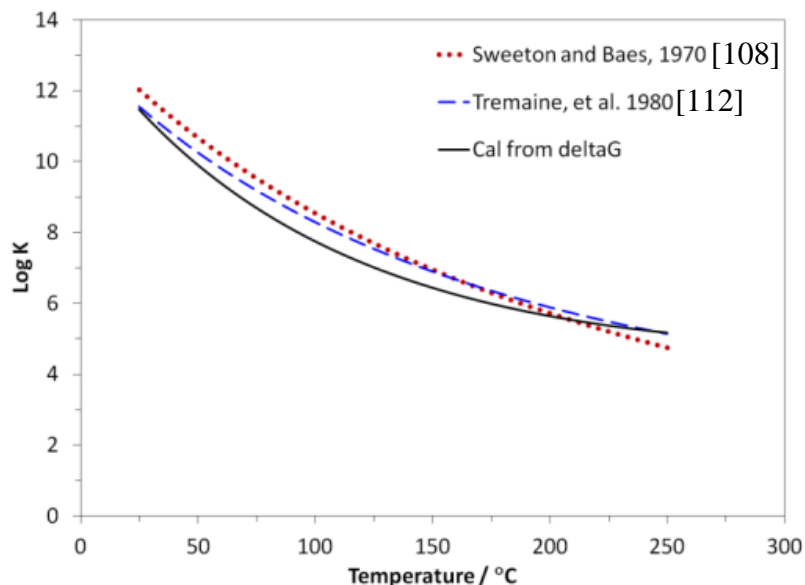


Figure 95. Solubility limit of Fe_3O_4 formation as a function of temperature.

5.2.2 Kinetics of Fe_3O_4 formation

The kinetics of Fe_3O_4 formation and the interaction of Fe_3O_4 and FeCO_3 were investigated by using the experimental results from Chapter 3 and Chapter 4. Two hypotheses were proposed:

If the kinetics of Fe_3O_4 formation is fast, then the scaling tendency (ST) is high [26], [43].

$$\text{ST} = \frac{\text{Scaling Formation Rate}}{\text{Corrosion Rate}}$$

High ST means a protective corrosion product layer is formed on the steel surface. Then *corrosion rate is very low*. In contrast, if ST is low, the steel surface will be covered by a non-protective corrosion product layer or no corrosion product is formed. Then *corrosion rate is high*.

Three cases were chosen from the previous experiments, as shown in Figure 96:

Case 1: at 120°C and 0.030M of CO₂ concentration, the surface was covered by FeCO₃.

Case 2: at 200°C and 0.030M of CO₂ concentration, a mixture of FeCO₃ and Fe₃O₄ was found on the surface.

Case 3: at 200°C and 0.021M of CO₂ concentration, only Fe₃O₄ was detected on the surface.

From the observations above, the corrosion rates were very low for all the cases where Fe₃O₄ was present. Therefore, it is also concluded that scaling tendency is high because the kinetics of Fe₃O₄ formation are fast and the corrosion rate is low.

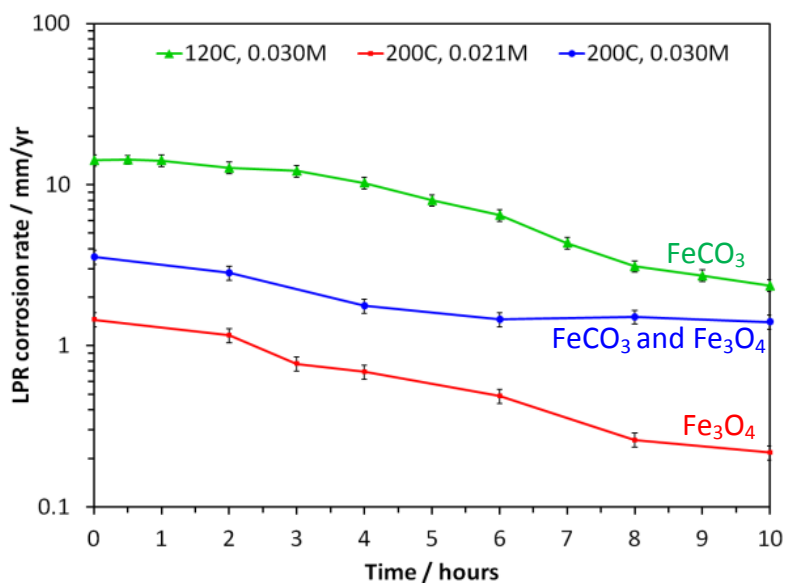


Figure 96. Comparison of corrosion rate with different types of corrosion product covered on the steel surface; pH 4.0, 1 wt.% NaCl; FeCO₃: 120°C, cCO₂ = 0.030 M; FeCO₃ and Fe₃O₄: 200°C, cCO₂ = 0.021 M; Fe₃O₄: 200°C, cCO₂ = 0.030 M.

It follows that if Fe_3O_4 forms fast, it will nucleate rapidly and form smaller crystals that are more densely packed on the surface, which will lower the corrosion rate.

Figure 97 and Figure 98 show the surface morphology of the steel surface covered by Fe_3O_4 and FeCO_3 , respectively. There is no obvious large-grain crystal structure of Fe_3O_4 when compared to FeCO_3 morphological characteristics. The size of the developed Fe_3O_4 crystals is obviously much smaller than for FeCO_3 . Fast Fe_3O_4 formation due to rapid nucleation and crystal growth leads to rapid surface coverage, providing a barrier for all species involved in the corrosion process, on a short time layer.

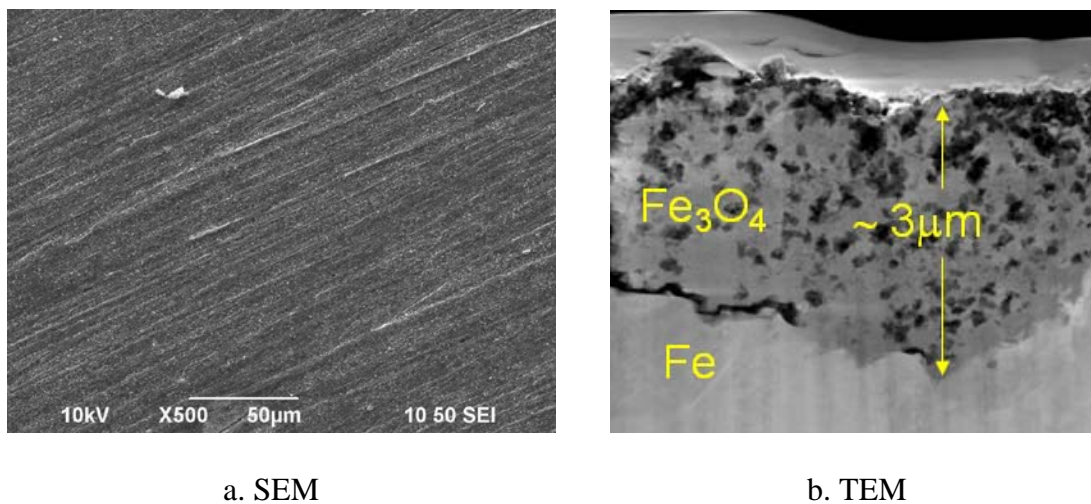
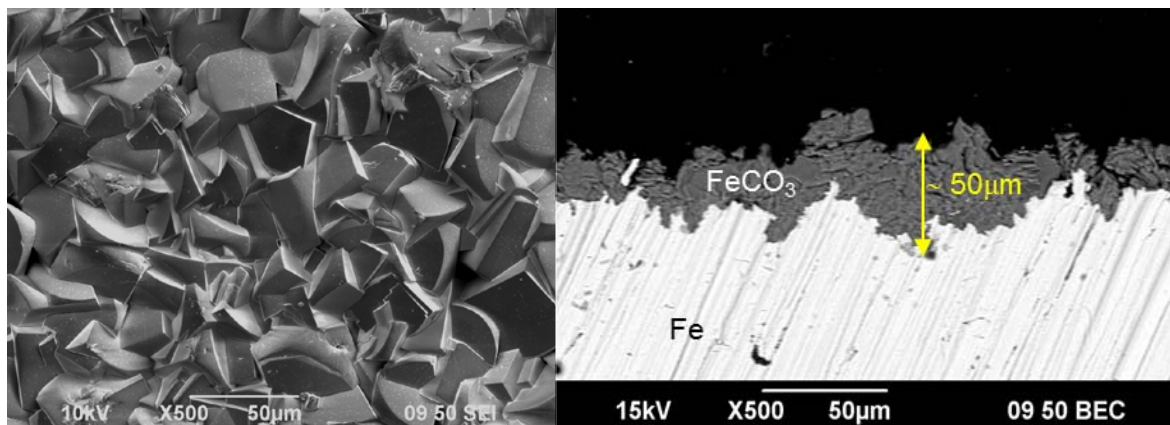


Figure 97. Morphology of Fe_3O_4 on the steel surface: results from Section 3.3.2.1 i).



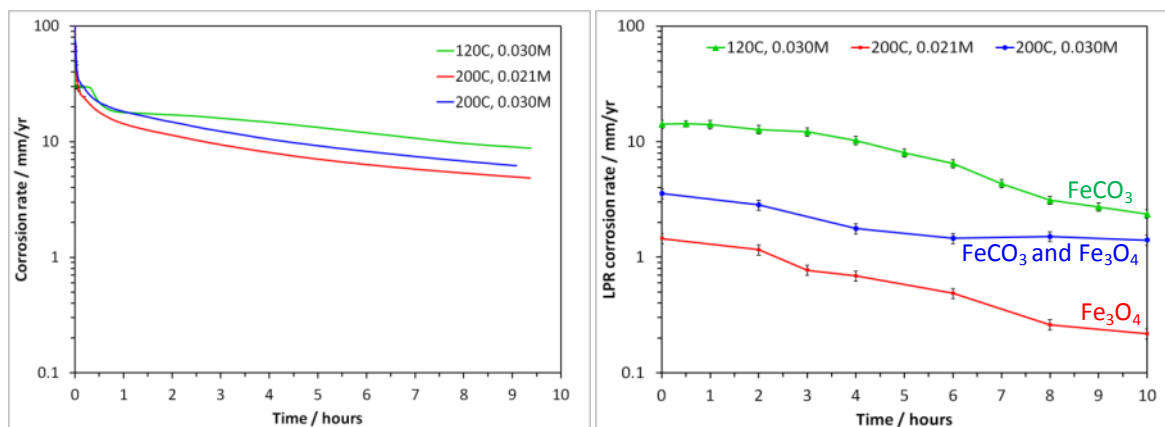
c. SEM

d. Cross-section back-scatter

Figure 98. Morphology of FeCO_3 on the steel surface; results from Section 3.3.2.1 ii).

5.2.3 Protectiveness of Fe_3O_4 formation

The predicted corrosion rates by MULTICORP (Figure 99 a.) were compared to the measured corrosion rate (Figure 99 b.). For Case 1, where the surface is covered by FeCO_3 , the predicted result provided similar values to the experiment. However, since MULTICORP can predict only FeCO_3 formation, for Case 2 and Case 3 the calculated corrosion rate is more than an order of magnitude higher than the measured corrosion rate. This means that Fe_3O_4 provided more protection to the steel surface than FeCO_3 and is not predicted by MULTICORP.

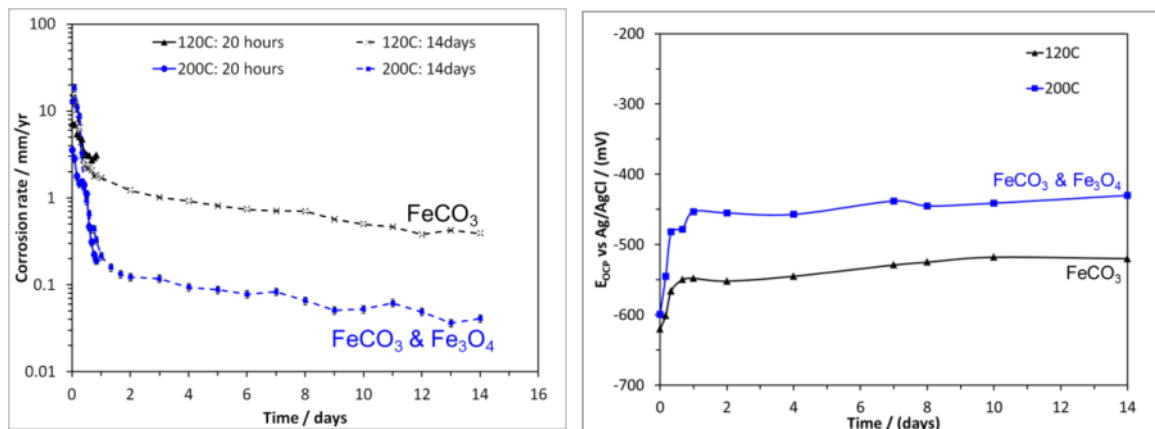


a. Predicted using MULTICORP

b. Experimental results

Figure 99. Comparison of corrosion rates between predicted and experimental results; pH 4.0, 1 wt.% NaCl; FeCO_3 : 120°C, $c\text{CO}_2 = 0.030$ M; FeCO_3 and Fe_3O_4 : 200°C, $c\text{CO}_2 = 0.021$ M; Fe_3O_4 : 200°C, $c\text{CO}_2 = 0.030$ M..

Another example showing the comparison of the corrosion rates where only FeCO_3 (at 120°C) or a mixture with Fe_3O_4 (at 200°C) covers the steel surface is shown in Figure 100 a. The corrosion rates in both cases decreased over time. However, the corrosion rate where the steel was covered by Fe_3O_4 was about a factor of 10 less than the one covered with FeCO_3 . The reduction of the corrosion rates can be explained by open circuit potentials. Figure 100 b. shows an increase in the open circuit potentials for both 120°C and 200°C tests. The open circuit potentials at 200°C (Fe_3O_4) increased more than those at 120°C. This increase is due to retardation of the anodic reaction [102], [111]. One can try and explain this behavior by three different scenarios:



a. LPR corrosion rates

b. Open circuit potentials

Figure 100. Corrosion rates and open circuit potentials at 120 and 200°C.

Scenario 1 (Figure 101): In this case, the corrosion products formed on the steel surface act as a diffusion barrier. Consequently, the cathodic reaction, hydrogen reduction, is limited by mass transfer under scaling conditions. The open circuit potential decreases under scaling conditions compared to non-scaling conditions.

Scenario 2 (Figure 102 a): Both anodic and cathodic reactions remain under charge transfer control, but the dissolution of iron is selectively slowed down more than the reduction of hydrogen. The open circuit potential increases under scaling conditions.

Scenario 3 (Figure 102 b): The steel surface is passivated by formation of a very thin protective corrosion product layer. This protective layer slows down the anodic reaction. Thus, the open circuit potential increases after corrosion product formation.

Scenarios 2 and 3 are plausible, while Scenario 1 is not. It is concluded that Fe₃O₄ formation retards the anodic reaction, *i.e.*, the dissolution of iron is slowed down. By inspecting the morphology of corrosion products formed on the steel surface (Figure

103), Fe_3O_4 is always formed in between the parent steel surface and the FeCO_3 layer, which may lead to passivation of the steel surface. This finding is consistent with the results from Han, *et al.* [64] obtained at lower temperature but higher pH.

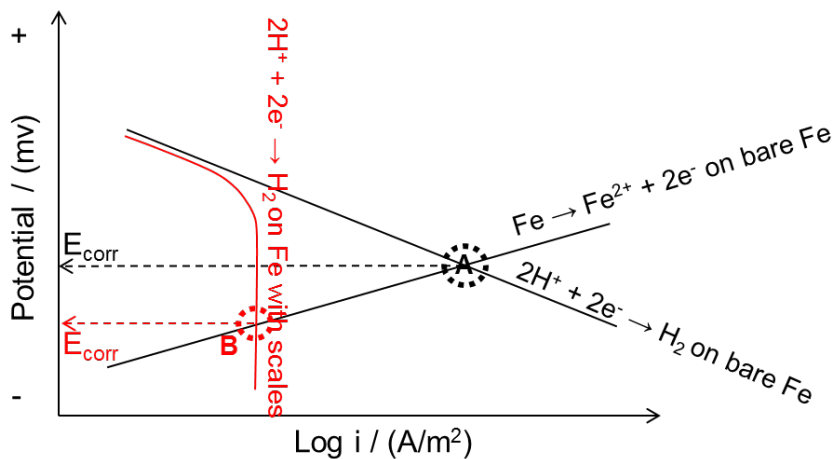
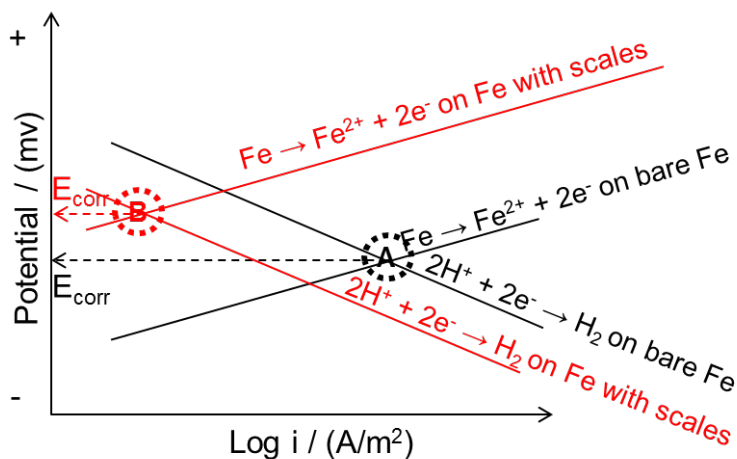
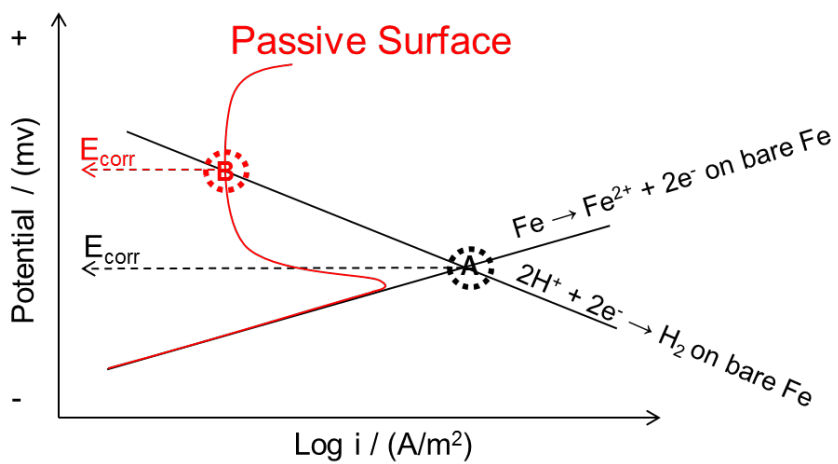


Figure 101. Decrease in open circuit potentials due to diffusion barrier.



a. The anodic reaction retarded more than the cathodic reaction.



b. Passivated steel surface

Figure 102. Increase in open circuit potentials.

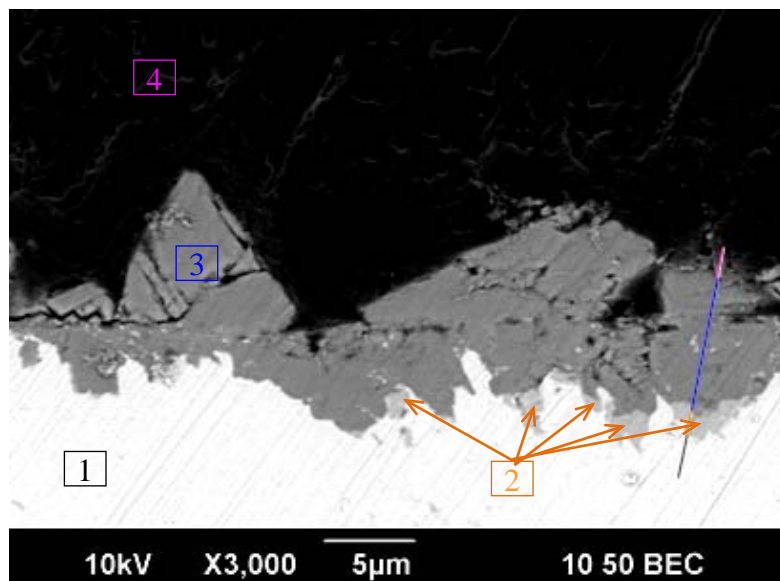


Figure 103. Morphology of the steel surface covered by corrosion products from Figure

67: 1 = Fe, 2 = Fe₃O₄, 3 = FeCO₃, 4 = Epoxy.

5.3 Summary

Mechanisms of CO₂ corrosion at temperatures of 25-250°C have been proposed based on the current CO₂ corrosion model by adding the effect of Fe₃O₄ formation. The thermodynamics and kinetics of Fe₃O₄ formation were identified. As soon as (local) thermodynamic conditions for Fe₃O₄ are achieved, it rapidly forms and protects the steel reducing the corrosion rate approximately by an order of magnitude. Fe₃O₄ formation retards mostly the anodic reaction, *i.e.*, the dissolution of iron is slowed down.

Chapter 6: Conclusions and Recommendations for Future Work

6.1 Conclusions

Electrochemical investigation of high temperature CO₂ corrosion has been conducted both experimentally and computationally. The following can be concluded:

1. The homogenous water chemistry model used in the current corrosion prediction model is valid for temperatures in the range 25-250°C based on comparison with experimental results and published data

2. The Pourbaix diagrams were constructed and validated with the experimental data over a temperature range of 25-250°C. Dissolved Fe²⁺, solid FeCO₃ and solid Fe₃O₄ are the main corrosion products to be expected in CO₂ corrosion of mild steel. In the pH range of 3-7 (typical range of CO₂ systems), the main species are:

- Fe²⁺ at low temperature and pressure;
- Once temperature and CO₂ partial pressure increase, iron carbonate (FeCO₃) and magnetite (Fe₃O₄) become dominant species.

3. The electrochemical kinetics of CO₂ corrosion at temperatures of 25-200°C was investigated using electrochemical measurement and can be summarized as follows:

- At 25-200°C, corrosion rate does not increase monotonously with temperature due to corrosion product formation.
- Corrosion rates at pH 4.0 are higher than those at pH 6.0 for each temperature.
- Flow has no effect on CO₂ corrosion after the protective corrosion product layer is formed.
- In a long-term study, localized corrosion was observed at 120°C.

4. Mechanisms of CO₂ corrosion at 25-250°C have been proposed based on the current CO₂ corrosion model of MULTICORP. Apart from water chemistry, corrosion rate and FeCO₃ formation, the mechanism of Fe₃O₄ formation is primarily governed by the rapid kinetics of its formation. Once the thermodynamic conditions are achieved, small crystals of Fe₃O₄ nucleate instantaneously and rapidly grow, forming a dense layer that acts as a diffusion barrier which greatly reduces corrosion rate approximately by an order of magnitude.

6.2 Recommendations for future work

Some recommendations for future work are as follows:

1. Further study the thermodynamics of Fe₂(OH)₂CO₃ and incorporate it into the construction of Pourbaix diagrams as appropriate.
2. Perform experiments in a flow through autoclave where the solution can be refreshed and kept at under-saturated conditions to prevent FeCO₃ formation and better understand the kinetic rate of corrosion process without interference of the corrosion product formation.
3. Perform experiments in a large scale flow loop to achieve higher velocities and have similar conditions to field operations.
4. Further analyze the EIS results to better understand the mechanism of anodic and cathodic reactions in the corrosion processes.
5. Add H₂S into the Pourbaix diagrams.

References

- [1] F. G. Harper, "Ultimate hydrocarbon resources in the 21st century," in *Oil and Gas in the 21st Century*, 1999.
- [2] R. W. Bentley, "Global oil and gas depletion: An overview," *Energy Policy*, vol. 30, p. 189–205, 2002.
- [3] R. Bentley, "The oil and gas situation," www.oildpletion.org, 2002. [Online].
- [4] C. De Waard, U. Lotz, and D. E. Milliams, "Predictive model for CO₂ corrosion engineering in wet natural gas pipelines," *Corrosion*, vol. 47, p. 976–985, 1991.
- [5] C. De Waard and D. E. Milliams, "Prediction of carbonic acid corrosion in natural-gas pipelines," in *First Internat. Conf. Internal and External Protection of Pipes*, vol. 31, p. 177–181, 1975.
- [6] P. L. Fosbøl, "Carbon Dioxide Corrosion: Modelling and experimental work applied to natural gas pipelines," Ph.D. dissertation, Technical University of Denmark, 2008.
- [7] L. G. S. Gray, B. G. Anderson, M. J. Danysh, and P. R. Tremaine, "Effect of pH and temperature on the mechanism of carbon steel corrosion by aqueous carbon dioxide," in *Corrosion/90*, Paper no. 40, 1990.
- [8] L. G. S. Gray, B. G. Anderson, M. J. Danysh, and P. R. Tremaine, "Mechanism of carbon steel corrosion in brine containing dissolved carbon dioxide at pH 4," in *Corrosion/89*, Paper no. 464, 1989.
- [9] A. Ikeda, S. Mukai, and M. Ueda, "Prevention of CO₂ corrosion of line pipe and oil country tubular goods," in *Corrosion/84*, Paper no. 289, 1984.

- [10] M. B. Kermani and A. Morshed, "Carbon dioxide corrosion in oil and gas production - A compendium," *Corrosion*, vol. 59, p. 659–683, 2003.
- [11] L. S. Moiseeva, "Carbon dioxide corrosion of oil and gas field equipment," *Protection of Metals*, vol. 41, p. 76–83, 2005.
- [12] S. Nešić, D. Drazic, N. Thevenot, and J. L. Crolet, "Electrochemical properties of iron dissolution in the presence of CO₂-basics revisited," in *Corrosion/96*, Paper no. 3, 1996.
- [13] S. Nešić, M. Nordsveen, and A. Stangeland, "A mechanistic model for CO₂ corrosion with protective iron carbonate scale films," in *Corrosion/01*, Paper no. 01040, 2001.
- [14] S. Nešić, J. Postlethwaite, and S. Olsen, "An electrochemical model for prediction of corrosion of mild steel in aqueous carbon dioxide solutions," *Corrosion*, vol. 52, p. 280–294, 1996.
- [15] S. Nešić, "Key issues related to modelling of internal corrosion of oil and gas pipelines – A review," *Corrosion Science*, vol. 49, p. 4308–4338, 2007.
- [16] M. Nordsveen, S. Nešić, R. Nyborg, and A. Stangeland, "A mechanistic model for carbon dioxide corrosion of mild steel in the presence of protective iron carbonate films - Part 1: Theory and verification," *Corrosion*, vol. 59, p. 443–456, 2003.
- [17] J. E. Oddo and M. B. Tomson, "The prediction of scale and CO₂ corrosion in oil field systems," in *Corrosion/99*, Paper no. 41, 1999.
- [18] E. Remita, B. Tribollet, E. Sutter, F. Ropital, X. Longaygue, J. Kittel, C. Taravel-Condât, and N. Desamais, "A kinetic model for CO₂ corrosion of steel in confined

- aqueous environments,” *Journal of The Electrochemical Society*, vol. 155, p. C41-C45, 2008.
- [19] G. Schmitt, “Corrosion of steels: An attempt to range parameters and their effects,” in *Corrosion/83*, Paper no. 23, 1983.
- [20] G. Schmitt, “Fundamental aspects of CO₂ metal loss corrosion - Part II: influence of different parameters on CO₂ corrosion mechanisms,” in *Corrosion/06*, Paper no.06112, 2006.
- [21] M. Ueda, “2006 F.N. Speller Award lecture: Development of corrosion-resistance alloys for the oil and gas industry - Based on spontaneous passivity mechanism,” *Corrosion*, vol. 62, p. 856–867, 2006.
- [22] M. Ueda and H. Takabe, “Effect of environmental factor and microstructure on morphology of corrosion products in CO₂ environments,” in *Corrosion/99*, Paper no. 13, 1999.
- [23] E. Gulbrandsen, J. H. Morard, and J. L. Crolet, “Study of the possible mechanisms of steel passivation in CO₂ corrosion,” in *Corrosion/99*, Paper no. 624, 1999.
- [24] A. Ikeda, M. Ueda, and S. Mukai, “CO₂ corrosion behavior and mechanism of carbon steel and alloy steel,” in *Corrosion/83*, Paper no. 45, 1983.
- [25] K. Masamura and I. Matsushima, “Corrosion and electrochemical behavior of steel in CO₂ bearing water,” *Transactions of the Iron and Steel Institute of Japan*, vol. 23, p. 676–679, 1983.

- [26] S. Nešić and K. L. J. Lee, "A mechanistic model for carbon dioxide corrosion of mild steel in the presence of protective iron carbonate films - Part 3: Film growth model," *Corrosion*, vol. 59, p. 616–628, 2003.
- [27] S. Nešić, M. Nordsveen, R. Nyborg, and A. Stangeland, "A mechanistic model for carbon dioxide corrosion of mild steel in the presence of protective iron carbonate films - Part 2: A numerical experiment," *Corrosion*, vol. 59, p. 443–456, 2003.
- [28] R. Nyborg, "Overview of CO₂ corrosion models for wells and pipelines," in *Corrosion/02*, Paper no. 02233, 2002.
- [29] E. Remita, B. Tribollet, E. Sutter, V. Vivier, F. Ropital, and J. Kittel, "Hydrogen evolution in aqueous solutions containing dissolved CO₂: Quantitative contribution of the buffering effect," *Corrosion Science*, vol. 50, p. 1433–1440, 2008.
- [30] Z. F. Yin, Y. R. Feng, W. Z. Zhao, Z. Q. Bai, and G. F. Lin, "Effect of temperature on CO₂ corrosion of carbon steel," *Surface and Interface Analysis*, vol. 41, p. 517–523, 2009.
- [31] D. W. Shannon, "Role of chemical components in geothermal brines on corrosion," in *Corrosion/78*, Paper no. 78057, 1978.
- [32] G. Lin, M. Zheng, Z. Bai, and X. Zhao, "Effect of temperature and pressure on the morphology of carbon dioxide corrosion scales," *Corrosion*, vol. 62, p. 501–507, 2006.
- [33] T. Tanupabrunsun, "Water chemistry of an Fe-CO₂-H₂O system at temperatures of 25-250C," *Advisory Board Meeting Report*, Institute for Corrosion and Multiphase Technology, Athens, Ohio, 2009.

- [34] T. Tanupabrunsun, "Corrosion products of mild steel at 80-250°C in an aqueous CO₂ solution," Advisory Board Meeting Report, Institute for Corrosion and Multiphase Technology, Athens, Ohio, 2010.
- [35] T. Tanupabrunsun, "Effect of pH and flow on CO₂ corrosion at elevated temperatures," Advisory Board Meeting Report, Institute for Corrosion and Multiphase Technology, Athens, Ohio, 2011.
- [36] T. Tanupabrunsun, "CO₂ corrosion at elevated temperature," Advisory Board Meeting Report, Institute for Corrosion and Multiphase Technology, Athens, Ohio, 2010.
- [37] T. Tanupabrunsun, "Modeling the thermodynamics of an Fe-CO₂-H₂O system," Advisory Board Meeting Report, Institute for Corrosion and Multiphase Technology, Athens, Ohio, 2009.
- [38] T. Tanupabrunsun, "Water chemistry of a CO₂ system at higher temperature," Advisory Board Meeting Report, Institute for Corrosion and Multiphase Technology, Athens, Ohio, 2008.
- [39] T. Tanupabrunsun, "CO₂ corrosion of mild steel at elevated temperatures," Advisory Board Meeting Report, Institute for Corrosion and Multiphase Technology, Athens, Ohio, 2012.
- [40] T. Tanupabrunsun, D. Young, B. Brown, and S. Nešić, "Construction and Verification of Pourbaix Diagrams for CO₂ Corrosion of Mild Steel Valid up to 250°C," in Corrosion/12, Paper no. 0001418, 2012.

- [41] T. Tanupabrunsun, S. Nešić, and B. Brown, "Effect of pH on CO₂ corrosion at elevated temperatures," in Corrosion/13, Paper no. 0002348, 2013.
- [42] C. D. Waard and D. E. Milliams, "Carbonic acid corrosion of steel," Corrosion, vol. 31, p. 177–182, 1975.
- [43] E. W. J. van Hunnik, B. F. M. Pots, and E. L. J. A. Hendriksen, "The formation of protective FeCO₃ corrosion product layers in CO₂ corrosion," in Corrosion/96, Paper no. 6, 1996.
- [44] W. Sun, S. Nešić, and S. Papavinasam, "Kinetics of corrosion layer formation: Part 1 - Iron carbonate layers in carbon dioxide corrosion," Corrosion, vol. 64, p. 334–346, 2008.
- [45] E. Dayalan, F. D. de Moraes, J. R. Shadley, S. A. Shirazi, and E. F. Rybicki, "CO₂ corrosion prediction in pipe flow under FeCO₃ scale-forming conditions," in Corrosion/98, Paper no. 51, 1998.
- [46] S. Savoye, L. Legrand, G. Sagon, S. Lecomte, A. Chausse, R. Messina, and P. Toulhoat, "Experimental investigations on iron corrosion products formed in bicarbonate/carbonate-containing solutions at 90°C," Corrosion Science, vol. 43, p. 2049–2064, 2001.
- [47] W. Sun and S. Nešić, "Basics revisited: kinetics of iron carbonate scale precipitation in CO₂ corrosion," in Corrosion/06, Paper no. 06365, 2006.
- [48] S. Nešić, J. Lee, and V. Ruzic, "A mechanistic model of iron carbonate film growth and the effect on CO₂ corrosion of mild steel," in Corrosion/02, Paper no. 02237, 2002.

- [49] K. Chokshi, W. Sun, and S. Nešić, "Iron carbonate scale growth and the effect of inhibitor in CO₂ corrosion of mild steel," in Corrosion/05, Paper no. 05285, 2005.
- [50] A. Dugstad, "Mechanism of protective film formation during CO₂ corrosion of carbon steel," in Corrosion/98, Paper no. 31, 1998.
- [51] M. Gao, X. Pang, and K. Gao, "The growth mechanism of CO₂ corrosion product films," Corrosion Science, vol. 53, pp. 557–568, 2011.
- [52] Y. Yang, B. Brown, and S. Nešić, "Mechanical strength and removal of a protective iron carbonate layer formed on mild steel in CO₂ corrosion," in Corrosion/10, Paper no. 10383, 2010.
- [53] K. Videm, "The influence of composition of carbon steels on anodic- and cathodic reaction in CO₂ corrosion," in Corrosion/98, Paper no. 30, 1998.
- [54] C. de Waard and U. Lotz, "Prediction of CO₂ corrosion of carbon steel," in Corrosion/93, Paper no. 69, 1993.
- [55] S. Wang, K. George, and S. Nešić, "High pressure CO₂ corrosion electrochemistry and the effect of acetic acid," in Corrosion/04, Paper no. 04375, 2004.
- [56] K. George, C. de Waard, and S. Nešić, "Electrochemical investigation and modeling of carbon dioxide corrosion of carbon steel in the presence of acetic acid," in Corrosion/04, Paper no. 04379, 2004.
- [57] S. Nešić, S. Wang, J. Cai, and Y. Xiao, "Integrated CO₂ corrosion-multiphase flow model," in Corrosion/04, Paper no. 04626, 2004.
- [58] B. F. M. Pots, "Mechanistic models for the prediction of CO₂ corrosion rates under multi-phase flow conditions," in Corrosion/95, Paper no. 137, 1995.

- [59] C. de Waard, U. Lotz, and A. Dugstad, "Influence of liquid flow velocity on CO₂ corrosion: A semi-empirical model," in *Corrosion/95*, Paper no. 128, 1995.
- [60] S. Nešić, G. T. Solvi, and J. Enerhaug, "Comparison of the rotating cylinder and pipe flow tests for flow-sensitive carbon dioxide corrosion," *Corrosion*, vol. 51, p. 773–787, 1995.
- [61] M. Honarvar Nazari, S. R. Allahkaram, and M. B. Kermani, "The effects of temperature and pH on the characteristics of corrosion product in CO₂ corrosion of grade X70 steel," *Materials and Design*, vol. 31, p. 3559–3563, 2010.
- [62] R. De Marco, Z.-T. Jiang, B. Pejčić, and E. Poinen, "An In Situ Synchrotron Radiation Grazing Incidence X-Ray Diffraction Study of Carbon Dioxide Corrosion," *Journal of The Electrochemical Society*, vol. 152, p. B389–B392, 2005.
- [63] R. De Marco, Z.-T. Jiang, D. John, M. Sercombe, and B. Kinsella, "An in situ electrochemical impedance spectroscopy/synchrotron radiation grazing incidence X-ray diffraction study of the influence of acetate on the carbon dioxide corrosion of mild steel," *Electrochimica Acta*, vol. 52, p. 3746–3750, 2007.
- [64] J. Han, D. Young, H. Colijn, A. Tripathi, and S. Nešić, "Chemistry and structure of the passive film on mild steel in CO₂ corrosion environments," *Industrial and Engineering Chemistry Research*, vol. 48, p. 6296–6302, 2009.
- [65] C. Rémazeilles and P. Refait, "Fe(II) hydroxycarbonate Fe₂(OH)₂CO₃ (chukanovite) as iron corrosion product: Synthesis and study by Fourier Transform Infrared Spectroscopy," *Polyhedron*, vol. 28, p. 749–756, 2009.

- [66] M. L. Schlegel, C. Bataillon, C. Blanc, D. Prêt, and E. Foy, "Anodic activation of iron corrosion in clay media under water-saturated conditions at 90 degrees C: characterization of the corrosion interface," *Environmental Science and Technology*, vol. 44, p. 1503–8, 2010.
- [67] D. A. Palmer and R. V. Eldik, "The chemistry of metal carbonato and carbon dioxide complexes," *Chemical Reviews*, vol. 83, p. 651–731, 1983.
- [68] Z. Duan and R. Sun, "An improved model calculating CO₂ solubility in pure water and aqueous NaCl solutions from 273 to 533 K and from 0 to 2000 bar," *Chemical Geology*, vol. 193, p. 257–271, 2003.
- [69] A. J. Ellis and R. M. Golding, "The solubility of carbon dioxide above 100 degrees C in water and in sodium chloride solutions," *American Journal of Science*, vol. 261, p. 47–60, 1963.
- [70] S. Portier and C. Rochelle, "Modelling CO₂ solubility in pure water and NaCl-type waters from 0 to 300 °C and from 1 to 300 bar: Application to the Utsira Formation at Sleipner," *Chemical Geology*, vol. 217, p. 187–199, 2005.
- [71] F. Millero, F. Huang, T. Graham, and D. Pierrot, "The dissociation of carbonic acid in NaCl solutions as a function of concentration and temperature," *Geochimica et Cosmochimica Acta*, vol. 71, p. 46–55, 2007.
- [72] J. E. Odde and M. B. Tomson, "Simplified calculation of CaCO₃ saturation at high temperatures and pressures in brine solutions," *Journal of Petroleum Technology*, vol. 34, p. 1583–1590, 1982.

- [73] A. Zawlsza and B. Maleslnska, "Solubility of carbon dioxide in liquid water and of water in gaseous carbon dioxide in the range 2-5 MPa and at temperatures up to 473 K," *Journal of Chemical and Engineering Data*, vol. 26, p. 388–391, 1981.
- [74] L. I. Gordon and L. B. Jones, "The effect of temperature on carbon dioxide partial pressures in seawater," *Marine Chemistry*, vol. 1, p. 317–322, 1973.
- [75] R. F. Weiss, "Carbon dioxide in water and seawater: the solubility of a non-ideal gas," *Marine Chemistry*, vol. 2, p. 203–215, 1974.
- [76] J. J. Carroll, J. D. Slupsky, and A. E. Mather, "The solubility of carbon dioxide in water at low pressure," *Journal of Physical Chemistry Reference Data*, vol. 20, p. 1201–1210, 1991.
- [77] C. Palmer and J. Cherry, "Geochemical evolution of groundwater in sequences of sedimentary rocks," *Journal of Hydrology*, vol. 75, p. 27–65, 1984.
- [78] Y. K. Kharaka, E. H. Perkins, W. D. Gunter, J. D. Debral, and C. H. Bamford, "Solmineq 88: A computer program for geochemical modeling of water rock interactions," *ACS Symposium Series*, p. 117–127, 1990.
- [79] D. Li and Z. Duan, "The speciation equilibrium coupling with phase equilibrium in the H₂O-CO₂-NaCl system from 0 to 250°C, from 0 to 1000 bar, and from 0 to 5 molality of NaCl," *Chemical Geology*, vol. 244, p. 730–751, 2007.
- [80] C. Patterson, G. Slocum, R. Busey, and R. Mesmer, "Carbonate equilibria in hydrothermal systems: first ionization of carbonic acid in NaCl media to 300°C," *Geochimica et Cosmochimica Acta*, vol. 46, p. 1653–1663, 1982.

- [81] F. H. Sweeton, R. E. Mesmer, and C. F. Baes, "Acidity measurements at elevated temperatures. VII. Dissociation of water," *Journal of Solution Chemistry*, vol. 3, p. 191–214, 1974.
- [82] R. H. Perry and D. W. Green, *Perry's Chemical Engineers' Handbook*, 7th ed. New York: McGraw-Hill, 1999, p. 2582.
- [83] S. Al-Hassan, B. Mishra, D. L. Olson, and M. M. Salama, "Effect of microstructure on corrosion of steels in aqueous solutions containing carbon dioxide," *Corrosion*, vol. 54, p. 480–491, 1998.
- [84] X. Guo and Y. Tomoe, "The effect of corrosion product layers on the anodic and cathodic reactions of carbon steel in CO₂-saturated mdea solutions at 100°C," *Corrosion Science*, vol. 41, p. 1391–1402, 1999.
- [85] C. A. Palacios and J. R. Shadley, "Characteristics of corrosion scales on steels in a CO₂-saturated NaCl brine," *Corrosion*, vol. 47, p. 122–127, 1991.
- [86] M. Ueda, "Potential-pH diagram at elevated temperatures for metal-CO₂/H₂S-water systems and the application for corrosion of pure iron," *Corrosion Engineering*, vol. 44, p. 159–174, 1995.
- [87] M. Pourbaix, "Thermochemical diagrams: Some applications to study of high temperature corrosion," *Materials Science and Engineering*, vol. 87, p. 303–317, 1987.
- [88] M. Pourbaix, "Thermodynamics and corrosion," *Corrosion Science*, vol. 30, p. 963–988, 1990.

- [89] P. Paine, "Technical Note: Potential-pH diagrams for the Fe-Cl-H₂O system at 25 to 150°C," *Corrosion*, vol. 46, p. 19–21, 1990.
- [90] H. E. Townsend, "Potential-pH diagrams at elevated temperature for the system Fe-H₂O," *Corrosion Science*, vol. 10, p. 343–358, 1970.
- [91] B. Beverskog and I. Puigdomenech, "Revised Pourbaix diagrams for iron at 25–300°C," *Corrosion Science*, vol. 38, p. 2121–2135, 1996.
- [92] V. Ashworth and P. J. Boden, "Potential-pH diagrams at elevated temperatures," *Corrosion Science*, vol. 10, p. 709–718, 1970.
- [93] M. Kaye and W. Thompson, "Computation of Pourbaix Diagrams at Elevated Temperature," in *Uhlig's Corrosion Handbook*, 3rd ed., R. W. Revie, Ed. John Wiley and Sons, Inc., 2011, p. 111–122.
- [94] R. A. Robie, H. T. Haselton, and B. S. Hemingway, "Heat capacities and entropies of rhodochrosite (MnCO₃) and siderite (FeCO₃) between 5 and 600 K," *American Mineralogist*, vol. 69, p. 349–357, 1984.
- [95] O. Knacke, O. Kubaschewski, and K. Hesselmann, Eds., *Thermochemical properties of inorganic substances*, 2nd ed. New York: Springer-Verlag, 1991, p. 2412.
- [96] T. Nishimura and J. Dong, "Corrosion behavior of carbon steel for overpack in groundwater containing bicarbonate ions," *Journal of Power and Energy Systems*, vol. 3, p. 23–30, 2009.
- [97] ASTM G 111-97, "Standard Guide for Corrosion Tests in High Temperature or High Pressure," p. 1–5.

- [98] J. Han, B. N. Brown, D. Young, and S. Nešić, "Mesh-capped probe design for direct pH measurements at an actively corroding metal surface," *Journal of Applied Electrochemistry*, vol. 40, p. 683–690, 2009.
- [99] T. R. Lee and R. T. Wilkin, "Iron hydroxy carbonate formation in zerovalent iron permeable reactive barriers: characterization and evaluation of phase stability," *Journal of contaminant hydrology*, vol. 116, p. 47–57, 2010.
- [100] I. Azoulay, C. Rémazeilles, and P. Refait, "Determination of standard Gibbs free energy of formation of chukanovite and Pourbaix diagrams of iron in carbonated media," *Corrosion Science*, vol. 58, p. 229–236, 2012.
- [101] M. F. Suhor, M. F. Mohamed, A. M. Nor, M. Singer, and S. Nešić, "Corrosion of mild steel in high CO₂ environment: Effect of the FeCO₃ layer," in *Corrosion/12*, Paper no. 1434, 2012.
- [102] J. Han, "Galvanic Mechanism of Localized Corrosion for Mild Steel in Carbon Dioxide Environments," Ph.D. Dissertation, Ohio University, 2009.
- [103] H. Fang, "Low temperature and high salt concentration effects on general CO₂ corrosion for carbon steel," M.S. Thesis, Ohio University, 2006.
- [104] I. Epelboin and M. Keddam, "Faradaic impedances: diffusion impedance and reaction impedance," *Journal of the Electrochemical Society*, vol. 117, p. 1052–1056, 1970.
- [105] I. Epelboin, M. Keddam, and H. Takenouti, "Use of impedance measurements for the determination of the instant rate of metal corrosion," *Journal of Applied Electrochemistry*, vol. 2, p. 71–79, 1972.

- [106] M. Keddam, O. R. Mattos, and H. Takenouti, "Reaction Model for Iron Dissolution Studied by Electrode Impedance I. Experimental Results and Reaction Model," *Journal of Electrochemical Society*, vol. 128, p. 257–266, 1981.
- [107] G. Baril, G. Galicia, C. Deslouis, N. Pébère, B. Tribollet, and V. Vivier, "An impedance investigation of the mechanism of pure magnesium corrosion in sodium sulfate solutions," *Journal of The Electrochemical Society*, vol. 154, p. C108–C113, 2007.
- [108] F. Sweeton and C. Baes, "The solubility of magnetite and hydrolysis of ferrous ion in aqueous solutions at elevated temperatures," *The Journal of Chemical Thermodynamics*, vol. 2, p. 479–500, 1970.
- [109] S. E. Ziemniak, M. E. Jones, and K. E. S. Combs, "Magnetite solubility and phase stability in alkaline media at elevated temperatures," *Journal of Solution Chemistry*, vol. 24, p. 837–877, 1995.
- [110] J. Ning, "Verification of Pourbaix diagrams for the H₂S-H₂O-Fe system," Advisory Board Meeting Report, Institute for Corrosion and Multiphase Technology, Athens, Ohio, 2012.
- [111] J. Han, Y. Yang, S. Nešić, and B. N. Brown, "Roles of passivation and galvanic effects in localized CO₂ corrosion of mild steel," in *Corrosion/08*, Paper no. 08332, 2008.
- [112] P. R. Tremaine and J. C. Leblanc, "The solubility of magnetite and the hydrolysis and oxidation of Fe²⁺ in Water to 300°C," *Journal of Solution Chemistry*, vol. 9, p. 415–442, 1980.

- [113] L. W. Niedrach, "Use of a High Temperature pH Sensor as a 'Pseudo-Reference Electrode' in the Monitoring of Corrosion and Redox Potentials at 285°C," *Journal of The Electrochemical Society*, vol. 129, p. 1445, 1982.
- [114] K. J. Lee, "A Mechanistic Modeling of CO₂ Corrosion of Mild Steel in the Presence of H₂S," Ph.D. Dissertation, Ohio University, 2004.

Appendix A: Experimental Techniques

A.1 pH measurements

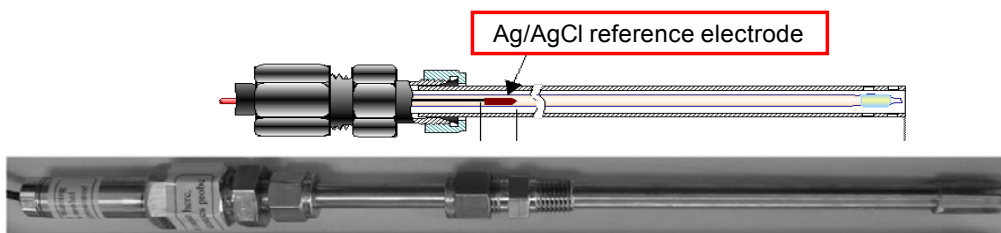
A.1.1. Types of pH electrodes

There are three types of pH electrodes used in this work, as shown in Figure 104.

- Glass-based pH electrode used at temperatures up to 80°C.
- Moderate temperature pH electrode, termed a high temperature glass-based electrode, used at temperatures of 0-130°C and pressures of 0-150 psig.
- High temperature/high pressure ZrO₂-based pH electrode with a zirconium oxide membrane, referred to as a high temperature/high pressure pH electrode (Figure 104 a.). This can be operated at temperatures of 110-150°C and pressures of 0-2000 psi. A limitation of the ZrO₂-based pH electrode is that this type of electrode does not work at low temperature since the zirconium oxide membrane has too high impedance at temperatures lower than 105°C. Furthermore, the ZrO₂-based pH electrode does not contain a reference electrode, so an external high temperature/high pressure reference electrode is required. Figure 104 b. shows the reference electrode used: an Ag/AgCl external reference electrode. It works at temperatures of 0-305°C and pressures of 0-2000 psi. In the experiment, the high temperature glass-based and high temperature/high pressure ZrO₂-based pH electrodes were used.



a. High temperature/High pressure ZrO₂-based pH electrode



b. High temperature/High pressure reference electrode

Figure 104. Types of pH electrodes and a high temperature reference electrode (Source: *Corr Instruments, LLC*).

A.1.2. Calibration of high temperature/high pressure pH electrode

pH electrodes depend on temperature. They are compensated for in the pH meter circuitry utilizing the Nernst equation:

$$E = E_x - \frac{2.3RT_K}{nF} pH \quad (38)$$

where: E_x = constant potential from reference electrode

R = gas constant

T_K = temperature (K)

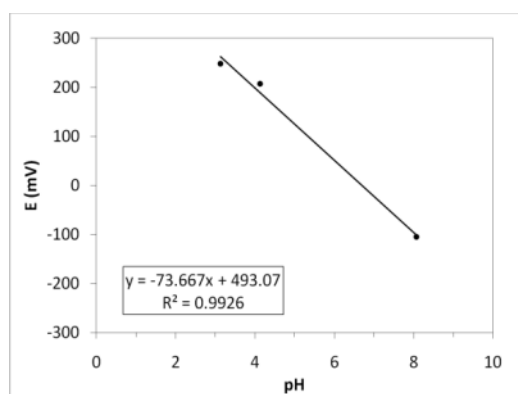
n = charge of the ion (including sign)

F = Faraday constant

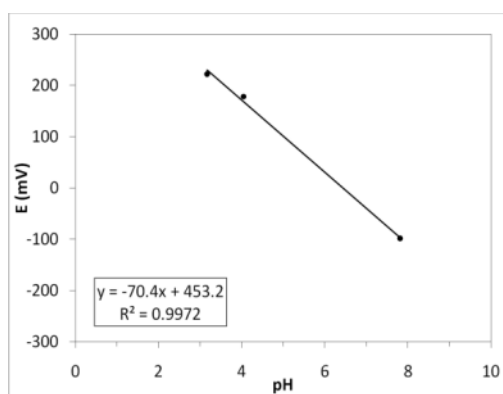
Changes in the temperature of a solution will alter the potential or millivolt output of the pH electrodes according to the Nernst equation.

For the HT/HP ZrO₂-based pH electrode, pH is measured using the millivolt option on a standard pH meter due to a potential versus pH calibration curve. The calibration temperature must be the same as the test temperature. At temperature above 100°C, standard solutions are sulfuric acid (H₂SO₄) or sodium hydroxide (NaOH). pH values of these solutions at different concentrations and elevated temperatures were published by Niedrach [113]. The measured potential versus pH calibration curves are as shown in Figure 105 (calibration curve). The slopes of the calibration curves are 10 to 20% lower than the theoretical Nernst slope (Equation (39)) due to the special ZrO₂ membrane.

$$\text{Theoretical slope} = -\frac{2.3RT_K}{nF} = -0.1977T_K \quad (39)$$



At T=80°C



At T=120°C

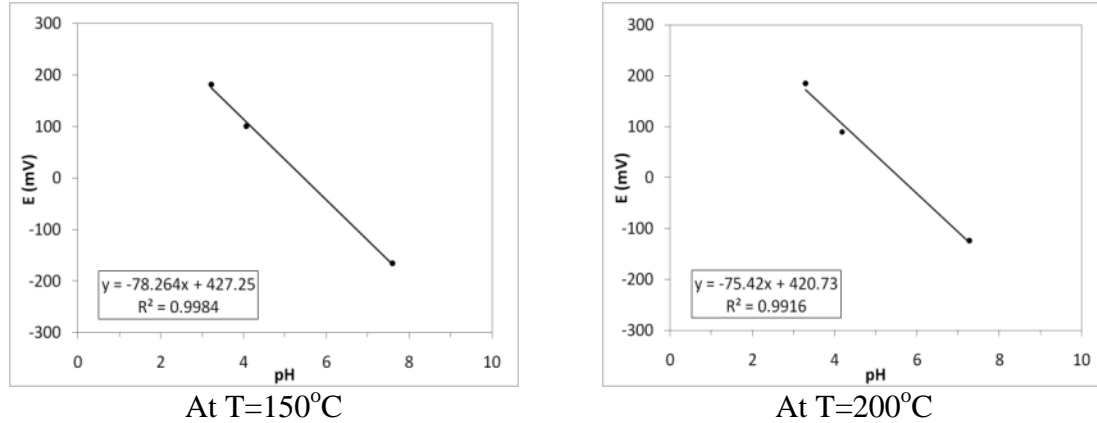


Figure 105. Measured potential vs. pH calibration curve for the ZrO₂-based pH electrode.

A.2 Corrosion rate calculation

A.2.1. Weight loss method

The corrosion rate by weight loss method is determined as follows:

$$\begin{aligned}
 CR &= \frac{m_1 - m_2}{MW_{Fe} \times t \times A} \left(\frac{\text{mol}}{\text{m}^2 \cdot \text{h}} \right) \\
 &= \frac{m_1 - m_2}{MW_{Fe} \times t \times A} \times \frac{365 \times 24 \times MW_{Fe}}{\rho} \quad (\text{mm/year})
 \end{aligned} \tag{40}$$

where CR = corrosion rate, in mol/(m².h) or mm/year,

m_1 = the weight of specimen prior to running experiments, in g,

m_2 = the weight of specimen after removing the scale, in g,

MW_{Fe} = the molecular weight of iron atom, in g/mol,

t = the exposed time, in hour,

A = the exposed specimen surface area, in m².

ρ = density of the specimen in kg/m³.

A.2.2 Linear polarization resistance (LPR)

Linear polarization method was used to measure the corrosion rate of the steel. This technique is discussed in detail in [114]. The linear polarization method is based on the electrochemical theory and the corrosion current can be obtained using the following Equation (41):

$$i_{corr} = \frac{\beta_a \beta_c}{2.303(\beta_a + \beta_c)} \frac{di_{app}}{dE} \quad (41)$$

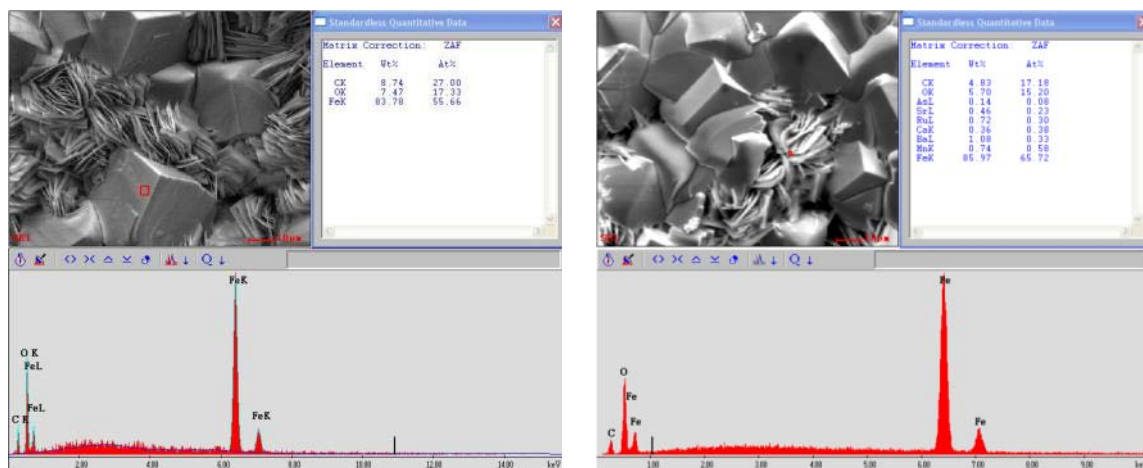
where i_{app} is the applied current density, E is the applied voltage, β_a is the anodic tafel slope, and β_c is the cathodic tafel slope. The corrosion rate can be obtained by converting the corrosion current density (i_{corr}) to the corrosion rate using Equation (42).

$$Corrosion\ rate\ (mm/year) = 1.16i_{corr} \quad (42)$$

where i_{corr} is the current density in A/m².

Appendix B: EDX Analysis of Specimens

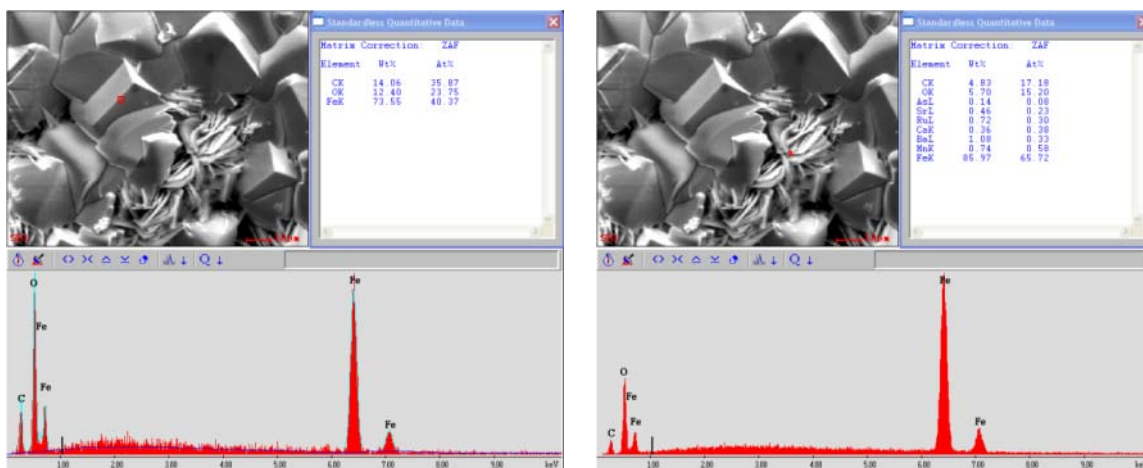
Additional surface analysis of specimens for Section 3.3.2.1.



a. Prism

b. Plate

Figure 106. EDX analysis of sample at 80°C, 4 days corresponding to Figure 18.



a. Prism

b. Plate

Figure 107. EDX analysis of sample at 100°C, 4 days corresponding to Figure 19.

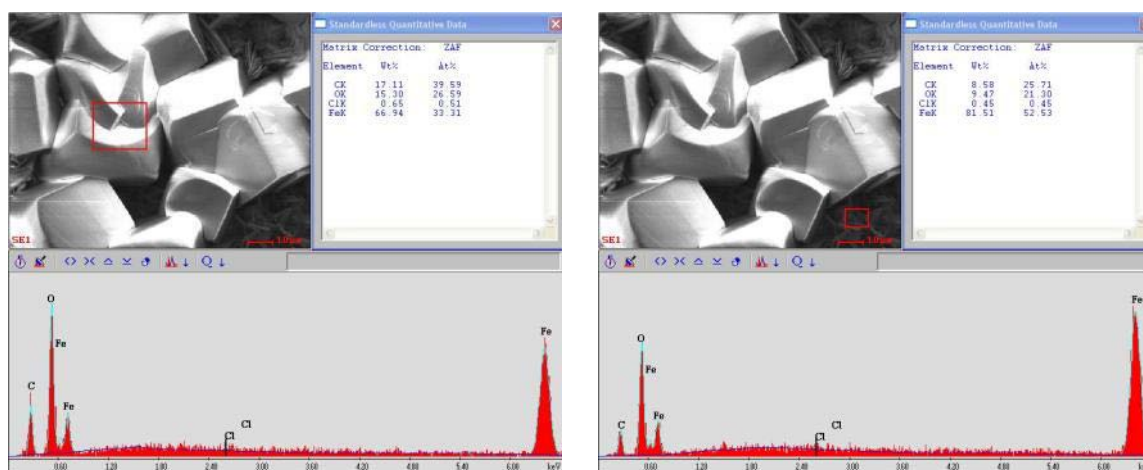


Figure 108. EDX analysis of sample at 120°C, 4 days corresponding to Figure 20.

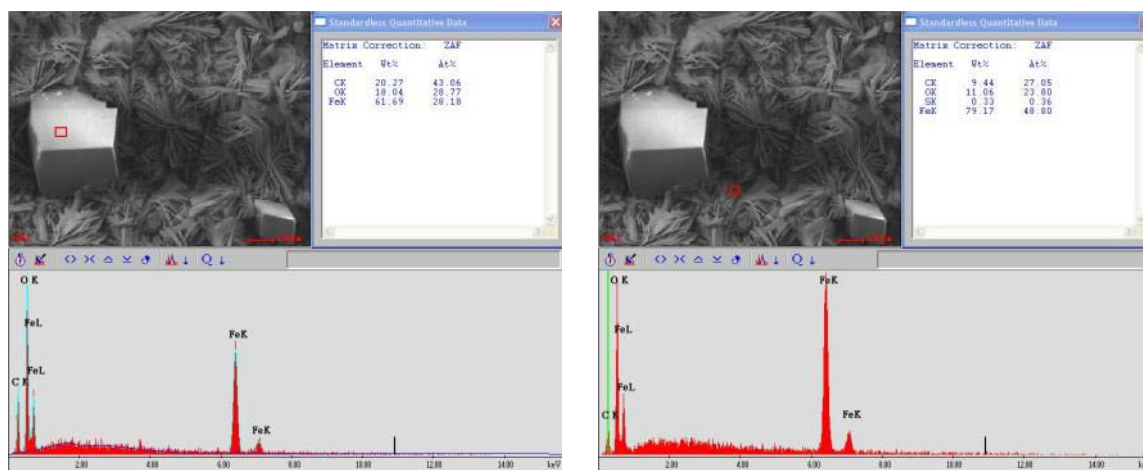


Figure 109. EDX analysis of sample at 150°C, 4 days corresponding to Figure 21.

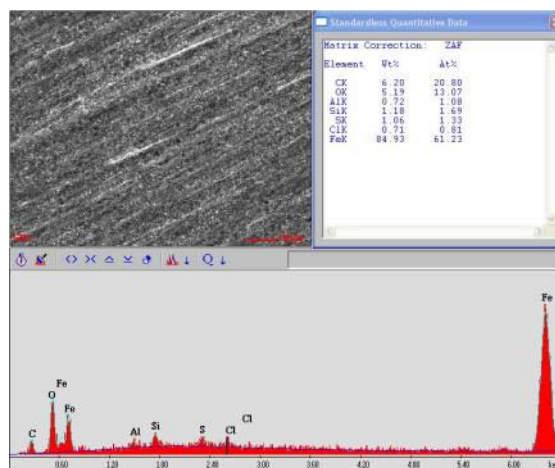
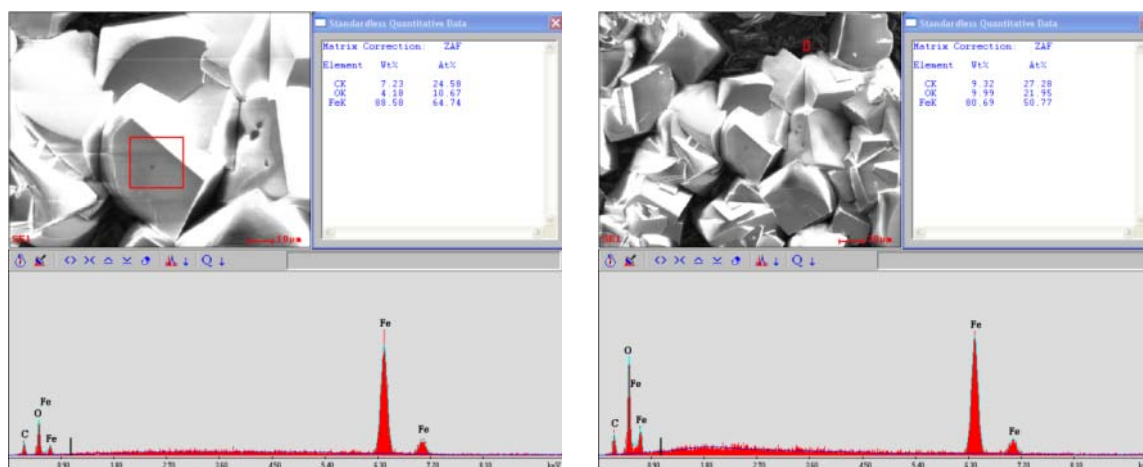


Figure 110. EDX analysis of sample at 200°C, 4 days corresponding to Figure 22.



a. Prism

b. Plate

Figure 111. EDX analysis of sample at 120°C, 7 days corresponding to Figure 26.

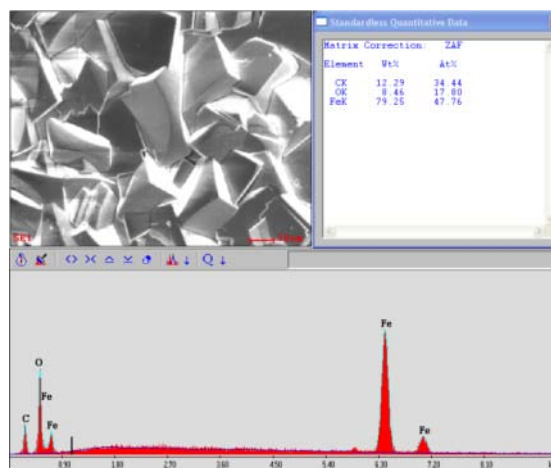
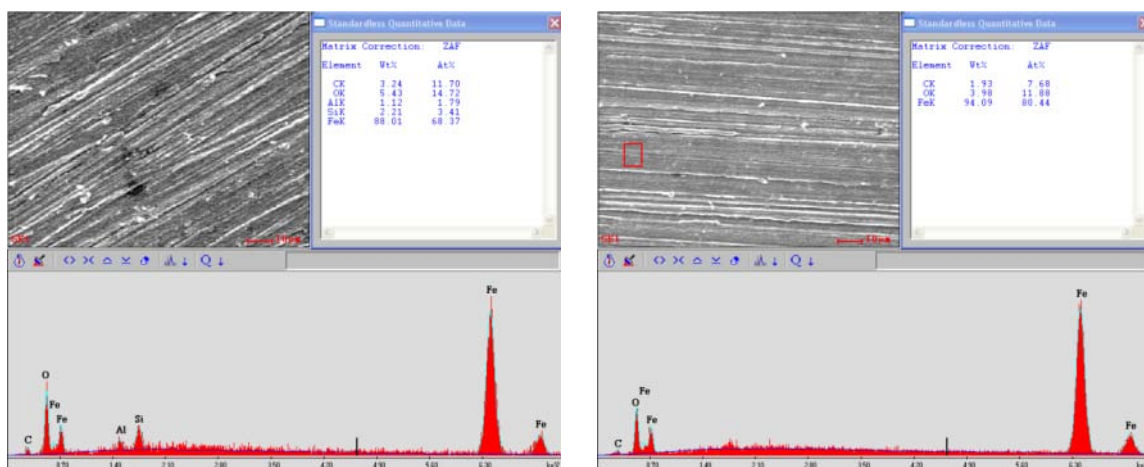


Figure 112. EDX analysis of sample at 120°C, 30 days corresponding to Figure 28.



a. 10 days

b. 30 days

Figure 113. EDX analysis of sample at 200°C corresponding to Figure 29.



OHIO
UNIVERSITY

Thesis and Dissertation Services